Second harmonic generation spectroscopy of plasmonic nanostructures and metamaterials

Dissertation

zur

Erlangung des Doktorgrades (Dr. rer. nat.)

der

Mathematisch-Naturwissenschaftlichen Fakultät

der

Rheinischen Friedrich-Wilhelms-Universität Bonn

vorgelegt von

Heiko Linnenbank

aus

Warendorf

Bonn 2015

Angefertigt mit Genehmigung der Mathematisch-Naturwissenschaftlichen Fakultät der Rheinischen Friedrich-Wilhelms-Universität Bonn

1. Gutachter:	Prof. Dr. Stefan Linden
2. Gutachter:	Priv.-Doz. Dr. Elisabeth Soergel
Tag der Promotion:	27.07.2015
Erscheinungsjahr:	2015

Abstract

Plasmonic nanostructures are subwavelength sized metallic structures which interact with electromagnetic waves, e.g., light, on the basis of frequency selective, collective oscillations of the conduction electrons, the so-called plasmonic resonances. These resonances can be tailored by engineering the size and shape of the metallic structures and lead to a strong local intensity enhancement close to the metal structures for an incident electromagnetic wave. Due to their tunable optical response, plasmonic nanostructures are frequently used as the building blocks of metamaterials, which are man-made effective materials supporting unprecedented optical properties. One class of optical processes, which can be strongly enhanced by both, optical resonances in matter and local intensity enhancements, are nonlinear optical frequency conversion processes. The most prominent and also first demonstrated among those is second harmonic generation, the instantaneous conversion of a strong electromagnetic wave into a new wave with twice the frequency inside a material lacking inversion symmetry. In this thesis, second harmonic generation from plasmonic nanostructures and metamaterials will be investigated.

In order to perform second harmonic generation spectroscopy on plasmonic nanostructures, i.e., to analyse the second harmonic generation efficiency of these structures as a function of the pump frequency, a novel light source for the generation of widely tunable ultrashort laser pulses is developed. This light source is based on optical parametric generation and amplification in a single macroscopic lithium niobate crystal. This process converts an intense wave into two new waves, whereas the sum of the frequencies of the new waves has to match the frequency of the original one. By this, femtosecond pulses generated by a 42 MHz repetition rate passively mode-locked Yb:KGW oscillator are converted into more than two watts of tunable near-infrared radiation between 1370 nm and at least 1650 nm. Beside its high average output power this device shows a high long term stability and allows to achieve pulse durations down to below 200 fs. Thus it constitutes an ideal light source to investigate second harmonic generation from plasmonic nanostructures.

To analyse the interplay between the local intensity enhancement, inherent to plasmonic nanostructures, and the nonlinear optical response of dielectric matter, plasmonic nanoantennas and nonlinear dielectric nanoparticles are combined in a two-stage electron-beam lithography process. Second harmonic generation spectroscopy on the combined hybrid dielectric/plasmonic nanoantennas as well as on the individual constituents shows, that second harmonic generation from the bare gold nanoantennas, even though it should be forbidden due to symmetry reasons, is several orders of magnitude larger than that of the bare dielectric nanoparticles. As even stronger second harmonic signals are generated by the hybrid dielectric/plasmonic nanoantennas, control experiments with nanoantennas containing linear

dielectric nanoparticles are performed to study the origin of the second harmonic generation enhancement. These experiments reveal that the increased second harmonic generation efficiency of the hybrid dielectric/plasmonic nanoantennas does not depend on the nonlinear optical susceptibility of the dielectric nanoparticles, but is an effect of the modification of the dielectric environment. Additional experiments show, that a simple combination of two nanoantennas to a nanoantenna system, resonant for both, the incoming pump light field and the generated light, provides not only a strong enhancement of the second harmonic generation efficiency but also offers control over the polarization properties of the generated second harmonic light.

Inspired by the results from double resonant nanoantenna systems, plasmonic nanostructures, which show only a resonance for the generated second harmonic light are investigated. By comparing a series of nanoantenna arrays, owning spectral distinct plasmonic resonances, it is shown, that the second harmonic generation efficiency of these structures is strongly dependent and resonantly enhanced by these two-photon resonances. This result is qualitatively and in part also quantitatively explained in a metamaterial picture, connecting the results of linear extinction spectroscopy with those of second harmonic spectroscopy measurements via an anharmonic oscillator model. Furthermore noncentrosymmtric nanostructures resonant for the generated light are studied. This study indicates that the general symmetry selection rules for second harmonic generation can be also applied to plasmonic nanostructures. Through a comparison of noncentrosymmtric nanostructures exhibiting strongly distinct linear extinction spectra the previous result is reinforced, that a further enhancement of the second harmonic generation efficiency is possible by designing nanostructures, which are not only resonant for either the pump or the generated second harmonic light, but for both.

Contents

1

Introduction

...colours which appear through the prism are to be derived from the light of the white one...[1]

Sir I. Newton explained the appearance of the magnificent colours of the rainbow or flower petals by proposing that the white sunlight, or that of any thermal light source, is actually composed of all colours and can be separated into those [1]. He concluded that the rainbow originates from a colour selective refraction of light and that the petal colour is due to a colour selective absorption of light. This actually means, that the colour of light, or to use a more mathematical language, its frequency, is not converted by light matter interactions. Newton even gave a hint to the microscopic mechanism of the light matter interactions, as he stated that, *"... Light [acts] upon Bodies... putting their parts into a vibrating motion..."*[1]. More than a hundred years later, H. A. Lorentz was able to completely explain those light matter interactions, by describing this *"vibrating motion"* as an oscillation of electrons in the harmonic potential of the atomic cores [2].

Like any oscillating or vibrating system those electrons bound to the atomic core will show an inherent resonance. That means, if the system is periodically excited by an external force, the amplitude of the oscillation will depend on the frequency of the excitation and will show a maximum, when the excitation frequency matches the eigen- or resonance frequency of the system. By accepting light to be an electromagnetic wave,[1] which excites those oscillations, it becomes evident, that light matter interactions are strongly frequency dependent. Hence, it should be possible to engineer the optical response of matter by manipulating the resonance frequency of its constituents, i.e., the atoms.

Very similar to atoms, subwavelength sized metallic structures respond frequency selective to an electromagnetic wave with a collective electron oscillation, called plasmonic resonance [3–5]. But in contrast to atoms, the resonance of those plasmonic structures depends on their geometry and can thus be engineered. By turning from optical to radiowave frequencies one realizes that subwavelength metallic objects are a very common tool for the manipulation of electromagnetic waves since the end of the nineteenth century. The antennas used in the pioneering experiments of H. Hertz and G. Marconi [6, 7] and enabling our modern ways of wireless communication, are also subwavelength metallic objects merely for six orders of magnitude longer wavelengths. But it needed the development of high precision nano-fabrication techniques in the last decades to controlled manufacture nanometer sized

[1] Actually Newton refused the theory of light being a wave, but that is another story.

metallic structures [8], which exhibit resonances in the near-infrared and even in the visible spectral regime [9, 10]. This analogy between radiowave antennas and plasmonic nanostructures gives also an indication of an important property of the latter. When H. Hertz proved the existence of electromagnetic waves, he used an antenna to convert a free propagating wave with a wavelength of around one meter to a spark ignition in a micrometer gap [6]. This actually corresponds to focussing into a deep subwavelength volume, not possible with classic refractive optics [11], resulting in an enormous local field enhancement.

Roughly twenty years ago Sir J. B. Pendry et al. came up with the concept of not using matter composed of real atoms to influence light, but materials consisting of densely periodic arranged, plasmonic structures, so-called metamaterials [12, 13]. The idea behind this concept is, that the light does not resolve the response of the individual constituents, as they are much smaller and denser packed than the wavelength of light, but experiences a collective response of those. With the concept of metamaterials it was actually possible to realize light matter interactions not encountered in nature, e.g., magnetism at optical frequencies [14–16], a negative refractive index [17–19], or electromagnetic invisible cloaks [20–22].

In 1961, Newton's finding, that the frequency of light is inalterable by light matter interactions, was refuted. P. Franken et al. demonstrated, that the interaction between a wave with high intensity and coherence, and a medium lacking inversion symmetry leads to the generation of a new wave with twice the frequency of the original one [23], i.e., second harmonic generation. Even with the use of the only shortly before invented laser [24], representing a monochromatic light source with an intensity and coherence not encountered in nature, this effect was so weak, that the faint spot on the photoplate, resulting from the generated second harmonic light, was removed during the editorial process of the corresponding publication [25]. Second harmonic generation was only the first observed nonlinear optical process out of a plethora [26], but it is still very well suited to investigate the basic properties of nonlinear optical processes in general. By investigating second harmonic generation it was for example shown, that the conversion efficiency of nonlinear processes is completely determined by both, the magnitude of the (linear) optical response at the generated and the original frequencies and that the employed material has to lack inversion symmetry to show second harmonic generation [23, 27, 28].

The term nonlinear optics in contrast to the former discussed linear optics can be understood from the microscopic origin. If the electron oscillation, responsible for the optical response of matter, is excited by strong electric fields, its amplitude can get so strong, that the atomic potential can not be modelled as harmonic any more. Instead an anharmonic potential describing a restoring force with a nonlinear dependency on the electron displacement has to be taken into account [29]. Therefore strong electric fields are mandatory to observe nonlinear processes. By this it becomes evident, that due to their inherent local field enhancement plasmonic nanostructures and metamaterials consisting of those are promising candidates to enhance nonlinear light matter interactions [13] and also give rise to nonlinear wave interactions themselves [30, 31]. This opened the very active research field of nonlinear plasmonics. Here, several strategies to achieve high conversion efficiencies have been investigated e.g., the comparison of differently shaped nanostructures [32, 33], the combination of metallic nanostructures and nonlinear dielectrics [34, 35], variation of the nanostructure arrangement [36], or the combination of so called "acitve" and "passive" structures [37]. But several aspects are still topics of discussions, as for example how plasmonic nanostruct-

ures interact with nanoscale nonlinear matter [38, 39] or how plasmonic resonances for the generated frequency influence nonlinear processes in plasmonic nanostructures [40–42].

In the majority of the previous quoted studies the nonlinear interactions were analysed at a fixed excitation frequency. This is somehow surprising, as the inherent local field enhancement of plasmonic nanostructures is a resonant effect and the basic idea behind these structures is to obtain engineerable light matter interactions by tailoring their resonances. Accordingly a strongly frequency dependent nonlinear response can be expected. To elucidate this connection, it is advisable to not only compare structures with distinct resonances, but to study the linear as well as the nonlinear interactions as a function of frequency. This technique is in general termed spectroscopy [43]. Indeed, the above mentioned discussions arose from the results of nonlinear spectroscopic studies [39, 40], which are contradictory to studies at fixed frequencies [38, 41]. In the case of linear interactions spectroscopy can be conducted with thermal light sources or just the sun light, as in Newton's studies [44]. But when it comes to nonlinear interactions a spectral intensity and coherence is needed to observe these processes, which can be only achieved by lasers. As the tunability of lasers is strongly limited by the gain bandwidth of the respective active material, a common approach is to convert the highly intense and coherent radiation of a laser to new frequencies. In this thesis an optical parametric generator, based on a macroscopic bulk crystal, has been designed and used to perform second harmonic generation spectroscopy of plasmonic nanostructures.

Outline of this Thesis

This thesis deals with the spectroscopic investigation of second harmonic generation from plasmonic nanostructures and metamaterials. In the first part of chapter 2 the linear interaction mechanism between light and matter starting from Maxwell's equations will be reviewed. This paves the way to allow an understanding of the basic properties of plasmonic nanostructures and metamaterials, summed up under the heading Nanoplasmonics, discussed in the second part. In the last part of chapter 2 nonlinear optics of second order in general will be reviewed for a deeper understanding of the experimental results in the later chapters.

In chapter 3 the light source, which will be used for the later experiments will be presented. Based on the process of optical parametric generation a novel frequency converter design was implemented and analysed.

Chapter 4 will cover the linear and nonlinear spectroscopic investigation of plasmonic nanostructures and metamaterials. In the first part the technique used to fabricate those will be explained in detail. In the second part the interplay of gap nanoantennas and dielectric nanoparticles will be examined, with respect to their second harmonic generation efficiency. Here, both dielectrics with and without nonlinear properties will be used to determine the origin of the nonlinearity of the hybrid plasmonic dielectric nanostructures. In the last part, second harmonic generation from metamaterials will be studied, which are composed of plasmonic structures that only exhibit a two-photon resonance, i.e., a plasmonic resonance for the generated light.

This thesis is finally concluded in chapter 5 and an outlook into possible future researches is given.

2

Fundamentals

In the following chapter the theoretical background of this thesis will be presented to the reader. As this thesis deals with the interaction between electromagnetic waves and matter, both artificial and natural, this chapter will start with the most basic description of electromagnetism, which is given by Maxwell's equations. Based on these, microscopic phenomenological models for dielectrics and metals will be presented in the first part of this chapter to finally understand the linear interaction between electromagnetic waves and plasmonic nanostructures or metamaterials. In the second part of this chapter the nonlinear interaction between electromagnetic waves and matter will be discussed, which is the basis of both the investigation of nonlinear plasmonics and the provision of a suitable light source for this purpose.

2.1 Maxwell's equations and consequences

The properties of electromagnetic fields in media are thoroughly described by a set of equations, derived by James Clark Maxwell in 1864. They read [45]:

$$\nabla \cdot \boldsymbol{D}(\boldsymbol{r},t) = \rho(\boldsymbol{r},t) \tag{2.1}$$

$$\nabla \cdot \boldsymbol{B}(\boldsymbol{r},t) = 0 \tag{2.2}$$

$$\nabla \times \boldsymbol{E}(\boldsymbol{r},t) = -\frac{\partial \boldsymbol{B}(\boldsymbol{r},t)}{\partial t} \tag{2.3}$$

$$\nabla \times \boldsymbol{H}(\boldsymbol{r},t) = \boldsymbol{j}(\boldsymbol{r},t) + \frac{\partial \boldsymbol{D}(\boldsymbol{r},t)}{\partial t} \tag{2.4}$$

here and throughout this thesis $\boldsymbol{D}(\boldsymbol{r},t)$ denotes the dielectric displacement, $\boldsymbol{B}(\boldsymbol{r},t)$ the magnetic induction, $\boldsymbol{E}(\boldsymbol{r},t)$ the electric field, $\boldsymbol{H}(\boldsymbol{r},t)$ the magnetic field, and $\rho(\boldsymbol{r},t)$ and $\boldsymbol{j}(\boldsymbol{r},t)$ the external charge and current densities. Internal charge separations and currents lead to a macroscopic electric polarization $\boldsymbol{P}(\boldsymbol{r},t)$ and magnetization $\boldsymbol{M}(\boldsymbol{r},t)$, that can be connected to the quantities mentioned before via the constitutive equations [11]:

$$\boldsymbol{D}(\boldsymbol{r},t) = \epsilon_0 \boldsymbol{E}(\boldsymbol{r},t) + \boldsymbol{P}(\boldsymbol{r},t) \tag{2.5}$$

$$\boldsymbol{B}(\boldsymbol{r},t) = \mu_0 \boldsymbol{H}(\boldsymbol{r},t) + \boldsymbol{M}(\boldsymbol{r},t) \tag{2.6}$$

with $\epsilon_0 = 8.85 \times 10^{-12}$ F/m the permittivity in free space and $\mu_0 = 4\pi \times 10^{-7}$ N/A^2 the permeability in free space. These two natural constants can be connected to the speed of light in vacuum $c_0 = 1/\sqrt{\mu_0 \epsilon_0}$.

By applying a rotation on equation (2.3) and combining equation (2.1) and (2.4) with the constitutive equations (2.5) and (2.6) we achieve:

$$-\nabla^2 \boldsymbol{E}(\boldsymbol{r},t) + \frac{1}{c_0^2}\frac{\partial^2 \boldsymbol{E}(\boldsymbol{r},t)}{\partial t^2} = -\frac{\partial}{\partial t}\left(\mu_0 \boldsymbol{j}(\boldsymbol{r},t) + \mu_0 \frac{\partial \boldsymbol{P}(\boldsymbol{r},t)}{\partial t} + \nabla \times \boldsymbol{M}(\boldsymbol{r},t)\right) \tag{2.7}$$

which is known as the inhomogeneous wave equation for the electric field. The left hand side of equation (2.7) represents the homogeneous wave equation for the electric field in vacuum. Whereas the terms on the right hand side act as source terms. From this we can distinguish two types of sources: (i) the external source current density $\boldsymbol{j}(\boldsymbol{r},t)$ and (ii) $\mu_0 \frac{\partial \boldsymbol{P}(\boldsymbol{r},t)}{\partial t}$ and $\nabla \times \boldsymbol{M}(\boldsymbol{r},t)$ as polarization and magnetization current density, respectively. The latter describe the interaction of electromagnetic radiation with matter. By restricting ourselves to dielectric or metallic but nonmagnetic materials, the magnetization $\boldsymbol{M}(\boldsymbol{r},t)$ can be neglected and is set equal to zero. If we assume a vanishing external charge density $\rho(\boldsymbol{r},t)$ and external current density $\boldsymbol{j}(\boldsymbol{r},t)$, i.e., all external sources which primary generate, e.g., the incoming electromagnetic fields are located outside our considered spatial domain, equation (2.7) further simplifies to:

$$\nabla^2 \boldsymbol{E}(\boldsymbol{r},t) - \frac{1}{c_0^2}\frac{\partial^2 \boldsymbol{E}(\boldsymbol{r},t)}{\partial t^2} = \mu_0 \frac{\partial^2 \boldsymbol{P}(\boldsymbol{r},t)}{\partial t^2} \tag{2.8}$$

So far, the above derivation of the wave equation (2.8) in matter was carried out in the spatial and the temporal domain. For the following considerations it is more convenient to switch to a frequency domain description. Hence, we define the Fourier transform between the temporal and the frequency domain for the electric field $\boldsymbol{E}(\boldsymbol{r},t)$ as [45]:

$$\boldsymbol{E}(\boldsymbol{r},\omega) = \int_{-\infty}^{\infty} \boldsymbol{E}(\boldsymbol{r},t) \mathrm{e}^{\imath\omega t} dt \tag{2.9}$$

$$\boldsymbol{E}(\boldsymbol{r},t) = \frac{1}{2\pi}\int_{-\infty}^{\infty} \boldsymbol{E}(\boldsymbol{r},\omega) \mathrm{e}^{\imath\omega t} d\omega \tag{2.10}$$

With this we obtain the wave equation in matter in the frequency domain:

$$\nabla^2 \boldsymbol{E}(\boldsymbol{r},\omega) + \frac{\omega^2}{c_0^2}\boldsymbol{E}(\boldsymbol{r},\omega) = -\mu_0 \omega^2 \boldsymbol{P}(\boldsymbol{r},\omega) \tag{2.11}$$

Obviously the polarization $\boldsymbol{P}(\boldsymbol{r},\omega)$ in the medium is a function of the electric field $\boldsymbol{E}(\boldsymbol{r},\omega)$ and can therefore be written as a power series of the electric field $\boldsymbol{E}(\boldsymbol{r},\omega)$ [29]. At first we will only consider the case of low electric field amplitudes, where the term linear in $\boldsymbol{E}(\boldsymbol{r},\omega)$ is dominating, and all higher order contributions can be omitted. For strong field amplitudes those higher order terms can of course not be neglected any more and will lead to several

interesting effects, which will be discussed in section 2.4 about nonlinear optics.[1] Hence, in the limiting case of linear optics the polarization $\boldsymbol{P}(\boldsymbol{r},\omega)$ can be expressed by:

$$\boldsymbol{P}(\boldsymbol{r},\omega) = \epsilon_0 \chi^{(1)}(\omega)\boldsymbol{E}(\boldsymbol{r},\omega) \tag{2.12}$$

where $\chi^{(1)}(\omega)$ is the first order electric susceptibility. Here, a homogeneous, isotropic material was assumed, which means that $\chi^{(1)}(\omega)$ is a (in our considered spatial domain) spatially constant scalar function. For anisotropic materials the electric field $\boldsymbol{E}(\boldsymbol{r},\omega)$ and the polarization $\boldsymbol{P}(\boldsymbol{r},\omega)$ are not necessarily parallel, in that case the electric susceptibility must then be written as a tensor of second order: $P_i = \epsilon_0 \sum_{j=1}^{3} \chi_{ij}^{(1)} E_j$. We will limit the following discussion to the case of homogeneous, isotropic materials. By inserting equation (2.12) into the wave equation in frequency domain (2.11) we obtain the Helmholtz equation:

$$\nabla^2 \boldsymbol{E}(\boldsymbol{r},\omega) + (1+\chi^{(1)}(\omega))\frac{\omega^2}{c_0^2}\boldsymbol{E}(\boldsymbol{r},\omega) = \tag{2.13}$$

$$\nabla^2 \boldsymbol{E}(\boldsymbol{r},\omega) + \epsilon_r(\omega)\frac{\omega^2}{c_0^2}\boldsymbol{E}(\boldsymbol{r},\omega) = \tag{2.14}$$

$$\nabla^2 \boldsymbol{E}(\boldsymbol{r},\omega) + \frac{\omega^2}{c^2}\boldsymbol{E}(\boldsymbol{r},\omega) = 0 \tag{2.15}$$

where we defined the relative permittivity $\epsilon_r(\omega) = (1+\chi^{(1)}(\omega))$, which connects the dielectric displacement with the electric field: $\boldsymbol{D}(\boldsymbol{r},\omega)=\epsilon_0\epsilon_r\boldsymbol{E}(\boldsymbol{r},\omega)$. With this the complex refractive index $\tilde{n}^2(\omega) = \epsilon_r(\omega)$, which defines the speed of light in matter $c = c_0/\tilde{n}$, can be defined. Analogous considerations starting from equation (2.4) lead to a wave equation for the magnetic field, the magnetic susceptibility $\chi_m(\omega)$ and the relative permeability $\mu_r(\omega)$. Even as magnetic materials will be not considered in this thesis (and therefore we assume $\mu_r(\omega) = 1$ in the following), it is important to mention, that in general the refractive index is defined as $\tilde{n}^2(\omega) = \epsilon_r(\omega)\mu_r(\omega)$.

Equation (2.15) can be solved by:

$$\boldsymbol{E}(\boldsymbol{r},\omega) = \frac{1}{2}\left[\boldsymbol{E}_0 \mathrm{e}^{\imath(\boldsymbol{k}\cdot\boldsymbol{r}-\omega t)} + cc.\right] \tag{2.16}$$

representing a plane wave oscillating in time with the frequency ω and propagating in the direction of the wave vector $\boldsymbol{k}$, *cc.* denotes the complex conjugate. Inserting the plane wave solution into equation (2.15) leads to the dispersion relation of a free propagating wave:

$$\frac{\omega^2}{|\boldsymbol{k}|^2} = \frac{c_0^2}{\tilde{n}^2} \tag{2.17}$$

In general the refractive index and hence the relative permittivity $\epsilon_r(\omega)$ are complex quantities. Assuming a plane wave propagating in z-direction we obtain:

$$\boldsymbol{k}_z = \frac{\omega}{c_0}\tilde{n}\hat{\boldsymbol{e}}_z = \frac{\omega}{c_0}(n(\omega)+\imath\kappa(\omega))\hat{\boldsymbol{e}}_z \tag{2.18}$$

[1] The term nonlinear optics originates in the nonlinear dependency of the polarization on the electric field.

where $\hat{\boldsymbol{e}}_z$ denotes the unit vector in z-direction. With this the electric field of a plane wave reads:

$$\boldsymbol{E}(z,\omega) = \boldsymbol{E}_0 \cdot \mathrm{e}^{\imath(\frac{\omega}{c_0} n(\omega) z - \omega t)} \cdot \mathrm{e}^{-\frac{\omega}{c_0}\kappa(\omega) z} \tag{2.19}$$

The first exponential function describes an oscillation and thus, the propagation of the wave through a medium is characterized by the real part $n(\omega)$ of the refractive index. The second exponential function describes an exponential decay and thus, the attenuation of the wave through a medium is associated with the imaginary part $\kappa(\omega)$ of the refractive index. Therefore the term refractive index sometimes only refers to the real part n, whereas the imaginary part κ is known as extinction coefficient [46].

2.2 Linear response of matter to electromagnetic waves

As we have seen before, in the limiting case of linear optics the propagation of an electromagnetic wave in a medium can be completely described by the complex refractive index $\tilde{n}(\omega)$, which in turn is given by the electric susceptibility $\chi^{(1)}(\omega)$. Therefore the goal of the next paragraphs is to derive models which provide the frequency dependent electric susceptibility $\chi^{(1)}(\omega)$ for different classes of materials.

2.2.1 Dielectrics as harmonic oscillators

The classical response of atoms to electromagnetic waves can be described in a driven oscillator picture, the so-called Lorentz model [2, 11]. Here, the atom is modelled as an electron which is bound to the atomic core. Applying an oscillating electric field leads to an oscillation of the electron around its rest position. For low light intensities, the electrons can be regarded as bound in a harmonic potential. Therefore the equation of motion in one dimension for a single electron driven by the electric field $E_0\mathrm{e}^{-\imath\omega t}$ is given by:

$$m_e \frac{\partial^2 x(t)}{\partial t^2} + m_e \gamma_\mathrm{L} \frac{\partial x(t)}{\partial t} + m_e \omega_0^2 x(t) \quad = \quad -eE_0\mathrm{e}^{-\imath\omega t} \tag{2.20}$$

where $x(t)$ is the displacement of the electron, γ_L the damping constant, ω_0 the resonance frequency, $e = 1.6 \times 10^{-19}$ As the elementary charge and $m_e = 9.1 \times 10^{-31}$ kg the electron mass. Here, we assume the incident plane wave to be polarized in x-direction: $\boldsymbol{E}(\boldsymbol{r},t) = \hat{\boldsymbol{e}}_x E_0 \mathrm{e}^{\imath(\boldsymbol{k}\cdot\boldsymbol{r}-\omega t)}$. The steady state solution of equation (2.20) is given by $x(t) = a(\omega)\mathrm{e}^{-\imath\omega t}$ leading to the electric dipole moment of a harmonic oscillator:

$$p(t) = -ex(t) = \frac{e^2}{m_e} \frac{1}{(\omega_0^2 - \omega^2 - \imath\gamma_\mathrm{L}\omega)} E_0 \mathrm{e}^{-\imath\omega t} \tag{2.21}$$

Thus, the electric dipole moment is proportional to the electric field. The proportionality factor $\alpha(\omega)$ is called polarizability. With a number of n_e oscillating electrons per atom it

reads:

$$\alpha(\omega) = \frac{n_e e^2}{m_e} \frac{1}{(\omega_0^2 - \omega^2 - \imath\gamma_{\mathrm{L}}\omega)} \tag{2.22}$$

If we consider only atoms of the same type with polarizability $\alpha(\omega)$, arranged with a constant density n_a, we obtain with the electron number density $N_e = n_e \cdot n_a$ the macroscopic polarization $P(\omega)$:

$$P(\omega) = n_a \alpha(\omega) E(\omega) = \epsilon_0 \chi(\omega) E(\omega) \tag{2.23}$$

In the case of a real dielectric we have to consider different types of atoms not necessarily obeying the same microscopic polarizability $\alpha(\omega)$. For an ordered crystal consisting of a finite number N of types of atoms, the macroscopic polarization $P(\omega)$ can be written as:

$$P(\omega) = E(\omega) \sum_{\nu=1}^{N} \frac{n_e e^2}{m_e} \frac{f_\nu}{(\omega_{0,\nu}^2 - \omega^2 - \imath\gamma_{\mathrm{L},\nu}\omega)} \tag{2.24}$$

where the oscillator strength f_ν has to satisfy the sum rule $\sum_{\nu=1}^{N} f_\nu = n_a$. Here, we neglect all modifications due to interaction between the atoms. This approximation holds true for diluted gases but breaks down when the atoms are densely packed such that the electronic wave functions overlap and form electronic bands. Nevertheless, even for this case we can define a new effective polarizability of the same form leading to a qualitatively good description of the linear optical properties of nonmetallic solids. For this new effective polarizability, coupled atomic potentials have to be taken into account and not isolated atoms.

In the previous discussion only the one dimensional case was considered, i.e., electrons oscillating parallel to the applied electric field. As mentioned in section 2.1 both the macroscopic polarization $\boldsymbol{P}(\omega)$ and the applied electric field $\boldsymbol{E}(\omega)$ have a vectorial character and therefore the macroscopic susceptibility has to be written as a tensor: $P_i(\omega) = \epsilon_0 \sum_{j=1}^{3} \chi_{ij} E_j(\omega)$. However, for isotropic media, e.g., ordered crystals consisting of finite types of atoms, there is always a coordinate system, called the principal axis system, in which χ is diagonal. With the use of this coordinate system the individual diagonal components χ_{ii} can then be evaluated analogously to the one dimensional case [47].

With the most simple approximation given by (2.22) and (2.23) we can calculate the real and the imaginary part of the complex refractive index:

$$n(\omega) = 1 - \frac{1}{2} \frac{e^2 N_e}{\epsilon_0 m_e} \frac{\omega^2 - \omega_0^2}{(\omega^2 - \omega_0^2)^2 + \gamma_{\mathrm{L}}^2 \omega^2} \tag{2.25}$$

$$\kappa(\omega) = \frac{1}{2} \frac{e^2 N_e}{\epsilon_0 m_e} \frac{\gamma_{\mathrm{L}}\omega}{(\omega^2 - \omega_0^2)^2 + \gamma_{\mathrm{L}}^2 \omega^2} \tag{2.26}$$

For dielectric crystals modelled with a single Lorentz oscillator the resonance frequency ω_0 can be identified with the band gap energy, which is typically located in the ultraviolet (isolators) up to the near-infrared region (semi-conductors). If the frequency ω is increased towards the resonance frequency ω_0 we obviously get an overall increase of the susceptibility and thus the complex refractive index, but this increase is connected to a strongly enhanced absorption.

2.2.2 Metals in the Drude model

In the case of metallic materials, in contrast to the previously discussed case of dielectric materials, at least a part of the electrons is not bound to a specific atom. Therefore, these so-called conduction electrons can be treated in a basic microscopic model of metals as individual freely moving electrons. It is called the free electron model or the Drude model of metals [48]. Of course, the conduction electrons are not perfectly free in a metal and different scattering events, like scattering at lattice defects, electron-electron scattering or electron-phonon scattering, lead to an effective damping of the freely moving electrons. In the Drude model this damping is described by the damping parameter $\gamma_D = 1/\tau$, where τ describes the average time between two scattering events. The equation of motion for the Drude model can be directly obtained from that for the Lorentz model (2.20). For this the resonance frequency ω_0 is set to zero, due to the lack of the restoring force resulting from the binding to the atomic core:

$$m_e \frac{\partial^2 x(t)}{\partial t^2} + m_e \gamma_D \frac{\partial x(t)}{\partial t} = -eE_0 \mathrm{e}^{-\imath\omega t} \tag{2.27}$$

In analogy to the Lorentz oscillator model the electric susceptibility and the relative permittivity $\epsilon(\omega)$ of the Drude model can be derived:

$$\chi(\omega) = -\frac{\omega_p^2}{\omega(\omega + \imath\gamma_D)} \tag{2.28}$$

$$\epsilon(\omega) = 1 - \frac{\omega_p^2}{\omega(\omega + \imath\gamma_D)} \tag{2.29}$$

Here, the bulk metal plasma frequency $\omega_p = \sqrt{\frac{e^2 N_e}{\epsilon_0 m_e}}$ was introduced. Starting from equation (2.29) some basic properties for metals can be deduced. In the visible and near-infrared spectral regime the frequency ω is much larger than the Drude damping constant γ_D, but still smaller than the plasma frequency ω_p [49]. Therefore, the imaginary part of $\epsilon(\omega)$ can be neglected and the real part becomes negative. Thus, the complex refractive index $\tilde{n}(\omega)$ gets purely imaginary, meaning that no wave propagation but only evanescent waves are allowed in the metal. Therefore, a plane wave gets fully reflected at the interface of the metal. The $1/e$ decay length of the evanescent wave into the metal, called skin depth, defined via equation (2.19) is for the discussed spectral regime in the order of some ten nanometers.

The Drude model is a fairly good description of the behaviour of metals at frequencies in the near-infrared region. For shorter wavelengths (higher energies) one has to account for excitations of electrons from lower bands into the conduction band, i.e., interband transitions [50]. These interband transitions occur for example in gold at an energy of 2.38 eV (522 nm), where an electron from the 5d-band (valence band) is excited into the 6s-band (conduction band). To improve the description of the permittivity for shorter wavelengths, a common ansatz is to combine the Drude model with Lorentz oscillators. The susceptibility corresponding to these excitations is then just added to the Drude permittivity.

2.2.3 Surface plasmon polaritons

Up to now we have discussed free propagating waves. But for an interface between two materials, with relative permittivities ϵ_1 and ϵ_2, lying in the xy-plane equation (2.14) can be solved by an ansatz of the form [5]:

$$\boldsymbol{E} = \boldsymbol{E}_0 \mathrm{e}^{-i(k_x x + k_z z - \omega t)} \tag{2.30}$$

The boundary conditions lead to

$$\frac{k_{z1}}{\epsilon_1} + \frac{k_{z2}}{\epsilon_2} = 0 \tag{2.31}$$

and

$$k_x^2 + k_{zi}^2 = \epsilon_i \left(\frac{\omega}{c_0}\right)^2 \qquad i = 1,2 \tag{2.32}$$

Solving these two equations, the dispersion relation is given by:

$$k_x = \frac{\omega}{c_0}\left(\frac{\epsilon_1 \epsilon_2}{\epsilon_1 + \epsilon_2}\right)^{1/2} \tag{2.33}$$

$$k_{z,i} = = \frac{\omega}{c_0}\left(\frac{\epsilon_i^2}{\epsilon_1 + \epsilon_2}\right)^{1/2} \qquad i = 1,2 \tag{2.34}$$

If we consider now a metal ($i = 1$) isolator ($i = 2$) interface in the visible spectral regime, i.e., $|\Im[\epsilon_1(\omega)]| \ll |\Re[\epsilon_1(\omega)]|$, $\Re[\epsilon_1(\omega)] \ll 0$, $\Im[\epsilon_2(\omega)] \ll \Re[\epsilon_2(\omega)]$ and $|\epsilon_1(\omega)| \gg |\epsilon_2(\omega)|$, we obtain a propagation in x-direction and an evanescent decay in z-direction, as depicted in Figure 2.1. Thus, we deal with a wave travelling along the interface with exponentially decaying fields into the metal and the isolator, the so-called surface plasmon polariton (SPP).

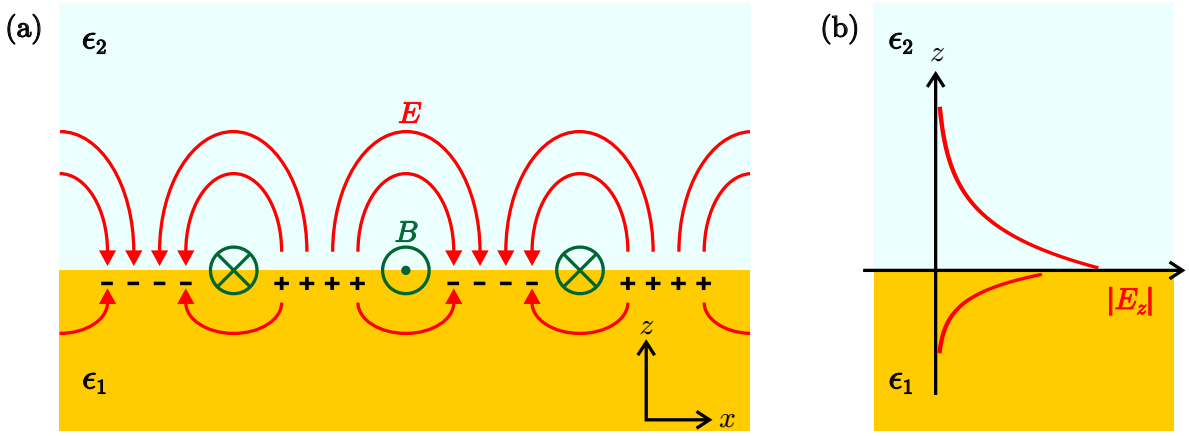

Figure 2.1: *(a) Schematic view of a surface plasmon polariton, bound to the interace between a metal (ϵ_1) and a dielectric (ϵ_2). The charges (+/-) as well as the electromagnetic fields are shown (red/green). (b) The perpendicular field $|E_z|$ decays exponentially into the the metal and the dielectric.*

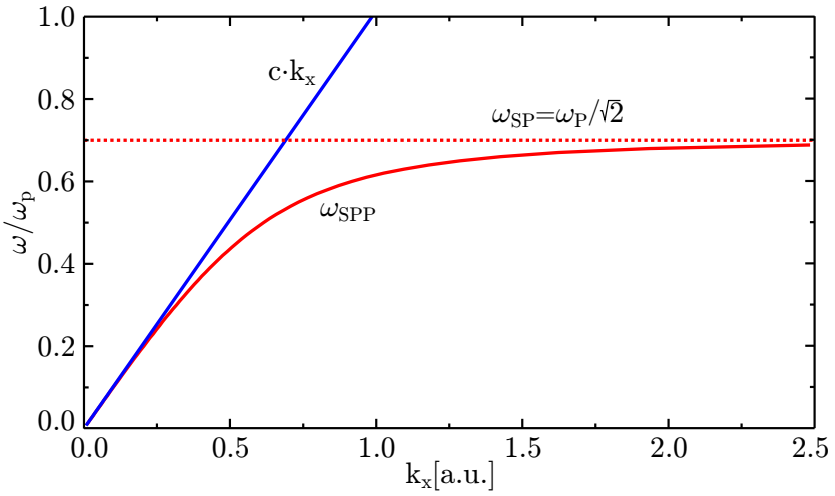

Figure 2.2: *The solid red line represents the dispersion relation for a surface plasmon polariton (SPP) traveling along a Drude-metal-vacuum interface. The blue line is the light line, that is, the free-space dispersion of electromagnetic waves. The dotted red line corresponds to the surface plasma (SP) frequency.*

In Figure 2.2 the dispersion relation of a SPP travelling along a metal-vacuum interface is shown. Here we see, that for low frequencies the dispersion relation of a SPP converges towards the free-space dispersion $\omega = ck$ of electromagnetic waves, while for high frequencies it approaches a horizontal line, given by $\omega_{\mathrm{SP}} = \omega_{\mathrm{pl}}/\sqrt{(1+\epsilon_2)}$, the so-called surface plasma (SP) frequency. While approaching towards the surface plasma frequency the imaginary part of the wavevector along the propagation direction $\Im[k_x]$ strongly increases, thus the SPP experiences higher losses for higher frequencies, additional to the effect that the losses of metals in general are increased towards the plasma frequency [5, 49].

Two important features of SPPs occur if the propagation length and the skin (decay) length into the metal and the dielectric are considered. The $1/e$ propagation length of a SPP is just given by $1/\Im[k_x]$. For a realistic gold vacuum interface at a wavelength of 633 nm ($\epsilon_1 = -11.6 + i1.2$ and $\epsilon_2 = 1$ [49]) we obtain a propagation length of roughly 10 µm, which is only an order of magnitude larger than the wavelength. Below the surface plasma frequency the skin length $1/k_{z,i}$ is given by equation (2.34) as k_z is purely imaginary. For the same situation as before this results in a decay length into the vacuum of approximately 330 nm and in a decay length into the gold of 28 nm. Thus a SPP is strongly localized at the metal dielectric interface, but can only propagate quite a short distance.

2.3 Nanoplasmonics

After the introduction to the optics of bulk metals in the last paragraph, we will now turn to the optical properties of metal nanoparticles. Here, we will start with a brief overview of the interaction of electromagnetic waves with metal nanoparticles in general, which will include a derivation of the title of this section: Nanoplasmonics. This overview will help us to understand the optical properties of the specific geometries, which will be investigated in this thesis. As it is not possible to solve Maxwell's equations analytically for arbitrary nanoparticle geometries, a non-commercial numerical program package,[2] based on the discontinuous Galerkin time domain method [51, 52] will be used to evaluate near-field distributions and plasmonic resonances if necessary. However, due to the need of actual modelling the geometries, these evaluations will only cover the limiting case of idealized geometries. Finally we will treat the collective response of densely arranged metal particles, the so-called metamaterials, to electromagnetic waves.

2.3.1 Optical properties of metal nanoparticles

As was seen before, an external electric field accelerates the conduction band electrons in a metal in one direction. In a small metal particle, the free moving electrons thus travel to one side of the particle and form a negative charge density. On the opposite side of the particle the positive background remains and forms a positive charge density. This charge separation gives rise to an electric field and a restoring force, like in a mass spring system (see Figure 2.3), acting on the electrons, resulting in a coherent plasma oscillation [3] comparable to that of electrons bound to a atom, which was discussed in section 2.2.1. Due to the confinement to the metal particle, one refers to this oscillation as a particle plasmon or a localized surface plasmon in analogy with the surface plasmon polariton [4]. Hereby it becomes evident that the term Nanoplasmonics refers to the optics of metal nanoparticles in general.

The simplest approximation of an arbitrary shaped nanoparticle is a small metal sphere with radius a embedded in a dielectric medium with dielectric constant ϵ_m. If the size of the considered metal particles is reduced drastically down below the wavelength of the electromagnetic wave, the electric field interacting with a single particle becomes quasi-static. Within the quasi static approximation, i.e., the electromagnetic wave has a constant spatial phase along the particle, an analytical expression for the polarizability $\alpha(\omega)$ is given by [4]:

$$\alpha(\omega) = 4\pi a^3 \frac{\epsilon(\omega) - \epsilon_m(\omega)}{\epsilon(\omega) + 2\epsilon_m(\omega)} \tag{2.35}$$

where $\epsilon(\omega)$ is the relative permittivity of the metal and $\epsilon_m(\omega)$ that of the surrounding dielectric. On the one hand, we can see that the polarizability is proportional to the third power of the radius a and hence to the volume of the metal sphere. On the other hand, it is proportional to a fractional term which contains the dielectric constants of the metal sphere and the surrounding. This term can exhibit a resonance if the denominator becomes zero.

[2] Developed in the group of Prof. Dr. Kurt Busch at Karlsruhe Institute of Technology (KIT), Karlsruhe, Germany.

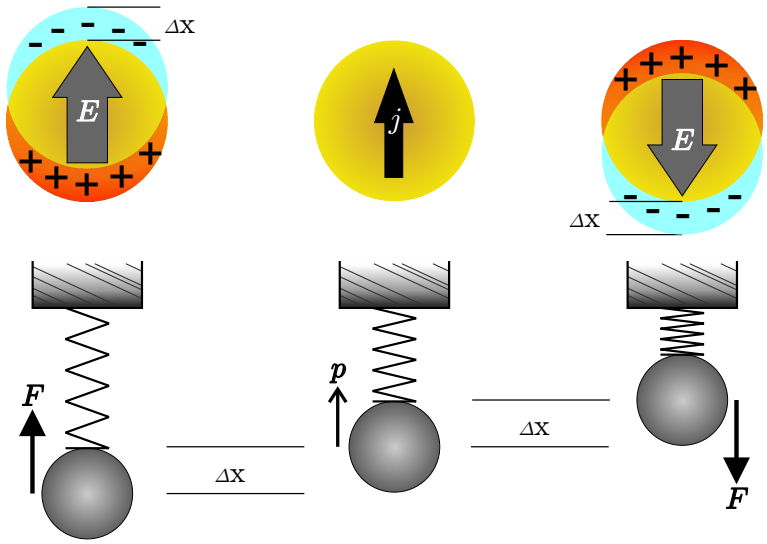

Figure 2.3: *(Upper row) Sketch of a metallic nanoparticle whose electron cloud has been displaced by Δx, due to an external oscillating electric field, e.g., an electromagnetic wave, giving rise to an internal electric field $\boldsymbol{E}$. (Lower row) Mechanical analogue of a mass attached to affixed spring. The restoring force $\boldsymbol{F}$ corresponds to the internal electric field $\boldsymbol{E}$, and the momentum $\boldsymbol{p}$ to the electron current $\boldsymbol{j}$, respectively.*

In the case of small damping in the metal, we can neglect for the moment the imaginary part of the dielectric constant $\epsilon(\omega)$ of the metal sphere. The resonance then appears for $\Re[\epsilon(\omega)] = -2\epsilon_m(\omega)$, which is called Fröhlich condition [4]. When we use a Drude model for the dielectric constant of the metal, as introduced in paragraph 2.2.2, the resonance frequency ω_0 can be calculated for a sphere located in air ($\epsilon_m(\omega) = 1$) to $\omega_0 = \omega_p/\sqrt{3}$.

Within the quasi-static approximation, we can also deal with ellipsoidal particles with the principal axes a, b, and c. In this formalism, the principal axes of the ellipsoids are represented by the normalized geometry parameters F_i, with $i = 1$, 2, and 3, and $\sum_i F_i = 1$. Clearly, we obtain a tensorial polarizability leading to a vectorial equation for the polarization:

$$\begin{pmatrix} p_x \\ p_y \\ p_z \end{pmatrix} = \epsilon_m(\omega) \begin{pmatrix} \alpha_1 & 0 & 0 \\ 0 & \alpha_2 & 0 \\ 0 & 0 & \alpha_3 \end{pmatrix} \begin{pmatrix} E_{0,x} \\ E_{0,y} \\ E_{0,z} \end{pmatrix} \tag{2.36}$$

Here, we assumed that the principal axes of the ellipsoidal particle are aligned along the unit vectors of the Cartesian coordinate system. For the elements of the polarization tensor, we obtain:

$$\alpha_i = \frac{\epsilon(\omega) - \epsilon_m(\omega)}{\epsilon_m(\omega) + (\epsilon(\omega) - \epsilon_m(\omega))F_i} V_{\text{ellipsoid}} \tag{2.37}$$

with $V_{\text{ellipsoid}}$ representing the volume of the ellipsoid. Here, the Fröhlich condition gives a geometry dependent resonance frequency of the particle due to the geometry parameter F_i.

Another inherent feature connected with the plasmonic resonances of metal nanoparticles is the enhancement of the near field around the particle. The intensity of the local field $I_{\text{loc}} \propto |E_{\text{loc}}|^2$ compared to the incoming field $I_0 \propto |E_0|^2$ differs by the frequency dependent enhancement factor $L(\omega)$ [4]:

$$I_{\text{loc}} = L(\omega)I_0 = L_{\text{SP}}(\omega)L_{\text{LR}}I_0 \tag{2.38}$$

Two physical effects are responsible for the field enhancement. The so-called lightning rod effect is responsible for the frequency independent contribution L_{LR} and is strongly depending on the geometrical shape of the particle. The electric field on the surface of a perfect conductor points perpendicular to the surfaces normal, therefore leading to a concentration of the electromagnetic field to areas of sharp edges or tips. The frequency dependent part $L(\omega)_{\mathrm{SP}}$ is due to the resonant excitation of localized surface plasmons in the structure and essentially resembles the polarizability $\alpha(\omega)$.

Additionally the efficiency of scattering and absorption of light by metal nanoparticles becomes resonantly enhanced. For small particles which are much smaller than the wavelength λ of light, the scattering and absorption cross sections C_{sca} and C_{abs}, defining the extinction cross section $C_{\mathrm{ext}} = C_{\mathrm{abs}} + C_{\mathrm{sca}}$, become [3, 4]:

$$C_{\mathrm{abs}} = \frac{k}{\epsilon_0}\Im(\alpha) \sim a^3 \tag{2.39}$$

$$C_{\mathrm{sca}} = \frac{k^4}{6\pi\epsilon_0^2}|\alpha|^2 \sim a^6 \tag{2.40}$$

where $k = |\boldsymbol{k}|$ is the wavenumber. Due to the dependency of the particle size a we see, that for very small particles the extinction is dominated by absorption.

Before we turn to the specific geometries, which will be investigated in this thesis, we shortly want to recapitulate the results of this paragraph:

i An increase of $\epsilon_m(\omega)$, i.e., of the refractive index of the surrounding medium, leads to a decrease of the resonance frequency, i.e., a red-shift.

ii An elongation of the particle along the axis parallel to the incident polarisation leads to a red-shift of the particle's resonance.

iii An elongation of the particle along the axis perpendicular to the incident polarisation leads to a blue-shift of the particle's resonance.

iv A resonant excitation of the particle plasmon leads to a local field enhancement around the particle.

v For very small particles the extinction cross section is dominated by absorption.

2.3.2 Nanoantennas

In general the term antenna refers to a device which can radiate and receive electromagnetic radiation. In this thesis we will refer to antennas, or to be more specific to nanoantennas, as wires with a finite length, and to gap nanoantennas as two finite wires separated by a small gap. These nanoantennas can exhibit resonances in the visible or near-infrared spectral regime. From the radio frequency (RF) regime it is well known, that an electromagnetic wave impinging on a metal wire orientated parallel to the wave's polarization leads to a charge separation oscillating along the wire, like in the case of a metal nanoparticle discussed in the previous section. A resonance in the excitation of those charge oscillations is observed,

when the length of the wire L corresponds to half of the wavelength of the impinging wave in vacuum: $L_{\mathrm{res}} = \lambda_{\mathrm{vac}}/2$. This linear scaling between the length of the antenna and its resonance wavelength, resembles the finding of the previous section where a elongation of metal particle along the axis parallel to the incident polarisation led to a red-shift of the particle's resonance. However, no absolute size scaling for the resonance wavelength was provided by the quasi-static approximation.

Fabry-Perot model

In order to get an understanding of the resonances and eigenmodes of a nanoantenna and of plasmonic nanostructures in general a Fabry-Perot like model will be presented, which will also resemble the findings from the RF regime [10]. In paragraph 2.2.3 the basic properties of surface plasmon polaritons, waves propagating along a metal dielectric surface, were discussed. SPPs are not limited to planar surfaces but can be also found for metal stripes or cylindrical wires. For an infinite long metal cylinder the basic properties of SPPs stay qualitatively the same, thus presenting a kind of plasmonic waveguide. Especially if the limiting case of a large cylinder diameter is considered, the dispersion relation, propagation length and decay length approach the limiting values of a planar interface. But as the diameter is decreased towards the skin length both the imaginary part and the real part of the wavevector k_{SPPM}[3] in propagation direction increase, which means that the propagation length as well as the velocity become smaller. Furthermore it can be shown, that a decrease of the diameter results in a larger confinement of the fields inside the metal wire and therefore increases the losses due to Ohmic damping [53].

A single wire antenna of length L as illustrated in Figure 2.4 can be pictured as a finite piece of such a wire waveguide. The two open ends represent mirror-like discontinuities with a near unity reflection coefficient. In such an one-dimensional cavity, a standing wave builds up once the accumulated phase per round trip equals an integer multiple of 2π, similar to the case of mirror based Fabry-Perot resonator [46]. For plasmonic nanoantennas the fields extend outside the physical boundaries of the metal structure, which results in a phase shift ϕ_R upon reflection [54], that has the same effect as some additional length of propagation [55]. With this, the resonant antenna length L_{res} for the m-th order resonance can be connected to the wavelength of the waveguide mode $\lambda_{\mathrm{SPPM}} = 2\pi/\Re[k_{\mathrm{SPPM}}]$, via the simple relation:

$$L_{\mathrm{res}} \cdot \Re[k_{\mathrm{SPPM}}] + \phi_R \;=\; m\pi \tag{2.41}$$

As, following Figure 2.2, for low, e.g., RF frequencies the dispersion of a SPP approaches that of vacuum, the above equation becomes $L_{\mathrm{res}} = m\lambda_{\mathrm{vac}}/2$, thus resembling the findings from the RF regime. Here, we made the assumption $k_{\mathrm{SPPM}} = k_{\mathrm{SPP}}$, which is justified as for typical RF wavelengths ($\sim$ 1 m) the antenna diameter can be much larger than the skin length still obeying a wire like shape. Additionally ϕ_R can be neglected compared the overall antenna length at RF wavelengths [54].

However, for optical and near-infrared radiation the wavelength of the waveguide mode λ_{SPPM} will be shorter than the wavelength in vacuum, as can be seen from Figure 2.2 and the

[3] In order to distinguish between a SPP on a planer surface and a SPP on guided a cylinder the abbreviation SPPM for surface plasmon polariton mode was introduced.

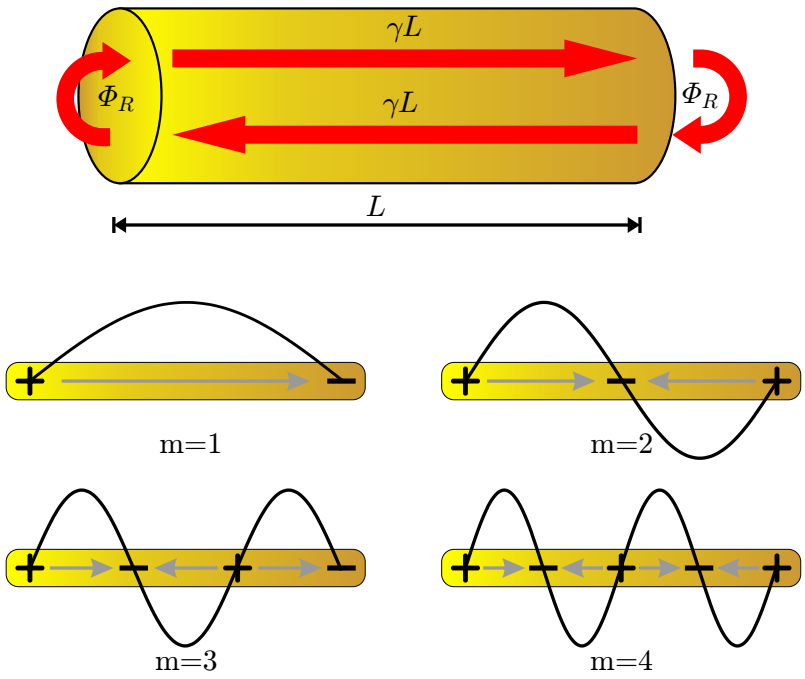

Figure 2.4: *Resonances of a plasmonic nanoantenna. (Upper picture) Sketch of accumulated phase contributions upon propagation and reflection in a truncated wire, leading to Fabry-Perot resonances, with* $\gamma = \Re[k_{\mathrm{SPPM}}]$. *Adapted from [5]. (Lower pictures) Plasmonic modes* $(m = 1 - 4)$ *of a nanoantenna. The grey arrows indicate the direction of the current, the black curves indicate the current density distribution and the charge density maxima are indicated by* $+$ *and* $-$.

above discussion. In order to keep an antenna like shape, i.e., a high aspect ratio between the length and the diameter, nanoantennas will have diameters of some ten nanometers, which is comparable with the skin length, thus λ_{SPPM} gets further decreased and ϕ_R can not be neglected any more. In this thesis we will also not deal with free standing wires in vacuum, but rather, as we will see in section 4.1, with highly curved nanocuboids lying on a glass substrate. But nevertheless, the above presented model provides us with an understanding of the linear connection between the resonant antenna length L_{res} and the wavelength and explains the differences of nanoantennas compared to RF antennas.

In Figure 2.4 the first four plasmonic modes $(m = 1 - 4)$ of a nanoantenna are visualized in terms of the charge distribution, the current direction and the current density distribution. We see, that for even order modes the currents cancel each other out, while for odd order modes a net current survives. By examining the charge distribution it becomes evident, that odd order modes give rise to a dipole moment, but even order modes not. Therefore only odd order modes can be excited by and interact with plane waves.

Gap nanoantennas

Next the case of a gap nanoantenna, i.e., two metallic wires arranged in a row divided by a gap comparable to the wire diameter, will be discussed. For this purpose it is useful to consider again the mechanical mass spring system analogue of a plasmonic resonance depicted in Figure 2.3 [5, 57]. Here, each wire has to be considered as an individual mass spring system with the same resonance frequency. Due to the interaction between the surface charges on the ends of both wires an additional spring needs to be introduced to couple the two systems, as depicted in Figure 2.5. As known from classical mechanics, the coupling of the

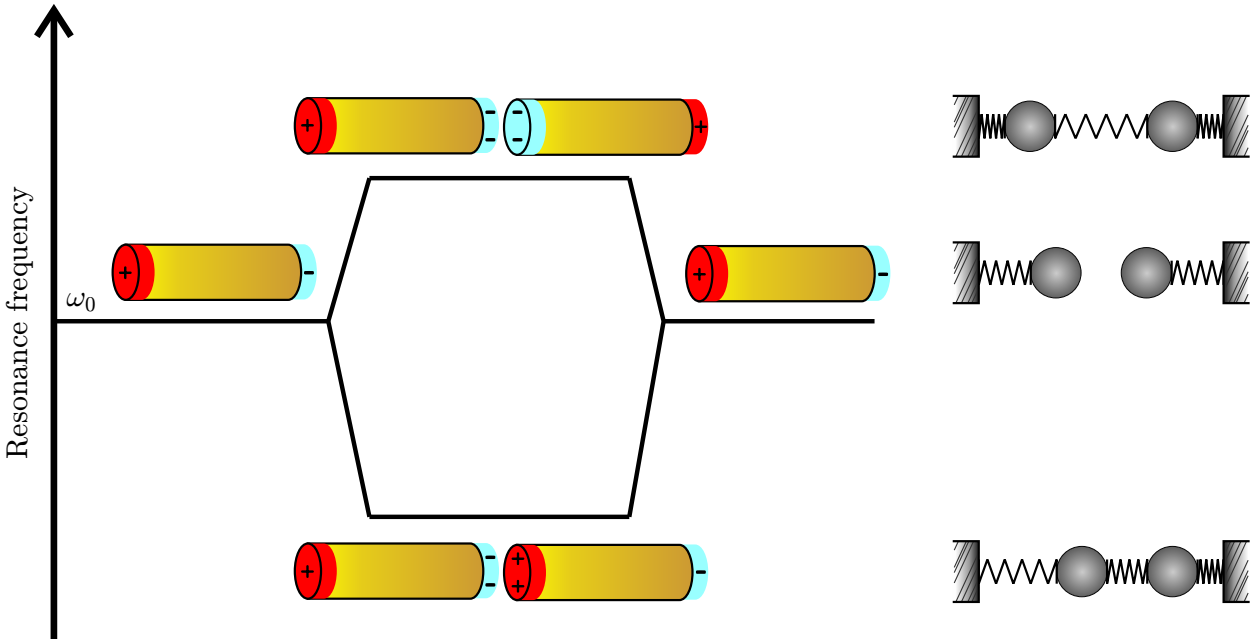

Figure 2.5: *Artistic representation of the evolution from two plasmonic nanoantennas with resonance frequency ω_0 to a gap nanoantenna and the corresponding mechanical analogue. The coupling between the two individual nanoantennas results in a mode splitting, giving rise to an in phase dipolar oscillating mode at a lower frequency and an anti phase oscillating mode at a higher frequency. Adapted from [56].*

two mass spring systems (antenna wires) through a third spring (nanoantenna gap) results in the appearance of two new eigenmodes [58]. One eigenmode exhibits an in phase oscillation of the two springs, for which the interaction spring has a fixed length and therefore does not exert any additional force on the masses. As can be seen in Figure 2.5, this eigenmode is characterized by a dipole like charge oscillation, which allows for excitation by plane wave illumination. The other eigenmode is characterized by an anti phase oscillation in which the interaction spring shifts the resonance to higher frequencies. In contrast to the first eigenmode, here, the two individual dipoles oscillate out of phase and therefore cancel each other in the far field. For a complete description a reduced restoring force of the two single particle springs has to be added to this model for the in phase eigenmode. Such a weakened spring constant can be explained by a mutual induction of charges, which in the coupled system are displaced toward the gap [57]. Thus the in phase eigenmode experiences a red-shift compared to the uncoupled system.

Numerical case study

To illustrate the previous discussion and to get an idea of possible applications of nanoantennas, numerical simulated extinction spectra and near field enhancement distributions for a nanoantenna and a gap nanoantenna are shown in Figure 2.6. For the simulations the more realistic case of a radiused nanocuboid lying on top of a glass surface was assumed instead of a cylinder in vacuum. The individual gold nanoantennas were modelled to be 180 nm long, 36 nm wide and 40 nm high. The gap of the gap nanoantenna has a width

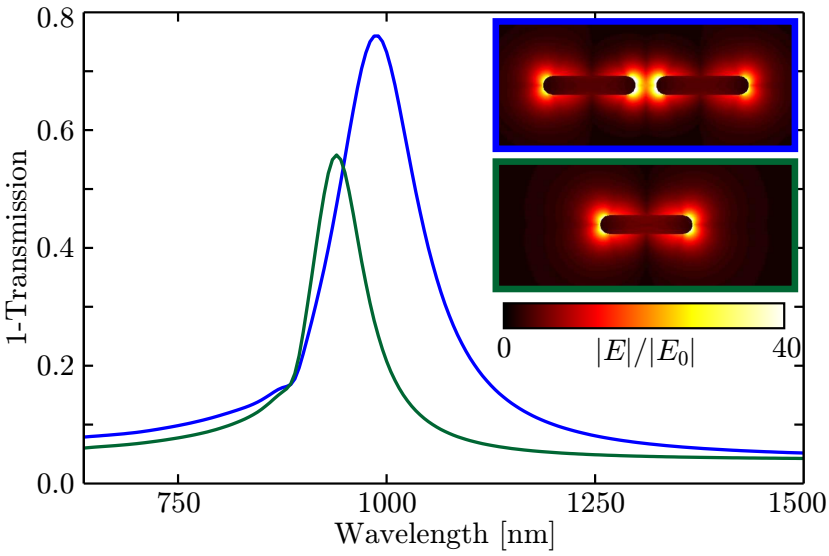

Figure 2.6: *Numerical simulated extinction (one minus transmission) spectra of a nanoantenna (green) and a gap nanoantenna (blue) arranged with the same periodicity. The inset shows the simulated near fields $|\boldsymbol{E}|$ normalized to the incident field $|\boldsymbol{E}_0|$ on an interpolated colourspace.*

of 40 nm and the nanoantennas are arranged in a lattice with a periodicity of 600 nm. The excitation was linearly polarized along the antenna arms. The coupling of the two antennas in the case of the gap nanoantenna results in a large near field enhancement which exceeds the cumulative effect of the individual wires. Additionally, the extent of the enhancement volume of the gap nanoantenna is increased compared to the nanoantenna. Thus the gap nanoantenna geometry is an interesting candidate to enhance light matter interactions in nanoscale volumes. Moreover, in the extinction spectra the previously discussed red-shift of the gap nanoantenna compared to the single nanoantenna becomes obvious. This red-shift may be obstructive, if a plasmonic nanostructure is needed which has a high aspect ratio but a resonance at short wavelengths. The comparison of the extinction spectra also reveals a broader full width at half maximum (FWHM) $\Delta\lambda$ in the case of the gap nanoantenna. This quantity is linked to the quality (Q-)factor of a resonator via the relation $Q = \frac{\lambda_0}{\Delta\lambda}$ [46]. The Q-factor itself counts the number of oscillations required for an oscillating system's energy to fall off to 0.2 % and therefore measures the energy stored in a resonator. From Figure 2.6 a decrease of the Q-factor by nearly 35 % can be extracted. All in all, the gap nanoantenna provides a better coupling between near and far field, but the single nanoantenna is obviously the better resonator.

Light matter interaction

If gap nanoantennas should be used to enhance the interaction between light and nanoscale matter via the intensity enhancement in the antenna gap, the influence of the nanoscale matter on the optical properties of the combined system, i.e., nanoantenna and nanoparticle, has to be taken into account. We have seen in paragraph 2.3.1 that an increase of the refractive index of the medium surrounding a metallic nanoparticle leads to a decrease of it's resonance frequency. Similiar results can be obtained if not a metal vacuum interface is assumed to calculate the dispersion relation of a SPP, but an arbitrary dielectric metal interface. However, for several applications it will be more obvious to place nanoscale matter,

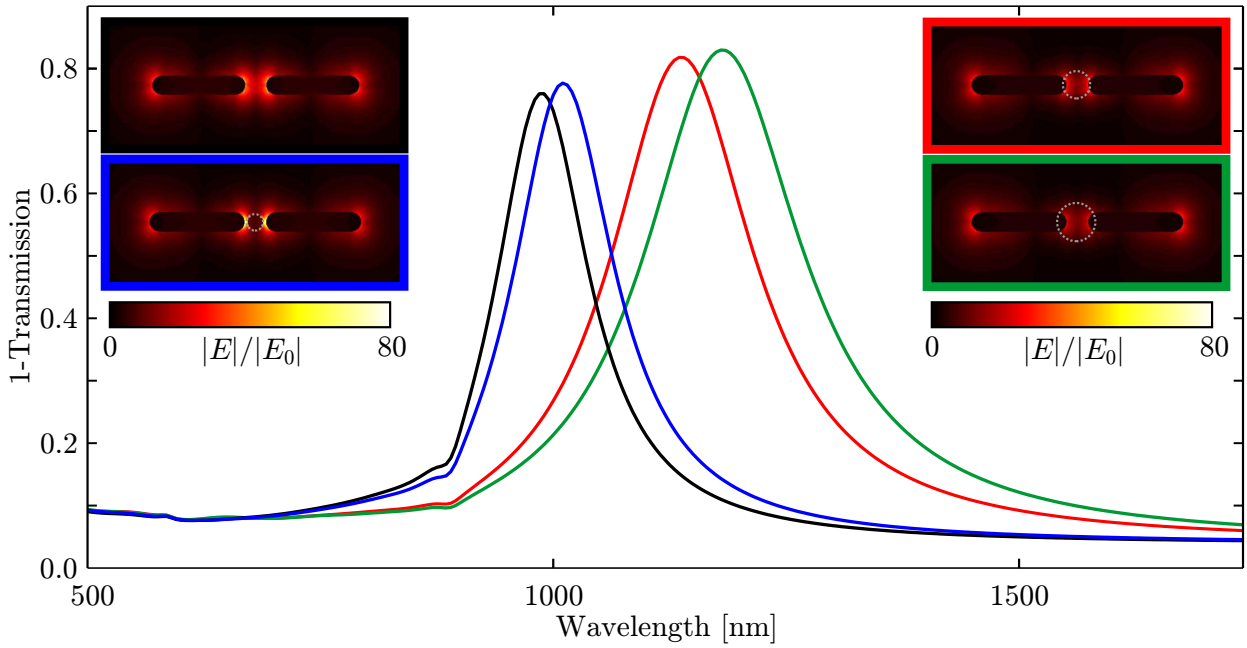

Figure 2.7: *Numerical simulated extinction (one minus transmission) spectra of gap nanoantennas for the cases, that the gap is filled with vacuum ($n = 1$) (black), a nanoparticle with a refractive index of $n = 2.2$ and a diameter smaller than the gap (blue), a nanoparticle with the same refractive index but a diameter equal to the gap (red) and a nanoparticle with the same refractive index but a diameter bigger than the gap (green). The insets show the simulated near fields $|\boldsymbol{E}|$ normalized to the incident field $|\boldsymbol{E}_0|$ on an interpolated colourspace. The perimeters of the nanoparticles are highlighted with grey dashed lines.*

e.g., nanoparticles or molecules, in the gap of the nanoantenna and not to embed it in matter. In Figure 2.7 the extinction spectra and the near field distribution of a gap nanoantenna are shown, for the cases that the gap is filled with: (black) vacuum ($n = 1$), (blue) a nanoparticle with a refractive index of $n = 2.2$ and a diameter smaller than the gap, (red) a nanoparticle with the same refractive index but a diameter equal to the gap, and (green) a nanoparticle with the same refractive index but a diameter bigger than the gap. From an examination of the extinction spectra we find, that a pronounced red-shift occurs if the nanoparticle touches the nanoantenna arms, i.e., fills the gap. Therefore a local field enhancement inside the nanoparticle can only be obtained, if the nanoparticle fills the gap completely. This becomes even more evident by an inspection of the field distributions in Figure 2.7. Here we see that for a nanoparticle smaller than the gap we get a strong field enhancement between the nanoantenna's tips and the particle but nearly no enhancement in the nanoparticle itself. However the situation drastically changes when the gap is completely filled. From this comparison we see that in order to get an enhanced light matter interaction via a gap nanoantenna the matter has to fill up the gap completely, but an only partial filling of the gap may be interesting to locally manipulate the antenna fields.

2.3.3 V-chaped nanostructures

In this paragraph we will have a look on a more complex V-chaped or L-chaped plasmonic nanostructure. At first sight this geometry can be seen as an antenna buckled in the middle. The $m = 1$ mode still exhibits a dipolar charge distribution in horizontal direction, in other words it can still interact with a horizontally polarized electromagnetic wave. Additionally this mode gives rise to a magnetic dipole moment oriented perpendicular to the plane of the V. However, the $m = 2$ mode now gives rise to a dipolar charge distribution in the vertical direction, i.e., it can interact with a vertically polarized electromagnetic wave. This occurrence of two modes at different energies and under different polarizations is also visible in a numerical estimation of the extinction shown in Figure 2.8. But the model of a buckled antenna does not involve a deviation of the change in the resonance frequencies, due to the buckling. For this purpose on can look at a V-chaped structure as two identical, perpendicular arranged, coupled antennas, where each antenna represents one arm of the V-chaped structure [59]. As in the case of the gap nanoantenna we can explain this system in the mass spring model giving rise to a set of equations of motions:

$$m\frac{\partial^2 x'(t)}{\partial t^2} + m\gamma\frac{\partial x'(t)}{\partial t} + m\omega_0^2 x'(t) + \kappa_1 y'(t) = -qE_{x'}\mathrm{e}^{-\imath\omega t} \tag{2.42}$$

$$m\frac{\partial^2 y'(t)}{\partial t^2} + m\gamma\frac{\partial y'(t)}{\partial t} + m\omega_0^2 y'(t) + \kappa_2 x'(t) = -qE_{y'}\mathrm{e}^{-\imath\omega t} \tag{2.43}$$

where κ_i represents the coupling between the two antennas and x' and y' the direction along those. For a perpendicular arrangement κ_1 equals κ_2. The solution of such a system of coupled differential equations can be found by Fourier transformation to the frequency domain and a coordinate transformation to the principal axis system, i.e., a coordinate system where both equations are decoupled [60]. In so doing we obtain the new resonance frequencies $\omega_x = \sqrt{\omega_0^2 - \kappa}$ and $\omega_y = \sqrt{\omega_0^2 + \kappa}$, as well as the principle axis system defined by the two eigenvectors $\hat{\boldsymbol{e}}_x = \frac{1}{\sqrt{2}}(\hat{\boldsymbol{e}}_{x'} - \hat{\boldsymbol{e}}_{y'})$ and $\hat{\boldsymbol{e}}_y = \frac{1}{\sqrt{2}}(\hat{\boldsymbol{e}}_{x'} + \hat{\boldsymbol{e}}_{y'})$. Hence the coordinate

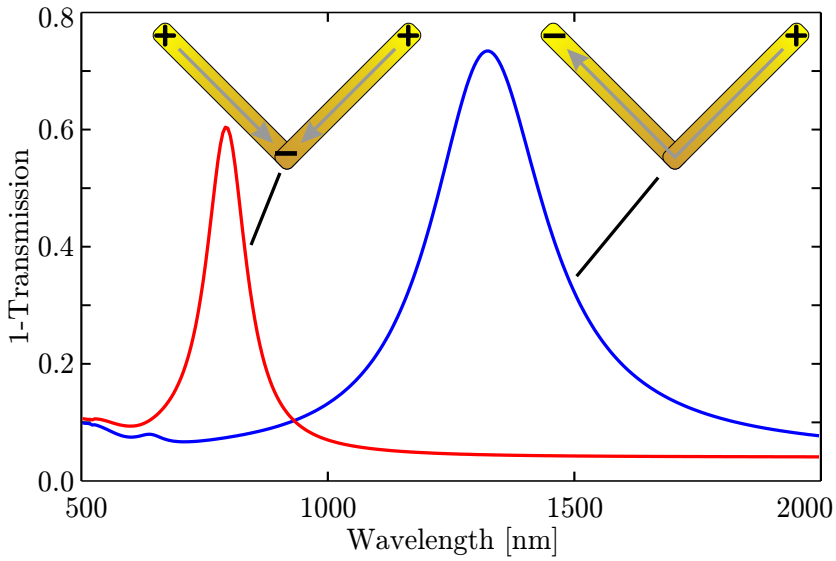

Figure 2.8: *Numerical estimated extinction (one minus transmission) spectra of a V-shaped plasmonic nanostructure for vertical polarized incident light (blue) and horizontal polarized incident light (red). The artistic representation of the nanostructures depicts the estimated charge density maxima (+ and −) and the direction of the current (grey arrows).*

system is rotated by 45° and points along the horizontal and vertical direction as discussed previously. Here, only the $m = 1$ mode of each antenna was regarded, but the coupling and splitting can be described analogously for the higher order modes.

Obviously the V-shaped nanostructures will offer some properties not encountered by nanoantennas. First, they posses two dipolar modes at distinct resonance frequencies and polarizations. Second, they posses a mode giving rise to a magnetic dipole. And last but not least they possess a lower symmetry than the nanoantennas, i.e., they do not possess a horizontal mirror plane. Especially the last point will become important in section 2.4 about nonlinear optics.

2.3.4 The metamaterial concept

In paragraph 2.2.1 we have seen, that the macroscopic response of dielectric materials can be described by the microscopic dipolar response of its building blocks, i.e., the atoms forming the dielectric. This is due to the fact, that both the size of a single atom, as well as the distance between the atoms in a crystal lattice are much smaller than the wavelength of light. This suggests itself, that by tailoring the dipolar response of the atoms the macroscopic response of materials could be tailored. We have seen in the previous paragraphs, that the optical response, especially the resonance frequency of plasmonic nanostructures can be quite easily tuned by adjusting their geometry. Thus, by arranging plasmonic nanostructures in a periodic fashion with an inter particle distance below the wavelength of light one can achieve an artificial material with a specific optical response, a so-called plasmonic metamaterial [13]. With this approach several fascinating features can be obtained like for example magnetism at optical frequencies [14–16], a negative refractive index [17–19] or electromagnetic invisible cloaks [20–22].

In this thesis the concept of plasmonic metamaterials will be used to obtain materials with a specific dispersion of the susceptibility. A straight forward approach would be to investigate isolated plasmonic nanostructures to choose a specific geometry as building block for a metamaterial. However, it has been shown that the coupling between the individual nanostructures in a metamaterial strongly influences the optical properties of the nanostructures and thereby the effective optical response of a metamaterial [61–63]. Therefore it is more reasonable to directly investigate metamaterials and to only deal with their effective response. As we have seen before, the linear interaction between an electromagnetic wave and matter can be completely described with the help of the susceptibility. In order to determine this quantity experimentally we have to turn to Lambert-Beer's law, which describes the attenuation of the intensity $I(\omega,z) = I_0 \mathrm{e}^{-\beta(\omega)z}$ of a plane wave with initial intensity I_0 when propagating in a medium [64]. With the well known relation between the electric field $\boldsymbol{E}$ and the intensity $I = \frac{c\epsilon_0}{2}|\boldsymbol{E}|^2$ [46], we see that a frequency resolved measurement of the intensity extinction provides us with the knowledge of the imaginary part of the susceptibility:

$$1 - \frac{I(\omega,z)}{I_0} \approx \beta(\omega)z = 2\frac{\omega}{c_0}\kappa(\omega)z \approx \frac{\omega}{c_0}\Im[\chi^1(\omega)]z \tag{2.44}$$

This is of course not a specific result for metamaterials, but holds true for any kind of matter. For simplicity we define the absolute extinction coefficient $\mathcal{B}(\omega) = \beta(\omega)z$. In the following

discussion we assume, that the constituting plasmonic nanostructures are all of the same kind and exhibit a single Lorentzian shaped resonance, with a resonance frequency ω_0 and the damping γ.

$$\chi(\omega) = \frac{n_a}{\epsilon_0}\frac{n_e e^2}{m_e}\frac{(\omega_0^2-\omega^2)+\imath\gamma\omega}{(\omega_0^2-\omega^2)^2+\gamma^2\omega^2} \tag{2.45}$$

Now, the resonance frequency ω_0 is not that of an isolated nanostructure, but accounts for the shifted resonance due to inter particle coupling. Likewise the damping γ describes the Ohmic and radiative losses of the particles theirselves, as well as the damping due to inter-particle coupling. The number density of the atoms n_a now describes the number density of the particles. In the following we will deal with a 2D metamaterial, i.e., plasmonic nanoparticles arranged on lattice with interparticle distances d_x and d_y. The number density times the propagation length z through the metamaterial is then just given by the interparticle distances $n_a \cdot z = 1/(d_x \cdot d_y)$. Hereby equation (2.44) and (2.45) can be rewritten to:

$$\mathcal{B}(\omega) = \frac{\omega}{c_0\epsilon_0}\frac{1}{d_x d_y}A\frac{\gamma\omega}{(\omega_0^2-\omega^2)^2+\gamma^2\omega^2} \tag{2.46}$$

$$\chi(\omega) = \frac{1}{\epsilon_0}\frac{1}{d_x d_y z}A\frac{(\omega_0^2-\omega^2)+\imath\gamma\omega}{(\omega_0^2-\omega^2)^2+\gamma^2\omega^2} \tag{2.47}$$

where $A = \frac{n_e e^2}{m_e}$ describes the individual oscillator strength. Close to the resonance, i.e., $\omega \approx \omega_0$, we can approximate this to:

$$\mathcal{B}(\omega) = \frac{1}{c_0\epsilon_0}\frac{1}{d_x d_y}A\frac{1}{\gamma} = \frac{1}{c_0\epsilon_0}\frac{1}{d_x d_y}A\frac{Q}{\omega_o} \tag{2.48}$$

$$\chi(\omega) = \frac{1}{\epsilon_0}\frac{1}{d_x d_y z}A\frac{\imath}{\gamma\omega_0} = \frac{1}{\epsilon_0}\frac{1}{d_x d_y z}A\frac{\imath Q}{\omega_0^2} \tag{2.49}$$

Thus the susceptibility of a metamaterial can be estimated by a quite simple measurement.

By using Lambert-Beer's law we assumed, that an electromagnetic wave propagating through a metamaterial only experiences absorption, but no scattering by the plasmonic nanostructures. To justify this assumption one can also connect the total extinction of a 2D metamaterial to the individual extinction cross sections of the constituting plasmonic nanostructures via their area density: $1 - T = C_{\text{ext}}/(d_x \cdot d_y)$. This approach will exactly reproduce the result obtained above, if we use the outcome of the quasi-static approximation presented in paragraph 2.3.1, that the absorption cross section dominates the extinction cross section. However, even if the quasi-static approximation is not valid for the plasmonic nanostructures constituting the metamaterial, we can at least assume for a given nanostructure geometry in a limited spectral range, that the ratio of scattering and absorption is constant.

2.4 Nonlinear optics

In the previous section we discussed linear interactions between light and matter. These interactions are linear in the sense, that the response of matter, described by the polarization, shows a linear dependence on the electric field. However, in general also nonlinear dependencies can occur, giving rise to a hole variety of effects, from which two will be used and investigated in this thesis: Second harmonic generation, which is the conversion of a wave into a new wave with twice the frequency, and optical parametric generation, which is the conversion of a wave into two new waves, whereas the sum of their frequencies corresponds to the frequency of the original wave. Due to a superlinear dependency on the amplitudes of the incident fields, those effects can only be observed in the presence of very intense optical fields, not encountered in nature. Therefore nonlinear optical effects where not perceived until the invention of the laser [23].

In this thesis second harmonic generation with plasmonic nanostructures and metamaterials will be investigated. Therefore the properties of this effect will be evaluated in this section on the basis of nonlinear light matter interaction in general. As shown in the previous section, one interesting aspect of plasmonic nanostructures is the ability to engineer their dispersion which will lead to a strongly frequency dependent nonlinear response. In order to investigate this, a tunable light source will be designed and used in this thesis, based itself on optical parametric generation, which will consequently be also discussed in this section.

2.4.1 Nonlinear polarization and effects of second order

From equation (2.8) it becomes evident, that the polarization $\boldsymbol{P}(t)$ of a medium is a function of the electric field $\boldsymbol{E}(t)$ and can thus be written as a power series of the electric field:

$$\boldsymbol{P}(t) = \underbrace{\epsilon_0 \chi^{(1)} \boldsymbol{E}}_{\boldsymbol{P}_\mathrm{L}} + \underbrace{\epsilon_0 \chi^{(2)} \boldsymbol{E}\boldsymbol{E} + \epsilon_0 \chi^{(3)} \boldsymbol{E}\boldsymbol{E}\boldsymbol{E} + ...}_{\boldsymbol{P}_\mathrm{NL}} \tag{2.50}$$

Here, the first term corresponds to the linear polarization $\boldsymbol{P}_\mathrm{L}(t)$, discussed in detail previously. The following terms, which are of higher order in $\boldsymbol{E}$ than the linear term, are summarized in the nonlinear polarization $\boldsymbol{P}_\mathrm{NL}(t)$, where the proportionality constants $\chi^{(n)}$ are the susceptibilities of n-th order. As in the linear case, the susceptibilities of anisotropic materials are in general tensors of the order $(n+1)$. For isotropic materials, or when only one tensorial component is of interest, the tensorial character can often be neglected. Putting the sum of linear and nonlinear polarization into Maxwell's equations (2.1-2.4) leads to a source term in the wave equation (2.8). Now, the nonlinear wave equation in time and frequency domain read [29]:

$$\nabla^2 \boldsymbol{E}(\boldsymbol{r},t) - \frac{\epsilon(\omega)}{c_0^2} \frac{\partial^2 \boldsymbol{E}(\boldsymbol{r},t)}{\partial t^2} = \frac{1}{\epsilon_0 c_0^2} \frac{\partial^2 \boldsymbol{P}_\mathrm{NL}(\boldsymbol{r},t)}{\partial t^2} \tag{2.51}$$

$$\nabla^2 \boldsymbol{E}(\boldsymbol{r},\omega) + \frac{\epsilon(\omega)\omega^2}{c_0^2} \boldsymbol{E}(\boldsymbol{r},\omega) = -\frac{\omega^2}{\epsilon_0 c_0^2} \boldsymbol{P}_\mathrm{NL}(\boldsymbol{r},\omega) \tag{2.52}$$

In this thesis only nonlinear processes of second order will be investigated, hence, equation (2.50) is truncated after the second summand. To derive the nonlinear processes of

second order, a scalar description will be used for the moment. In general the second order nonlinear polarization is not given by the electric field of an incoming wave squared, but by two not necessarily identical waves, which can be represented in the form:

$$E(t) = E_1 \mathrm{e}^{-\imath\omega_1 t} + E_2 \mathrm{e}^{-\imath\omega_2 t} + c.c. \tag{2.53}$$

With this approach we find that the nonlinear polarization is of the form:

$$\begin{aligned} P_{\mathrm{NL}}(t) &= \epsilon_0 \chi^{(2)} [E_1^2 \mathrm{e}^{-\imath 2\omega_1 t} + E_2^2 \mathrm{e}^{-\imath 2\omega_2 t} + 2E_1 E_2 \mathrm{e}^{-\imath(\omega_1+\omega_2)t} & (2.54)\\ &\quad +2E_1 E_2^* \mathrm{e}^{-\imath(\omega_1-\omega_2)t} + c.c.] + 2\epsilon_0 \chi^{(2)} [E_1 E_1^* + E_2 E_2^*] & (2.55) \end{aligned}$$

It is convenient to express the nonlinear polarization $P_{\mathrm{NL}}(t)$ as a sum over its different positive and negative frequency components $\sum_n P(\omega_n)\mathrm{e}^{\imath\omega_n t}$, in order to sort the complex amplitudes:

$$P(2\omega_1) = \epsilon_0 \chi^{(2)} E_1^2 \tag{2.56}$$

$$P(2\omega_2) = \epsilon_0 \chi^{(2)} E_2^2 \tag{2.57}$$

$$P(\omega_1 + \omega_2) = 2\epsilon_0 \chi^{(2)} E_1 E_2 \tag{2.58}$$

$$P(\omega_1 - \omega_2) = 2\epsilon_0 \chi^{(2)} E_1 E_2^* \tag{2.59}$$

$$P(0) = 2\epsilon_0 \chi^{(2)} (E_1 E_1^* + E_2 E_2^*) \tag{2.60}$$

Additionally there is also a response at the negative of each of the nonzero frequencies, given by the complex conjugate of the corresponding equation. Thus it becomes obvious that due to a second order nonlinearity we obtain four different frequency conversion processes, named after their resulting frequency ω:

$\omega = 2\omega_i$	second harmonic generation	(SHG)
$\omega = \omega_1 + \omega_2$	sum frequency generation	(SFG)
$\omega = \omega_1 - \omega_2$	difference frequency generation	(DFG)
$\omega = 0$	optical rectification	(OR)

Surprisingly, not all of those frequency conversion processes lead to the generation of electromagnetic radiation, but there is also one process, optical rectification, which leads to a static electric field. An intuitive picture of those processes is given in terms of the corresponding photon energy-level diagrams presented in Figure 2.9. In the case of SHG and SFG two photons are simultaneously absorbed by an atom, promoting it to a virtual, higher energy level. This virtual level decays instantaneously back to the ground level by the emission of a photon, whose frequency is the sum of the frequencies of the previously absorbed photons. Hence, SHG can be understand as degenerate SFG. In the case of DFG we see, that the absorption of a photon at the frequency ω_1 and one at ω_2, resulting in the emission of a photon at the frequency $\omega = \omega_1 - \omega_2$, would violate the conservation of energy. Thus, for every photon created at the difference frequency $\omega = \omega_1 - \omega_2$ a photon at ω_1 must be absorbed and a photon at ω_2 and ω must be emitted, giving rise to an amplification of the input-field at ω_2. Therefore, DFG is also known as optical parametric amplification. In the photon energy-level description this corresponds to the absorption of a photon at the

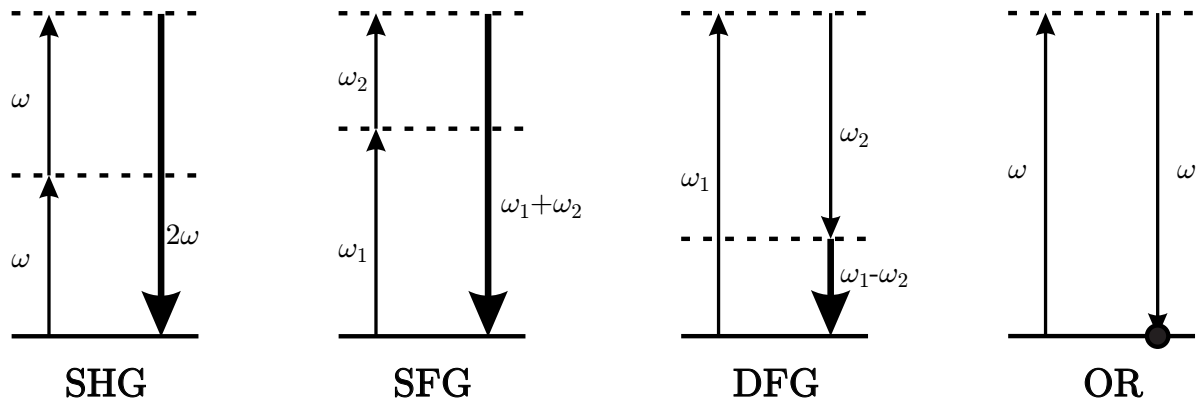

Figure 2.9: *Photon energy-level diagram of second harmonic generation (SHG), sum frequency generation (SFG), difference frequency generation (DFG), and optical rectification (OR). The solid lines represent the energy ground-level, the dashed lines virtual energy levels, the thin arrows incoming photons and the broad arrows (solid circle) the resulting photons.*

frequency ω_1, promoting the atom to a virtual, higher energy level. This virtual level decays by a two photon emission process, stimulated by the presence of the input-field oscillating at ω_2. However, this two-photon emission can also occur spontaneously, without the presence of a field at ω_2, and is known as parametric fluorescence or optical parametric generation [65].

2.4.2 Nonlinear susceptibility

In the following we will take a closer look on the second order nonlinear susceptibility. Due to the tensorial character of the susceptibility, the most general description for the nonlinear polarization of second order is given by:

$$P_i(\omega) = \epsilon_0 \sum_{jk} \sum_{nm} \chi^{(2)}_{ijk}(\omega,\omega_n,\omega_m) E_j(\omega_n) E_k(\omega_m) \tag{2.61}$$

Here the indices i,j,k refer to the Cartesian components of the fields and the convenient expression for the polarization and the electric fields is used:

$$\boldsymbol{P}_{\mathrm{NL}}(t) = \sum_n \boldsymbol{P}(\omega_n) \mathrm{e}^{-\imath\omega_n t} \tag{2.62}$$

$$\boldsymbol{E}(t) = \sum_n \boldsymbol{E}(\omega_n) \mathrm{e}^{-\imath\omega_n t} \tag{2.63}$$

As before, the summation extends over all positive and negative frequency field components. Due to the previous survey we can restrict ourselves to the case of $\omega = \omega_n + \omega_m$, which means that the nonlinear susceptibility of second order is characterized by 12 tensors, which accounts for 6 different three wave mixing possibilities, whereas additionally each frequency can be replaced by its negative [29]. Furthermore each of these 12 tensors consists of 27 Cartesian components, thus the second order nonlinear susceptibility is determined by 324 components. In the following it will be shown, that this number can be strongly reduced.

Properties of the nonlinear susceptibility

First of all the polarization as well as the electric fields represent physical measurable quantities and therefore must be real, thus the positive and negative frequency components can be related via [29]:

$$P_i(\omega) = P_i(-\omega)^* \tag{2.64}$$
$$E_j(\omega_n) = E_j(-\omega_n)^* \tag{2.65}$$
$$E_k(\omega_m) = E_k(-\omega_m)^* \tag{2.66}$$

leading to a relation for the tensor components of the form:

$$\chi^{(2)}_{ijk}(\omega,\omega_n,\omega_m) = \chi^{(2)}_{ijk}(-\omega,-\omega_n,-\omega_m)^* \tag{2.67}$$

As the order of the electric fields in equation (2.61) is arbitrary, we can conclude that:

$$\chi^{(2)}_{ijk}(\omega,\omega_n,\omega_m) = \chi^{(2)}_{ikj}(\omega,\omega_m,\omega_n) \tag{2.68}$$

This is known as intrinsic permutation symmetry. For example, for the case of SHG the nonlinear polarization is thus given by:

$$\begin{pmatrix} P_x(2\omega) \\ P_y(2\omega) \\ P_z(2\omega) \end{pmatrix} = \begin{pmatrix} \chi^{(2)}_{xxx} & \chi^{(2)}_{xyy} & \chi^{(2)}_{xzz} & \chi^{(2)}_{xyz} & \chi^{(2)}_{xxz} & \chi^{(2)}_{xxy} \\ \chi^{(2)}_{yxx} & \chi^{(2)}_{yyy} & \chi^{(2)}_{yzz} & \chi^{(2)}_{yyz} & \chi^{(2)}_{yxz} & \chi^{(2)}_{yxy} \\ \chi^{(2)}_{zxx} & \chi^{(2)}_{zyy} & \chi^{(2)}_{zzz} & \chi^{(2)}_{zyz} & \chi^{(2)}_{zxz} & \chi^{(2)}_{zxy} \end{pmatrix} \begin{pmatrix} E_x(\omega)^2 \\ E_y(\omega)^2 \\ E_z(\omega)^2 \\ 2E_y(\omega)E_z(\omega) \\ 2E_x(\omega)E_z(\omega) \\ 2E_x(\omega)E_y(\omega) \end{pmatrix} \tag{2.69}$$

However, one can always move to a coordinate system in which one of the Cartesian coordinates describes the propagation direction, thus only two Cartesian components of the fields can be observed.

A very important feature of the second order nonlinear susceptibility arises, when the symmetry of the nonlinear medium (crystal) is taken into account. In a medium owing inversion symmetry, an inversion of the Cartesian coordinates will change the sign of the field amplitudes and the polarisation, e.g., $P_i(-\boldsymbol{r}) = -P_i(\boldsymbol{r})$. For a nonlinear process of second order this leads to [46]:

$$P_i(-\boldsymbol{r}) = \epsilon_0 \chi^{(2)}_{ijk} E_j(-\boldsymbol{r}) E_k(-\boldsymbol{r}) \tag{2.70}$$
$$= \epsilon_0 \chi^{(2)}_{ijk} (-E_j(\boldsymbol{r}))(-E_k(\boldsymbol{r})) \tag{2.71}$$
$$= \epsilon_0 \chi^{(2)}_{ijk} E_j(\boldsymbol{r}) E_k(\boldsymbol{r}) \tag{2.72}$$
$$= P_i(\boldsymbol{r}) \tag{2.73}$$

This can only be fulfilled if $\chi^{(2)}_{ijk} = 0$. Therefore, nonlinear optical effects of second order, or more general of even order, can only be found in non inversion symmetric media, or to use a crystallographic language, in noncentrosymmetric media.

Let us, for example, consider a nonlinear material possessing a mirror symmetry in x-direction, i.e., a mirror plane in yz-plane, and a mirror symmetry in z-direction, but no mirror symmetry y-direction. These symmetries correspond for example to the V-shaped structures depicted in Figure 2.8. If furthermore the incident light is propagating in the z-direction, i.e., the electric field has only components in x- and y-direction, the nonlinear polarization for SHG is reduced to:

$$\begin{pmatrix} P_x(2\omega) \\ P_y(2\omega) \\ P_z(2\omega) \end{pmatrix} = \begin{pmatrix} 0 & 0 & 0 & 0 & 0 & \chi^{(2)}_{xxy} \\ \chi^{(2)}_{yxx} & \chi^{(2)}_{yyy} & \chi^{(2)}_{yzz} & 0 & 0 & 0 \\ 0 & 0 & 0 & \chi^{(2)}_{zyz} & 0 & 0 \end{pmatrix} \begin{pmatrix} E_x(\omega)^2 \\ E_y(\omega)^2 \\ 0 \\ 0 \\ 0 \\ 2E_x(\omega)E_y(\omega) \end{pmatrix} \tag{2.74}$$

Thus, one only has to deal with five tensor elements, but two are not accessible in the discussed situation.

Anharmonic oscillator model

In paragraph 2.2.1 the Lorentz model of an atom was used to describe linear response of nonmetallic matter to an incident electromagnetic wave. In the following this model will be extended by allowing a nonlinearity in the restoring force exerted on the electron. As stated above, second order nonlinear optical effects can only occur in noncentrosymmetric media. Due to the noncentrosymmetry, the equation of motion for an electron will take the following form [47, 66]:

$$\ddot{q}_i + \gamma_{\mathrm{L},i}\dot{q}_i + \omega_{0,i}^2 q_i + \sum_{jk} a_{ijk} q_j q_k = -\frac{e}{m_e} E_i(t) \tag{2.75}$$

where q_i is the displacement of the electron in the i-th direction, thus i,j,k account again for the Cartesian coordinates, and a_{ijk} describes the asymmetry of the atomic potential. The applied optical field has the same form as in equation (2.53). To solve equation (2.75) it is convenient to use a perturbative ansatz, where $E(t)$ is replaced by $\lambda E(t)$, with λ ranging between zero and one. Now, one has to deal with:

$$\ddot{q}_i + \gamma_{\mathrm{L},i}\dot{q}_i + \omega_{0,i}^2 q_i + \sum_{jk} a_{ijk} q_j q_k = -\frac{e}{m_e} \lambda E_i(t) \tag{2.76}$$

which can be solved using a power series ansatz:

$$q_i = \lambda q_i^{(1)} + \lambda^2 q_i^{(2)} + \lambda^3 q_i^{(3)} + ... \tag{2.77}$$

Insertion and sorting by powers of the expansion parameter results in the equations:

$$\ddot{q}_i^{(1)} + \gamma_{\mathrm{L},i}\dot{q}_i^{(1)} + \omega_{0,i}^2 q_i^{(1)} = -\frac{e}{m_e} E_i(t) \tag{2.78}$$

$$\ddot{q}_i^{(2)} + \gamma_{\mathrm{L},i}\dot{q}_i^{(2)} + \omega_{0,i}^2 q_i^{(2)} + \sum_{jk} a_{ijk} q_j^{(1)} q_k^{(1)} = 0 \tag{2.79}$$

$$\text{etc.} \tag{2.80}$$

The lowest order contribution $q_i^{(1)}$ is obviously governed by the same equation as the linear Lorentz model and is thus solved by:

$$q_i^{(1)}(t) = q_i^{(1)}(\omega_1)\mathrm{e}^{-\imath\omega_1 t} + q_i^{(1)}(\omega_2)\mathrm{e}^{-\imath\omega_2 t} + c.c. \tag{2.81}$$

with the amplitudes:

$$q_i^{(1)}(\omega_\alpha) = -\frac{e}{m_e}\frac{E_i(\omega_\alpha)}{D_i(\omega_\alpha)} \tag{2.82}$$

and the complex denominator $D_i(\omega_\alpha) = \omega_{0,i}^2 - \omega_\alpha^2 - \imath\omega_\alpha\gamma_{\mathrm{L},i}$. Hence, we can reproduce the linear susceptibility:

$$\chi_i^{(1)}(\omega_\alpha) = N_e\frac{e^2}{\epsilon_0 m_e}\frac{1}{D_i(\omega_\alpha)} \tag{2.83}$$

where the principal axis coordinate system was assumed, i.e., $\chi_{ij}^{(1)} = \delta_{ij}\chi_{ii}^{(1)} = \delta_{ij}\chi_i^{(1)}$. The expression for $q_i^{(1)}$ is then substituted into equation (2.79) giving rise to the frequencies $\pm 2\omega_1, \pm 2\omega_2, \pm(\omega_1+\omega_2), \pm(\omega_1-\omega_2)$, and 0. As example, the response at frequency $2\omega_1$, i.e., SHG will be determined. Hence,

$$\ddot{q}_i^{(2)} + \gamma_{\mathrm{L},i}\dot{q}_i^{(2)} + \omega_{0,i}^2 q_i^{(2)} = -\sum_{jk} a_{ijk}\left(\frac{e}{m_e}\right)^2 \frac{E_j}{D_j(\omega_1)}\frac{E_k}{D_k(\omega_1)}\mathrm{e}^{-\imath 2\omega_1 t} \tag{2.84}$$

has to be solved, which can be done with the ansatz:

$$q_i^{(2)}(t) = q_i^{(2)}(2\omega_1)\mathrm{e}^{-\imath 2\omega_1 t} + c.c. \tag{2.85}$$

leading to the result:

$$q_i^{(2)}(2\omega_1) = -\sum_{jk}\frac{a_{ijk}}{D_i(2\omega_1)}\left(\frac{e}{m_e}\right)^2 \frac{E_j}{D_j(\omega_1)}\frac{E_k}{D_k(\omega_1)} \tag{2.86}$$

In analogy with the linear case, the second order nonlinear susceptibility for SHG can now be written as:

$$\chi_{ijk}^{(2)}(2\omega_1,\omega_1,\omega_1) = \frac{a_{ijk}N_e e^3}{\epsilon_0 m_e^2 D_i(2\omega_1)D_j(\omega_1)D_k(\omega_1)} \tag{2.87}$$

Analogously the second order nonlinear susceptibilities at the other frequencies can be found.

Miller's law

A comparison of the resulting second order nonlinear susceptibility given by equation (2.87) with the linear susceptibility given by equation (2.83) shows, that the second order nonlinear susceptibility can be expressed with the help of the linear susceptibilities at the corresponding frequencies:

$$\chi^{(2)}_{ijk}(2\omega_1,\omega_1,\omega_1) = \frac{\epsilon_0^2 m_e a_{ijk}}{N_e^2 e^3}\chi^{(1)}_{ii}(2\omega_1)\chi^{(1)}_{jj}(\omega_1)\chi^{(1)}_{kk}(\omega_1) \tag{2.88}$$

An interesting consequence of this correlation is an enhancement of the second order nonlinear susceptibility in the case, that the linear susceptibility exhibits a resonance at either the driving frequency (one-photon resonance) or at the second harmonic frequency (two-photon resonance). Already in the earlier years of nonlinear optics R. Miller empirically showed that the ratio:

$$\frac{\chi^{(2)}_{ijk}(2\omega_1,\omega_1,\omega_1)}{\chi^{(1)}_{ii}(2\omega_1)\chi^{(1)}_{jj}(\omega_1)\chi^{(1)}_{kk}(\omega_1)} \tag{2.89}$$

is nearly constant for all noncentrosymmetric crystals [27]. This corresponds to the fact that the combination

$$\frac{\epsilon_0^2 m_e a_{ijk}}{N_e^2 e^3} \tag{2.90}$$

is nearly constant. The parameters e,m_e and ϵ_0 are of course fundamental constants. For all condensed matter, the electron number density N_e is also nearly the same. Thus, a_{ijk} should be the same for all condensed matter. C. Garret and F. Robinson gave the following explanation to this [28]: (i) The linear and nonlinear contributions to the restoring force will be same, if the displacement of the electrons due to a driving field becomes comparable to the size of the atom. (ii) The size of the atom is in the order of the separation between the atoms, given by the lattice constant d, thus $m_e\omega_0^2 d = m_e a d^2$. (iii) ω_0 and d are roughly the same for most solids.

2.4.3 Nonlinear response of plasmonic nanoparticles

Metallic nanoparticles can be used in at least two different ways for nonlinear frequency conversion applications. The first method is to employ the dramatic near field enhancement inherent to plasmonic nanoparticles in order to boost nonlinear processes [42, 67]. As the nonlinear polarization of second order scales quadratically with the amplitude of the driving field, an enhancement of the amplitude will also quadratically enhance the nonlinear polarization. This gives rise to the idea of placing a second order nonlinear material at a position close to a plasmonic nanostructure, where the field is enhanced in order to boost the response of the nonlinear material. Such a hybrid geometry could for example consist of a gap nanoantenna, as presented in paragraph 2.3.2, whose gap is loaded with a second order nonlinear dielectric nanostructure. But some care has to be taken with this approach. We

have seen before, that the nonlinear response is anisotropic with respect to the driving field. This indicates that the dielectric nanostructure, or to be more precise its crystallographic axis, has to be aligned with respect to the local field components and depending on the exact plasmonic geometry, only dielectrics with certain non vanishing elements of the nonlinear susceptibility can be employed [68]. Furthermore, it was shown in paragraph 2.3.2 that at least for gap nanoantennas a complete filling of the gap is necessary to obtain a significant field enhancement in the dielectric.

In the presented concept a plasmonic nanostructure was used to enhance the nonlinear response of a dielectric nanostructure, i.e., the plasmonic nanostructure acts as a passive element. But plasmonic nanostructures can also give rise to an intrinsic second order nonlinear response [42, 69]. This might sound counterintuitive as the building materials for plasmonic nanostructures, metals, show a inversion symmetric bulk atomic structure. However, on a surface inversion symmetry is obviously broken, giving rise to a second order nonlinearity, especially as plasmonic nanostructures have a high surface to volume ratio due to their overall size. In the previous section it was furthermore shown that the electric field in plasmonic nanostructures is strongly confined to their surface. Additionally, when the nonlinear response of subwavelength objects is studied, the symmetry of the object itself has also to be taken into account [70, 71]. For example the V-chaped structures described in paragraph 2.3.3 show a lower symmetry than the nanoantennas discussed in paragraph 2.3.2, which is manifested in an several orders of magnitude stronger nonlinear response of the V-chaped structures [37]. All in all, the possibility of influencing their symmetry and resonances by means of geometry design, together with their strong coupling to free space radiation, and their field enhancement abilities, have encouraged several studies on the nonlinear response of plasmonic nanostructures leading to frequency conversion efficiencies beyond those of dielectric materials [32].

In order to describe the nonlinear response of dielectrics the Lorentz model was just extended to describe an anharmonic potential of the electrons. Unfortunately such an easy extension can not be done for metallic matter, as the Drude model, describing linear response of metals, depicts the electrons as unbound. However, a description of the free electron gas as a fluid leads to nonlinear effects of arbitrary order similar to nonlinearities in hydro-dynamics [72]. In this approach not individual electrons are considered, but the free electron gas as a hole is characterized by a number density $n_e(\boldsymbol{r},t)$ and a velocity field $\boldsymbol{v}(\boldsymbol{r},t)$, which gives rise to a charge density $\rho(\boldsymbol{r},t)$ and a current density $\boldsymbol{j}(\boldsymbol{r},t)$ [33]:

$$\rho(\boldsymbol{r},t) = e\left(n_0 - n_e(\boldsymbol{r},t)\right) \tag{2.91}$$

$$\boldsymbol{j}(\boldsymbol{r},t) = \left(\rho(\boldsymbol{r},t) - en_0\right)\boldsymbol{v}(\boldsymbol{r},t) \tag{2.92}$$

Here n_0 is the time independent number density of the positively charged background formed by the ions of the metal. The time derivative of the current density $\frac{\partial}{\partial t}\boldsymbol{j}(\boldsymbol{r},t)$ representing a source term in the inhomogeneous wave equation (2.7) can then be expressed as:

$$\frac{\partial}{\partial t}\boldsymbol{j}(\boldsymbol{r},t) = -en_e\frac{\mathrm{d}\boldsymbol{v}}{\mathrm{d}t} + \sum_k \frac{\partial}{\partial r_k}\left(\frac{\boldsymbol{j}j_k}{en_o - \rho}\right) \tag{2.93}$$

where the first term on the right hand side describes a force density based on the Lorentz

force and can thus be related to:

$$-en_e\frac{\mathrm{d}\boldsymbol{v}}{\mathrm{d}t} = \frac{-e}{m_e}\left[(\rho - en_0)\,\boldsymbol{E} + \boldsymbol{j}\times\boldsymbol{B}\right] \tag{2.94}$$

Thus one finally obtains, by adding a phenomenological term $\gamma\boldsymbol{j}$ describing the losses, and replacing the charge density via $\rho = \epsilon_0\nabla\boldsymbol{E}$:

$$\frac{\partial}{\partial t}\boldsymbol{j}(\boldsymbol{r},t) = \frac{e^2 n_0}{m_e}\boldsymbol{E} - \gamma\boldsymbol{j} - \frac{e}{m_e}\left[\epsilon_0(\nabla\boldsymbol{E})\boldsymbol{E} + \boldsymbol{j}\times\boldsymbol{B}\right] + \sum_k \frac{\partial}{\partial r_k}\left(\frac{\boldsymbol{j}j_k}{en_o - \rho}\right) \tag{2.95}$$

The first two terms represent the linear oscillation of the electrons with respect to the positive charged background, whereas the other describe the nonlinear sources. The three different contributions can be accounted to different origins: (i) $(\nabla\boldsymbol{E})\boldsymbol{E}$ has only nonzero contributions on the surface of the metal. (ii) $\boldsymbol{j}\times\boldsymbol{B}$ has only nonzero contributions in the volume of the metal. (iii) $\sum_k \frac{\partial}{\partial r_k}\left(\frac{jj_k}{en_o-\rho}\right)$ has contributions from both the surface and the volume of the metal. In order to use this model for bulk metals or to describe nonlinear effects in metallic nanoparticles, it is sufficient to choose the number density $n_e(\boldsymbol{r},t)$ equal to a constant > 0 inside the metal and $n_e(\boldsymbol{r},t = 0$ outside the metal. Following this approach, also the nonlinear response from metallic nanoparticles can be numerically calculated.

2.4.4 Wave description of nonlinear optics

To understand the evolution of electromagnetic waves in a nonlinear medium we will go back to the nonlinear wave equations given by equation (2.51) and (2.52). We will again separate the electric fields and the nonlinear polarization according to their frequency components, but now also take their spatial dependence into account [46]:

$$\boldsymbol{P}_{\mathrm{NL}}(\boldsymbol{r},t) = \sum_i \left(\boldsymbol{P}_i(\boldsymbol{r})\mathrm{e}^{-\imath\omega_i t} + \boldsymbol{P}_i^*(\boldsymbol{r})\mathrm{e}^{\imath\omega_i t}\right)/2 \tag{2.96}$$

$$\boldsymbol{E}(\boldsymbol{r},t) = \sum_i \left(\boldsymbol{E}_i(\boldsymbol{r})\mathrm{e}^{-\imath\omega_i t} + \boldsymbol{E}_i^*(\boldsymbol{r})\mathrm{e}^{\imath\omega_i t}\right)/2 \tag{2.97}$$

with this the wave equation can be separated according to the different frequency components:

$$\left(\nabla^2 + \frac{\epsilon(\omega)\omega_i^2}{c_0^2}\right)\boldsymbol{E}_i(\boldsymbol{r}) = -\frac{\omega_i^2}{\epsilon_0 c_0^2}\boldsymbol{P}_i(\boldsymbol{r}) \tag{2.98}$$

Coupled wave equations

The above wave equation must hold for each frequency component and in particular for the sum frequency component at $\omega_3 = \omega_1 + \omega_2$. Thus we can propose a plane wave at frequency ω_3 propagating in z-direction as solution. All fields will therefore be represented in the form:

$$E_i(z) = A_i\mathrm{e}^{ik_i z} \quad \text{with} \quad k_i = \frac{n_i\omega_i}{c_0} \tag{2.99}$$

The amplitude of the nonlinear polarization can now be written as:

$$P_3 \mathrm{e}^{-\imath k_3 z} = 4\epsilon_0 d_{\mathrm{eff}} A_1 A_2 \mathrm{e}^{\imath(k_1+k_2-k_3)z} \tag{2.100}$$

$$P_1 \mathrm{e}^{-\imath k_1 z} = 4\epsilon_0 d_{\mathrm{eff}} A_3 A_2^* \mathrm{e}^{-\imath(k_1+k_2-k_3)z} \tag{2.101}$$

$$P_2 \mathrm{e}^{-\imath k_2 z} = 4\epsilon_0 d_{\mathrm{eff}} A_3 A_1^* \mathrm{e}^{-\imath(k_1+k_2-k_3)z} \tag{2.102}$$

where we introduced the effective nonlinear coefficient d_{eff} which can be used to simplify the relation between the nonlinear polarization and the fundamental waves and is connected to the nonlinear susceptibility via the general nonlinear coefficient $d_{ijk} = \frac{1}{2}\chi^{(2)}_{ijk}$ [73]. Plugging this into the wave equation results in:

$$\begin{aligned}\left[\frac{d^2A_3}{dz^2} + 2\imath k_3 \frac{dA_3}{dz} - k_3^2 A_3 + \frac{\epsilon(\omega_3)\omega_3^2 A_3}{c_0^2}\right] \mathrm{e}^{\imath(k_3 z - \omega_3 t)} + c.c. = \\ \frac{-4 d_{\mathrm{eff}} \omega_3^2}{c_0^2} A_1 A_2 \mathrm{e}^{\imath([k_1+k_2]z - \omega_3 t)} + c.c.\end{aligned} \tag{2.103}$$

and analogous equations for A_1 and A_2. By using the slowly varying amplitude approximation

$$\left|\frac{\partial^2 A_i}{\partial z^2}\right| \ll k \left|\frac{\partial A_i}{\partial z}\right| \tag{2.104}$$

we can finally obtain the coupled wave equations, with the wavevector mismatch $\Delta k = k_1 + k_2 - k_3$:

$$\frac{dA_3}{dz} = \frac{2\imath d_{\mathrm{eff}} \omega_3^2}{k_3 c_0^2} A_1 A_2 \mathrm{e}^{\imath \Delta k z} \tag{2.105}$$

$$\frac{dA_1}{dz} = \frac{2\imath d_{\mathrm{eff}} \omega_1^2}{k_1 c_0^2} A_3 A_2^* \mathrm{e}^{-\imath \Delta k z} \tag{2.106}$$

$$\frac{dA_2}{dz} = \frac{2\imath d_{\mathrm{eff}} \omega_2^2}{k_2 c_0^2} A_3 A_1^* \mathrm{e}^{-\imath \Delta k z} \tag{2.107}$$

With these equations all nonlinear processes of second order can be described. However, it is important to carefully consider the initial conditions. For example, if SHG in a nonlinear crystal should be described the initial conditions will read A_1,$A_2 \neq 0$, $A_3 = 0$, but if a part of the generated wave is coupled back to the medium via a cavity, the latter condition is not fulfilled.

2.4.5 Second harmonic generation

Second harmonic generation was not only the first observed nonlinear optical process [23] but can be also seen as the lowest order nonlinear optical process, as it requires only one input wave interacting with itself creating a new wave with twice the frequency. Therefore SHG has already been used in the pioneering days of nonlinear optics to study the fundamental nonlinear properties of different kinds of media [27, 28, 74, 75]. Analogously SHG from metamaterials and plasmonic nanostructures will be investigated in this thesis. For this purpose, the principles of SHG will be presented in the following. Additionally SHG will be used to present the effect of phase mismatch.

SHG in bulk material

For SHG, the generated frequency is given by $\omega_3 = \omega_1 + \omega_2 = 2\omega$ and thus $\omega_1 = \omega_2 = \omega$ and $A_1 = A_2 = A(\omega)$. Thereby the original three coupled wave equations are reduced to the first two. We will make use of the undepleted pump approximation, i.e., $A(\omega) = \text{const.}$, and the initial condition $A(2\omega,z = 0) = 0$. For the case of $\Delta k \neq 0$ the amplitude of the generated wave after the conversion in a medium of length L is obtained by integrating equation (2.105) from $z = 0$ to $z = L$. With the intensities $I_i = 2n_i\epsilon_0 c_0 |\boldsymbol{A}_i|^2$ the result reads:

$$I(2\omega) = \Gamma^2\omega^2 I^2(\omega,z = 0)L^2\text{sinc}^2\left(\frac{\Delta kL}{2}\right) \tag{2.108}$$

with $\Gamma^2 = \frac{32d_{\text{eff}}^2}{n^2(\omega)n(2\omega)\epsilon_0 c_o^2}$ accounting for material specific parameters.
This expression predicts a dramatic decrease of the conversion efficiency, if the condition of perfect phase matching, i.e., $\Delta k = 0$, is not fulfilled. Depending on the magnitude of Δk the intensity of the generated wave inside the nonlinear medium will show a oscillatory behaviour reaching its maximum after $L_{\text{coh}} = \Delta k/2$, which is called the coherence length, as can be seen in Figure 2.10. After the coherence length the generated wave and its driving polarization are out of phase leading to a back conversion from the generated field to the driving field. In order to avoid this behaviour several techniques are known. As the coherence length in dielectric materials is typically in the order of some microns, one possibility is to use nonlinear materials with much shorter lengths or even a singular spatial expansion with respect to the propagation direction, as will be discussed later on. In the following two possibilities of achieving phase matching with structured nonlinear materials will be presented.

Quasi phase matching

The idea behind quasi phase matching (QPM) is to use a material, which is structured in a way that the nonlinear coefficient changes its sign with the periodicity Λ, which is called periodic poling.[4] If Λ is chosen to be twice the coherence length, a phase jump in the coupling of the generated and the driving field will occur, due to the sign change of the nonlinear coefficient, each time the back conversion starts to take place. Thus, the generated field will grow monotonically with the propagation. A mathematical description of quasi phase matching can be obtained, by accounting for the periodic sing change of the nonlinear coefficient via a Fourier series [76]:

$$d(z) = d_{\text{eff}}\sum_{-\infty}^{\infty} G_m \mathrm{e}^{ik_m z} \quad \text{with} \quad G_m = \frac{2}{m\pi}\sin(m\pi l/\Lambda) \tag{2.109}$$

Here, $k_m = 2\pi m/\Lambda$ describes the reciprocal vectors of the resulting grating and l/Λ the duty cycle of the two orientations. The coupled wave equations will now be modified by

[4]The term periodic poling results from the fact, that such a geometry can be fabricated by inverting the spontaneous polarization of ferroelectric domains by applying a strong electric field.

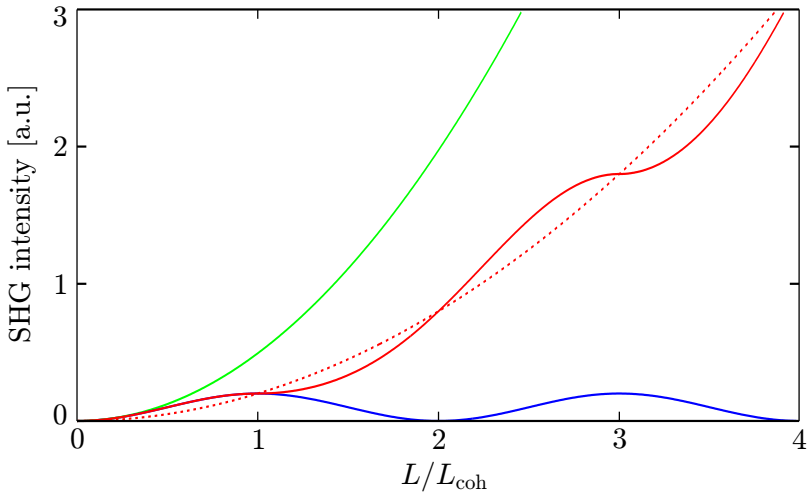

Figure 2.10: *Effect of phase matching on the growth of second harmonic intensity with distance in a nonlinear crystal. Green: perfect phase matching in a uniformly poled crystal; Blue: non phase matched interaction; Red: first order QPM by flipping the sign of the spontaneous polarization every coherence length of the interaction of the blue curve. Adapted from [76]*

the substitution $\Delta k \rightarrow \Delta k_Q = \Delta k - k_m$. It then can be shown that the highest conversion efficiency is obtained by using the term for $m = 1$ and $\Lambda = 2L_{\mathrm{coh}}$. A nice feature of quasi phase matching occurs if the temperature dependency of the refractive index is taken into account. As the coherence length is frequency dependent, perfect quasi phase matching, i.e. $\Delta k_Q = 0$, will only occur at a certain frequency (range) for a fixed periodicity. But the coherence length will change with temperature, as it depends on the refractive indices. Therefore the perfect quasi phase matching condition can be tuned to a certain frequency, by leaving the periodicity fixed and changing the temperature of the structured material.

For second harmonic generation the resulting intensity as function of the length of the nonlinear material is shown in Figure 2.10 for perfect phase matching ($\Delta k = 0$), perfect quasi phase matching ($\Delta k_Q = 0$) and imperfect phase matching ($\Delta k = 2L_{\mathrm{coh}}$). It can be clearly seen, that for $L \ll L_{\mathrm{coh}}$ the effect of phase mismatch plays a minor role, but for $L \gg L_{\mathrm{coh}}$ the generated wave can even vanish. In the case of perfect quasi phase matching the resulting conversion efficiency is still weaker than in the case of perfect phase matching but still grows quadratic with length of the employed material squared. This fact is usually accounted by a reduced effective nonlinear coefficient [76].

Random quasi phase matching

In crystalline powders or polycrystalline materials the nonlinear coefficient is not changing in a periodic fashion but rather randomly. At first sight one would expect no net conversion in this situation as the contributions of the individual domains, e.g., the particles of the powder or the crystallites of the polycrystalline material, to the average polarization should obey a uniform phase distribution and therefore interfere destructively with each other. But, by making the assumption that the individual domains obey a Gaussian size and orientation distribution, whereas the mean value of the size is given by Λ, the following results can be

obtained from the coupled wave equations [77, 78]: (i) The intensity of the wave generated by the three-wave mixing process scales linear with the number of domains N, which is correlated to the sample thickness L and the illuminated area A by $N = LA/\Lambda^3$. (ii) The intensity shows a resonance behaviour with respect to the grain size, owing its maximum when the grain size equals the coherence length. (iii) The intensity scales quadratically with the nonlinear coefficient averaged over all possible crystal orientations. (iv) The intensity of the generated wave still scales linear with the individual intensities of both driving waves.

Even if the random quasi phase matching only shows a linear scaling with the length of the employed crystal, and therefore is less efficient than perfect quasi phase matching or perfect phase matching it shows some advantages. First of all polycrystalline thin films or crystals can be fabricated quite easily as we will see later on, especially if it comes to nano or micro structured films. As the nonlinear coefficient averaged over all possible crystal orientations has to be taken into account, no care has to be taken for an alignment of the polarization of the driving fields with respect to the orientation of the employed nonlinear material. Even as random quasi phase matching shows a frequency dependence via the coherence length this dependence is rather weak compared to other phase matching techniques, thus random quasi phase matching is quite interesting for broadband frequency conversion applications [79, 80].

SHG at interfaces

In the paragraph 2.4.5 an analytic expression for SHG in bulk material was obtained by only considering equation (2.52) in the medium. In a more detailed analysis also the interface of the medium has to be taken into account. This can be done by postulating a general solution consisting of any particular solution plus a solution to the homogeneous version of (2.52) obtained by setting its right hand side to zero [29]. The continuity of the Maxwell equations require the tangential components of $\boldsymbol{E}$ and $\boldsymbol{H}$ to be continuous, which can only be fulfilled by the existence of a reflected second harmonic wave. A detailed analysis shows that the second harmonic wave inside the medium grows not from zero, but from a boundary value, i.e., a surface contribution, which is comparable to that of the bulk result for a thickness of $L = \lambda/4\pi$. For the surface contribution propagation effects, in particular phase mismatch, does not influence the amplitude of the aforementioned boundary value, which is equal to that of the reflected second harmonic wave. This essentially means, that the reflected second harmonic intensity will only show a spectral dependency with respect to the nonlinear coefficient, which can be estimated by equation (2.88). Hence, surface SHG can be employed as a reference to measure the spectral dependency of the SHG from a material of interest.

It is important to mention that the surface contribution to SHG does not only occur at the interface of noncentrosymmetric materials, but also at the interface of centrosymmetric materials. This can be understood by taking into account, that inversion symmetry is intrinsically broken at an interface. In a phenomenological treatment this process can be described by modelling the centrosymmetric medium as a thick slab consisting of a material lacking any kind of second order nonlinearity with a nonlinear polarization sheet sitting on its surface [81]. Within such a treatment it can be shown, that for a wave with frequency ω and intensity $I_{\mathrm{in}}(\omega)$ impinging perpendicular on that model geometry, the intensity of the

generated wave at frequency 2ω transmitted through the geometry is given by:

$$I_{\text{out}}(2\omega) = \eta\omega^2 \left| \boldsymbol{e}(2\omega) \cdot \boldsymbol{\chi}^{(2)}(2\omega,\omega,\omega) : \boldsymbol{e}(\omega)\boldsymbol{e}(\omega) \right|^2 I_{\text{in}}^2(\omega) \tag{2.110}$$

where η is just a proportionality constant, which can be obtained by taking the Fresnel equations into account. In the above equation the polarization of the incident wave is described by $\boldsymbol{e}(\omega)$ and the polarization of the nonlinear polarization is described by $\boldsymbol{e}(2\omega)$ hence the tensorproduct $\boldsymbol{e}(2\omega) \cdot \boldsymbol{\chi}^{(2)}(2\omega,\omega,\omega) : \boldsymbol{e}(\omega)\boldsymbol{e}(\omega)$ can be evaluated according to equation (2.69).

SHG from metamaterials

In paragraph 2.3.4 2D metamaterials were introduced and examined as plasmonic nanoparticles arranged on lattice, giving rise to an effective, collective, linear response to incident electromagnetic waves. Due to fabrication issues these metamaterials, or to be more precise metasurfaces are lying on a substrate, made for example out of glass. The building blocks of these materials, i.e., the plasmonic nanostructures, can give rise to second order nonlinear optical processes, which includes SHG. Hence, like in the linear case, we can assign an effective, collective, nonlinear response to a 2D metamaterial or metasurface. Obviously, the just described geometry resembles the model geometry of the previous paragraph about SHG at interfaces, if we restrict ourselves to a normal incident driving wave. Hence, we can make use of equation (2.110) in order to approximate the intensity of the generated second harmonic light from a metamaterial. For this purpose we first have to estimate the second order nonlinear susceptibility of a given metamaterial.

As a result of paragraph 2.4.2 Miller's law was obtained, which can be used to estimate the second order nonlinear susceptibility from the linear susceptibility. By combining this with the definition of the effective linear susceptibility of a metamaterial, given in equation (2.47), we obtain:

$$\chi_{ijk}^{(2)}(2\omega,\omega,\omega) \hat{=} \chi_{ijk}^{\text{SHG}} = \frac{a_{ijk}}{\epsilon_0} \left(\frac{1}{d_x d_y z} \right) A \frac{e}{m_e} D_{ii}(2\omega) D_{jj}(\omega) D_{kk}(\omega) \tag{2.111}$$

with the resonance function:

$$D_{ii}(\omega) = \frac{(\omega_{i,0}^2 - \omega^2) + \imath\gamma_i\omega}{(\omega_{i,0}^2 - \omega^2)^2 + \gamma_i^2\omega^2} \tag{2.112}$$

For a given metamaterial d_x and d_y are known quantities, A and D_{ii} can be obtained by measuring the absolute extinction $\mathcal{B}(\omega)$ following paragraph 2.3.4, ϵ_0, e, and m_e are natural constants, and z describes the singular thickness of a 2D metamaterial. Hence, the second order nonlinear susceptibility is completely determined except for a_{ijk}. It now appears likely, to make use of the results obtained by R. Miller and assume a_{ijk} to be constant or even to use the well-known values. But one has to keep in mind that the theoretical justification of Miller's law is based on specific properties of natural occurring crystals, which are fulfilled by all noncentrosymmetric matter but not necessarily by metamaterials.

However, for metamaterials whose source of the nonlinear polarization, i.e., the geometry of the constituting nanostructures, is similar, a_{ijk} should be a constant quantity.

From the above equations one can picture, that the unique property of metamaterials, which is the possibility to artificially tailor their linear dispersion, can be directly used to also tailor their nonlinear response. The most often encountered situation for SHG from plasmonic metamaterials is, that the driving field is in resonance with the metamaterial [37]. This is due to the fact, that the strong near-field enhancement inherent to plasmonic nanostructures is believed to be the source of their nonlinearity [42, 67, 69]. As in paragraph 2.3.4 we will now briefly approximate the second order nonlinear susceptibility for this specific case. Under the assumption $Q = \frac{\omega_0}{\gamma} \gg 1$ the resonance functions at the frequencies of interest can be approximated by:

$$D_{ii}(\omega_0) = \frac{\imath Q_i}{\omega_{0,i}^2} \tag{2.113}$$

$$D_{ii}(2\omega_0) \approxeq \frac{-1}{3\omega_{0,i}^2} \tag{2.114}$$

Hence, the generated SHG intensity under this condition will scale with 4-th power of the Q-factor, but only quadratically with the oscillator strength A and the density of the plasmonic nanostructures. However, one should keep in mind that the density of the plasmonic nanostructures can also influence the Q-factor via inter particle coupling.

The assumption was tacitly made, that $i = j = k$, or at least $\omega_{0,i} = \omega_{0,j} = \omega_{0,k}$, which is not necessarily fulfilled as seen in section 2.3. For a detailed analysis of the second order nonlinear susceptibility the wave properties, or in more detail the polarization, of the driving wave(s) and the nonlinear polarization can be taken into account. Let us assume only linear polarized transverse electromagnetic waves as driving fields and restrict ourselves to the detection of those waves for the generated field. We furthermore assume, that the nonlinear polarization sheet representing the metamaterial lies in xy-plane and excitation and detection is done perpendicular, i.e., a restriction to waves propagating in z-direction. For the case of a single wave input, we can describe the driving field as $\boldsymbol{E}(z,\omega) = E_0 \mathrm{e}^{\imath(\omega t - kz)} [\boldsymbol{e}_x \cos\theta + \boldsymbol{e}_y \sin\theta]$, with $\boldsymbol{e}_x$ and $\boldsymbol{e}_y$ being the unit vector in x- and y-direction and θ the polarization angle, i.e. the angle between $\boldsymbol{e}(\omega)$ and $\boldsymbol{e}_x$. Obviously equation (2.110) can be rewritten to:

$$I^{\mathrm{SHG}}(\omega) = \eta\omega^2 \left| \frac{\boldsymbol{P}^{\mathrm{SHG}}(\omega)}{|\boldsymbol{E}(\omega)|} \right|^2 I_{\mathrm{in}}^2(2\omega) \tag{2.115}$$

which under the previous explained condition becomes:

$$I^{\mathrm{SHG}}(\omega) = \eta\omega^2 \frac{|P_x^{\mathrm{SHG}}(\omega)|^2 + |P_y^{\mathrm{SHG}}(\omega)|^2}{|\boldsymbol{E}(\omega)|^2} I_{\mathrm{in}}^2(2\omega) \tag{2.116}$$

with:

$$\frac{|P_x^{\mathrm{SHG}}(\omega)|}{|\boldsymbol{E}(\omega)|} \hat{=} \hat{P}_x^{\mathrm{SHG}} = \left|\chi_{xxx}^{\mathrm{SHG}} \cos^2\theta + \chi_{xyy}^{\mathrm{SHG}} \sin^2\theta + \chi_{xxy}^{\mathrm{SHG}} \sin 2\theta\right| \tag{2.117}$$

$$\frac{|P_y^{\mathrm{SHG}}(\omega)|}{|\boldsymbol{E}(\omega)|} \hat{=} \hat{P}_y^{\mathrm{SHG}} = \left|\chi_{yxx}^{\mathrm{SHG}} \cos^2\theta + \chi_{yyy}^{\mathrm{SHG}} \sin^2\theta + \chi_{yxy}^{\mathrm{SHG}} \sin 2\theta\right| \tag{2.118}$$

Evaluating this for the angles $\theta = 0$, $\pi/4$, $\pi/2$ results in the following table:

θ	0	$\pi/4$	$\pi/2$
$\hat{P}_x^{\mathrm{SHG}}$	$\chi_{xxx}^{\mathrm{SHG}}$	$0{,}5\chi_{xxx}^{\mathrm{SHG}} + 0{,}5\chi_{xyy}^{\mathrm{SHG}} + \chi_{xxy}^{\mathrm{SHG}}$	$\chi_{xyy}^{\mathrm{SHG}}$
$\hat{P}_y^{\mathrm{SHG}}$	$\chi_{yxx}^{\mathrm{SHG}}$	$0{,}5\chi_{yxx}^{\mathrm{SHG}} + 0{,}5\chi_{yyy}^{\mathrm{SHG}} + \chi_{yxy}^{\mathrm{SHG}}$	$\chi_{yyy}^{\mathrm{SHG}}$

Thus, a polarization selective measurement of $I^{\mathrm{SHG}}(\omega)$ for a variation of the polarization of the driving field, can be employed to evaluate the individual tensor elements of the second order nonlinear susceptibility for second harmonic generation.

2.4.6 Optical parametric generation and amplification

Next difference frequency generation as depicted by the third diagram in Figure 2.9 will be discussed. In this process two waves at frequencies ω_1 and ω_2 interact in a nonlinear medium and generate a new output wave at $\omega = \omega_1 - \omega_2$. In order to use the general formalism obtained through equations (2.96)-(2.107) for sum frequency generation, i.e., $\omega_3 = \omega_1 + \omega_2$, the index substitution $3 \to p$, $2 \to s$ and $1 \to i$ is performed. Under the assumption that the higher energy wave is undepleted, i.e., $A_p = \text{const}$ the coupled wave equations describing the interaction can be written down:

$$\frac{dA_i}{dz} = \frac{2\imath d_{\mathrm{eff}}\omega_i^2}{k_i} A_p A_s^* \mathrm{e}^{\imath \Delta k z} \tag{2.119}$$

$$\frac{dA_s}{dz} = \frac{2\imath d_{\mathrm{eff}}\omega_s^2}{k_s} A_p A_i^* \mathrm{e}^{\imath \Delta k z} \tag{2.120}$$

For the case of perfect phase matching, these equations can be solved by differentiating the latter with respect to z and inserting the complex conjugate of the first leading to [29]:

$$\frac{d^2A_s}{dz^2} = \frac{4d_{\mathrm{eff}}^2\omega_s^2\omega_i^2}{k_s k_i c_0^4} A_p A_p^* A_s \tag{2.121}$$

and a similar equation for A_i. A general solution of such a equation has the form:

$$A_s(z) = C\sinh(\sqrt{I_p}\kappa z) + D\cosh(\sqrt{I_p}\kappa z) \tag{2.122}$$

with the integration constant C and D, depending on the boundary conditions and:

$$\kappa^2 = \frac{8d_{\mathrm{eff}}^2\omega_s^2\omega_i^2}{k_s k_i c_0^5 \epsilon_0} \tag{2.123}$$

By assuming the boundary condition $A_i(0) = 0$ and $A_s(0)$ arbitrary (or the other way around), the following result can be obtained:

$$A_s(z) = A_s(0)\cosh(\sqrt{I_p}\kappa z) \tag{2.124}$$

$$A_i(z) = \imath\sqrt{\frac{n_s\omega_i}{n_i\omega_s}}\frac{A_p}{|A_p|} A_s^*(0)\sinh(\sqrt{I_p}\kappa z) \tag{2.125}$$

With a large gain approximation, i.e., $\kappa\sqrt{I_p}L \gg 1$ where L describes the length of the employed nonlinear medium, the evolution of the intensities can be simplified to [82]:

$$I_s(L) \approx \frac{1}{4} I_s(0) \mathrm{e}^{\left(2\kappa L\sqrt{I_p}\right)} \tag{2.126}$$

$$I_i(L) \approx \frac{\omega_i}{4\omega_s} I_s(0) \mathrm{e}^{\left(2\kappa L\sqrt{I_p}\right)} \tag{2.127}$$

Now we see that the process introduced as difference frequency generation at the beginning of this chapter, does not only generate a new wave at the frequency ω_i but also amplifies the lower energy input wave at ω_s. Therefore, this process is also known as optical parametric amplification. Hence, p denotes the pump wave, s the amplified signal wave and i due to historical reasons the idler wave. Interestingly the ratio of signal and idler intensities is such that an equal number of signal and idler photons are generated, as predicted in the photon picture at the beginning of this section. Surprisingly this process even works if no input wave is explicitly present at the entrance of the nonlinear medium. In this situation which is known as optical parametric generation, both the signal and the idler wave are seeded by zero-point fluctuations [83].

In the case of amplification, the resulting frequency ω_i is determined by the input frequencies via the conservation of energy $\omega_p = \omega_s + \omega_i$, which explains the name parametric amplification. But if the process is seeded by zero-point fluctuations, which is in principle broadband noise, the resulting frequencies are not a priori determined. In this case also phase matching has to be taken into account, which parametrizes the generation up to a certain bandwidth. This bandwidth, called phase matching bandwidth can be treated, by adding a phase mismatch $\Delta k = k_p - k_s - k_i$ via the substitution $I_p\kappa^2 \rightarrow I_p\kappa^2 + (\Delta k/2)^2$ in the previous equations [82, 84]. The FWHM of the conversion efficiency curve then corresponds to a phase mismatch of $\Delta kL = 2.7831$ rad. By now varying the signal frequency, while the pump frequency is kept fixed, the phase mismatch is varied according to:

$$\frac{\partial}{\partial\omega_s}\Delta k = \frac{\partial k_s}{\partial\omega_s} - \frac{\partial k_i}{\partial\omega_i} = \frac{1}{v_{g,s}} - \frac{1}{v_{g,i}} \tag{2.128}$$

where the group velocity v_g was introduced. With this the phase matching bandwidth results in:

$$\Delta\omega = \frac{2.7831}{\left|\frac{1}{v_{g,s}} - \frac{1}{v_{g,i}}\right| L} \tag{2.129}$$

Thus optical parametric generation/amplification represents the basis of a light source whose bandwidth and central output frequency is adjustable via the phase matching condition.

There are at least three different schemes, how an OPG process can be used to provide a tunable light source [85, 86], which are depicted in Figure 2.11. The most wide spread is the use of an optical cavity, which feeds back the generated signal and/or idler light to the nonlinear crystal in order to further amplify it, as depicted in Figure 2.11(a). Depending on the cavity, the signal and/or idler light get amplified in up to several hundreds of passes through the nonlinear crystal, thus a strong net amplification can be achieved even with a

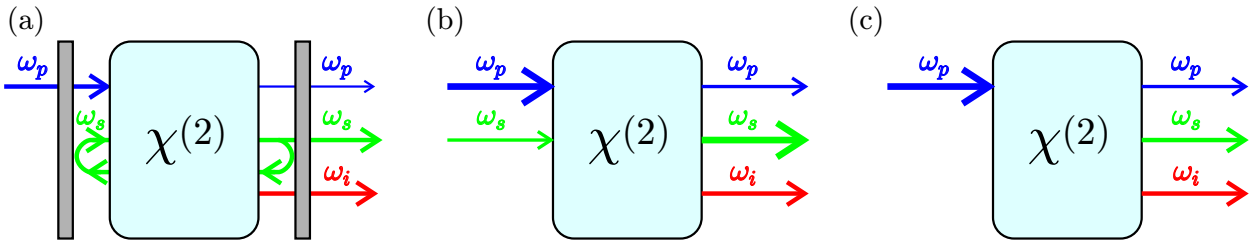

Figure 2.11: *Frequency conversion schemes based on optical parametric generation: (a) Optical parametric oscillator (OPO), (b) Optical parametric amplifier (OPA), (c) Optical parametric generator (OPG). The boxes represent a second order nonlinear crystal, whereas the grey bars represent dichroic mirrors.*

low gain per single pass through the nonlinear medium. Furthermore, the cavity can also be used to manipulate the spectral and spatial properties of the generated light. Such devices are called optical parametric oscillators (OPO). OPOs have proven their functionality and reliability in research laboratories all over the world and are nowadays a standard tool for physicists nearly as common as lasers [85, 87]. But the use of an optical cavity has also some drawbacks. An instability of the cavity will obviously influence the stability of the OPO process and depending on the needed cavity configuration, the setup of an OPO can get quite complicated, unhandy and expensive. A common alternative are optical parametric amplifiers (OPAs), as depicted in Figure 2.11(b). Here, a not too weak light source, operating at the signal frequency, is seeded in the nonlinear crystal together with a very strong pump source and gets amplified. But in such a setup the complexity of the cavity, in the case of an OPO, is just transferred to the provision of a suitable seed source. However, some research results suggest, that with a suitable pump source a high conversion efficiency can be achieved without the use of a cavity or an external seed [88, 89], as depicted in Figure 2.11(c). Such devices are known as optical parametric generators (OPG) and will be discussed in the following.

By assuming that the OPG process is initiated by zero-point fluctuations, a strongly fluctuating output, i.e., signal and idler intensities, can be expected. In contrast to this, the output stabilizes when the OPG process is driven into saturated conversion [83]. In this situation the main fraction of the pump light is converted into signal and idler light[5] and the conversion will stop, or even back conversion to the pump light can occur [90]. Thus the process will stabilize itself to a certain output power regardless of the seeding power - in a first approximation.

As the seeding power of zero-point fluctuations will be vanishingly small the OPG conversion process of the pump light to the signal or idler light will inherently be very weak, which is obviously undesirable especially if a strongly fluctuating output is not preferable. An examination of equation (2.126) and (2.127) shows, that a high gain can be achieved by the use of high pump intensities and/or long crystals. In principle, also the choice of the nonlinear material has a strong influence via the factor κ, but unfortunately the choice of nonlinear materials is rather limited, especially if periodic poling has to be taken into account [91]. The use of very long crystals might be an option, but there will be definitely

[5]Obviously the assumption of undepleted pump intensity is not valid in this situation.

a limit due to fabrication issues. So, a straight forward approach is the use of high intensity lasers as a pump source. Here the limit is of course the onset of thermal damage of the nonlinear materials, as all materials will show some kind of residual absorption. As the thermal damage scales in a first approximation with the average power, a possibility to overcome this limit is the use of a laser, which does not emit its power continuously in time, but squeezed to short intervals in time - to ultrashort pulses [92]. For example, if a laser system has an average output power of 10 W and emits, with a periodicity of 50 MHz, pulses as short as 500 fs this would result in a peak power of 400 kW, which should increase the efficiency of any nonlinear frequency conversion process tremendously while keeping the heating due to absorption on the level of a 10 W laser.

In the following some basic properties of ultrashort laser pulses will be reviewed in order to estimate how the use of those as pump source will influence an OPG. For this purpose, a secant hyperbolic pulse shape will be assumed [93]:

$$I(t) = I_0 \mathrm{sech}^2\left(\frac{1.76t}{\tau_p}\right) \tag{2.130}$$

Here τ_p is the pulse duration, accounting for the FWHM of the intensity profile. Such a pulse form is typically achieved by passive mode locking in a laser resonator. By Fourier transforming the corresponding electric field from the time domain to the frequency domain, the spectral intensity profile can be obtained [93]:

$$I(\omega) \propto \mathrm{sech}^2\left(\frac{1.76\omega}{\Delta\omega}\right) \tag{2.131}$$

Thus, a pulsed laser is not truly monochromatic but has a certain spectral width $\Delta\omega$. For secant hyperbolic shaped pulses the dependency between pulse length and bandwidth is given by the time bandwidth product (TBWP) $\Delta\omega\tau_p = 2\pi \cdot \Delta\nu\tau_p \geq 2\pi \cdot 0.315$, whereas exact equality is obtained if the pulse is Fourier limited. This term describes the condition of a frequency-independent spectral phase, i.e., all frequency components constituting the spectral intensity profile show the same phase relationship. For a given spectral width $\Delta\omega$ this condition leads to the maximum possible peak power and is hence favourable.

In equation (2.129) a phase matching bandwidth with respect to the signal and idler frequencies was defined. In a similar way an acceptance bandwidth for the pump pulse frequencies can be defined. Thus the maximum usable length of the nonlinear material is limited. However, the length is usually much more limited by a phenomena called temporal walk off, which is illustrated in the left part of Figure 2.12. Due dispersion, waves of different frequencies propagate with different velocities inside a medium, which can be taken into account via the group velocity $v_g(\omega)$. A mismatch between the group velocities of the signal and idler wave with respect to the pump wave, called group velocity mismatch (GVM), results in a temporal and spatial separation of the pulses, while propagating through the nonlinear medium. As this will obviously stop the nonlinear interaction the GVM defines a maximum interaction length $L_{\max}$, which can be approximated via [82]:

$$L_{\max} \approx \frac{\tau_{\mathrm{AC,pump}}}{\min[\mathrm{GVM}_j]} \qquad j = s,i \tag{2.132}$$

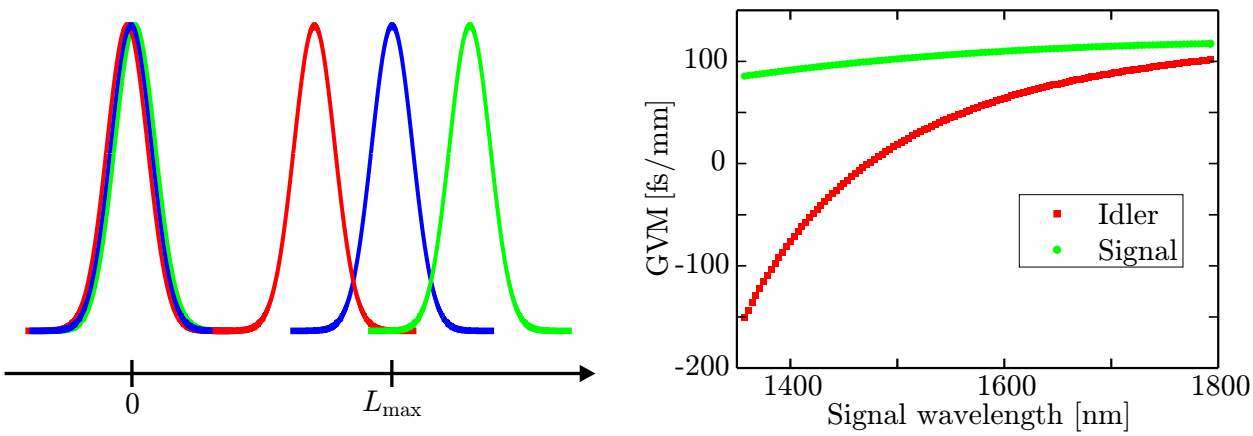

Figure 2.12: *(Left) Illustration of the temporal walk off originated in the GVM of the signal (green) and idler (red) light with respect to the pump (blue) light, for the case of* $\text{sign}[\text{GVM}_s] \neq \text{sign}[\text{GVM}_i]$ *without nonlinear trapping. (Right) Group velocity mismatch (GVM) of the signal (green) and idler (red) light with respect to the pump light, as function of the signal wavelength for* $LiNbO_3$ *pumped at 1030 nm. Data taken from [94].*

With the GVM defined via $\text{GVM}_j = v_{g,j}^{-1} - v_{g,p}^{-1}$, where j accounts for signal or idler. By inspecting the exemplary presentation of the GVM for lithium niobate ($LiNbO_3$) in the right part of Figure 2.12, two different situations can be spotted. Both the signal and the idler pulse can walk in the same direction with respect to the pump pulse, i.e. $\text{sign}[\text{GVM}_s] = \text{sign}[\text{GVM}_i]$, and they can both walk in opposite directions, i.e. $\text{sign}[\text{GVM}_s] \neq \text{sign}[\text{GVM}_i]$. In the first case the nonlinear interaction will just stop after $L_{\max}$. If we betake ourselves to the frame moving with the pump pulse, we see that, in the latter case, the signal pulse runs away from the pump pulse, but generates, due to the interaction with the pump pulse, idler light, which then runs from the signal pulse towards the pump pulse. And the other way around does the idler pulse. This leads to a localization of the generated pulses, referred to as nonlinear trapping, under the pump pulse, which strongly increases the interaction length [83, 90].

Finally the goal of an OPG pumped by ultrashort pulses should be to generate tunable ultrashort signal and idler pulses, in order to use them for an efficient spectroscopic investigation of nonlinear processes. Therefore one has to find trade-off between a high gain due to a long interaction length and a broad phase matching bandwidth due to small interaction lengths.

3

Optical parametric generator

This chapter will deal with the provision of a light source, suitable to investigate the second harmonic generation from plasmonic nanostructures and metamaterials and is closely following [95]. In the previous chapter plasmonic nanostructures and metamaterials were introduced as artificial objects, whose linear, and thereby also their nonlinear, spectral response to electromagnetic radiation, e.g., visible or near-infrared light, can be tailored. Thus it is advisable to investigate second harmonic generation from those spectrally resolved, therefore a tunable light source is needed.

As the length of plasmonic nanostructures and metamaterials, which enters the SHG efficiency quadratically, will be vanishingly small one has to employ highest possible pump intensities, to obtain a measurable nonlinear signal. But high average intensities would lead to a melting after a short period of time, due to strong absorption in resonance. To reduce the heat exposure it is possible to utilize laser pulses, which exhibit high intensities only for a period of time in the range of several femtoseconds. If a time averaged detection is used for the nonlinear signal, a pulsed excitation will result in a low signal-to-noise ratio. A usual procedure to maximize the signal-to-noise ratio is to perform the excitation with a high pulse repetition rate.

Following paragraph 2.4.6, the process of optical parametric generation and amplification should be capable to achieve spectral tunable, ultrashort pulses. So far, the research activities carried out on OPGs are mainly focused on picosecond pulse durations and/or kilohertz repetition rates [96–102]. The reason for this is that OPGs need a high parametric gain, in order to achieve a measurable output and to suppress intensity fluctuations [83, 88, 89, 102]. The high parametric gain is usually achieved by the use of an amplified laser system as a pump source or rather long nonlinear crystals. However, long crystals are usually no option for the generation of femtosecond pulses as discussed in paragraph 2.4.6.

The development of high average power passively mode-locked solid state and fiber lasers [103–105] allowed for the realization of single pass optical parametric generators based on rather short $LiNbO_3$ and $LiTaO_3$ crystals with repetition rates of several tens of megahertz and pulse durations in the femtosecond regime [88, 89]. In these experiments the average signal power and the conversion efficiency for long term operation was limited due to the onset of laser damage inside the crystal after a few minutes.

One method which is known from the picosecond regime to increase the parametric gain without using higher pump powers is to send the residual pump and the generated light through the crystal a second time [100, 106, 107]. This doubles the effective crystal length, but allows for tighter focusing compared to a longer crystal. Furthermore, such a double-pass configuration allows for a simple compensation of the temporal walk off [100]. In the following, a compact single crystal double-pass optical parametric generator configuration, based on periodically poled MgO:$LiNbO_3$, operating at 42 MHz repetition rate, tunable in the near-infrared, will be presented.

3.1 Experimental setup

The scheme of the double-pass OPG is shown in Figure 3.1. The OPG is pumped by a solitary mode-locked Yb:KGW oscillator[1][104], delivering up to 8 W average power with a pulse duration of 550 fs at a repetition rate of 42 MHz and a center wavelength of $\lambda_p = 1031$ nm. A half-wave plate and a Faraday isolator are used together as a variable attenuator for the pump beam. In order to achieve the optimal focusing condition derived by Boyd et al. [108] the pump beam was focused to a diameter of 40 µm with a f = 200 mm lens (L_1). A dichroic mirror (DCM: Reflection band 920-1160 nm, transmission band 1240-1600 nm) reflects the pump beam into the MgO:LiNbO3 crystal.[2] The crystal is 10 mm long and 0.5 mm thick, consists of 5% MgO-doped congruent $LiNbO_3$ and has 9 different poling channels (poling periods: Λ = 27.9-31.6 µm) with respect to the z-axis for quasi phase matching. The end

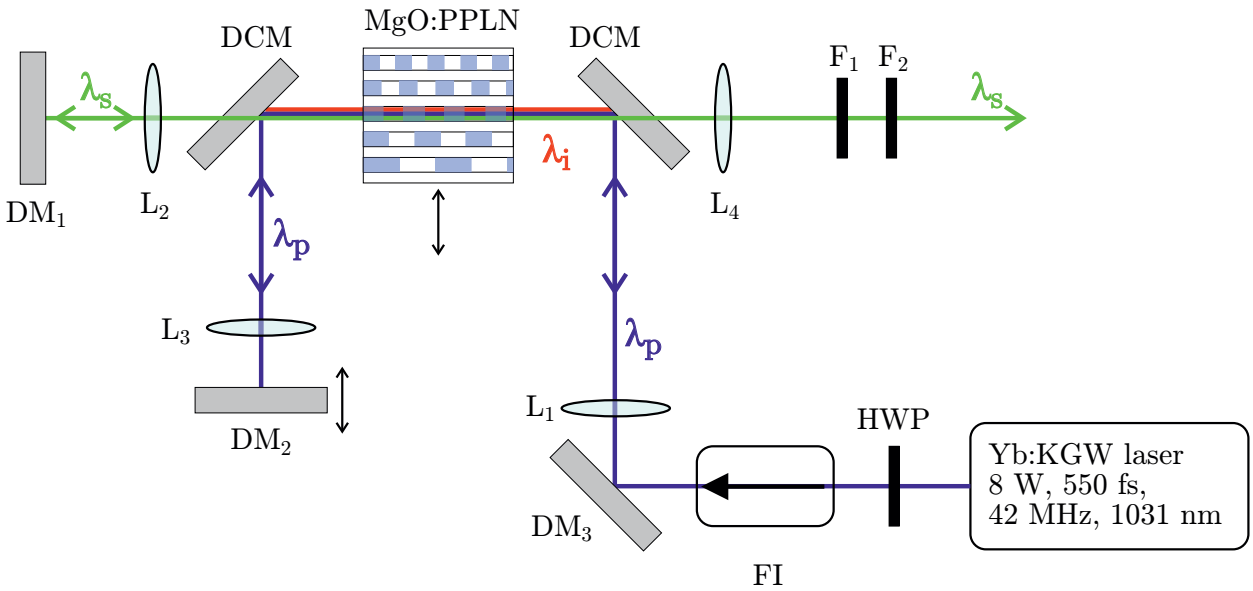

Figure 3.1: *OPG scheme: HWP: half-wave plate, FI: Faraday isolator, DM: dielectric mirror, L: lens, DCM: dichroic mirror, F: filter. The MgO:PPLN crystal can be translated with respect to the nine different poling channels. The back reflecting mirror DM_2 is mounted on a translation stage to synchronize the pump and signal pulse in the second pass.*

[1] Yb:KGW 1040-8, NT&C, Germany
[2] MOPO1-0.5-10, Covesion Ltd., United Kingdom

facets are broadband anti reflection coated (R<5%, 1000-5000 nm). The crystal is mounted on an aluminum heat sink whose temperature is controllable from 30 °C up to 200 °C. The crystal holder can be translated with respect to the different poling channels using a computer controlled stage. After passing through the crystal the transmitted pump and generated signal beam are separated by a second dichroic mirror (DCM).

For the second pass the signal beam is collimated by a lens (L_2, f = 100 mm), back reflected by a dielectric mirror (DM_1: Reflection band 1300-1900 nm) and focused back into the crystal. The transmitted pump beam is collimated by a lens (L_3, f = 150 mm), back reflected by a dielectric mirror (DM_2: Reflection band 750-1100 nm) and focused back into the crystal. The dielectric mirror (DM_2) can be translated parallel to the pump beam to ensure the temporal overlap of the signal and pump beam in the second pass.

After the second pass the signal beam passes the first dichroic mirror, is collected by a lens (L_4, f = 100 mm) and sent through two filters[3,4] in order to suppress any parasitic generated visible light and residual pump light. As all optics are made from BK-7 glass the idler light will be absorbed.

The OPG itself (without the pump laser) has a footprint of only 30 cm × 30 cm. For operation and wavelength tuning only the crystal's position and temperature, the position of DM_2 and the input power has to be varied, which can in principle all be done automated. For the use in this thesis, the control of the crystal's position and temperature was automated.

To characterize the pulse length τ_p an intensity autocorrelator as depicted in Figure 3.2 is employed. Here, a beam splitter creates two copies of the incoming pulses. These copies are superimposed in a nonlinear medium, where they interact on the basis of SHG and SFG. By introducing a spatial delay in one of the interferometer arms both copies interact time delayed in the nonlinear medium. The resulting nonlinear signal as function of the delay time τ is then proportional to the intensity autocorrelation function:

$$G_I(\tau) = \int I(t)I(t-\tau)dt \tag{3.1}$$

The FWHM of the autocorrelation trace τ_{AC} is then connected to the pulse duration via $\tau_{AC} = 1.55\tau_p$, in the case of a secant hyperbolic shaped pulse.

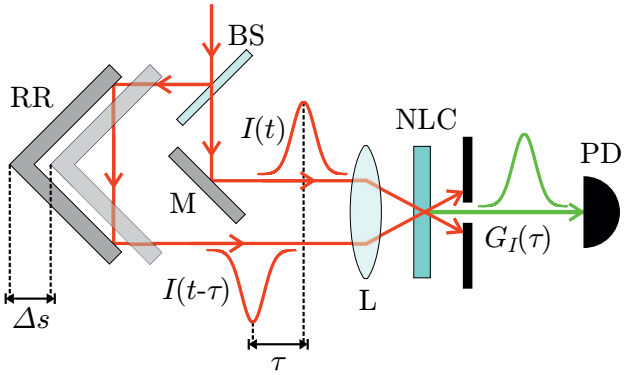

Figure 3.2: *BS: beamsplitter; RR: retroreflektor; M: mirror; L: lens; NLC: nonlinear crystal, PD: photodiode. A BS creates two copies of the incoming pulse, which are delayed in time against each other via a spatial delay of the RR and afterwards focused into a NLC. The created SHG signal gives the intensity autocorrelation as function of the delay time τ.*

[3]Schott RG-1000, Edmund Optics GmbH, Germany
[4]OD 4.0 1100 nm High Performance Longpass Filter, Edmund Optics GmbH, Germany

3.2 Results and discussion

In this section the results of the characterization of the previously presented OPG setup will be shown and discussed. In the first part the influence of the pump power on the conversion efficiency and the signal output noise will be investigated for a fixed signal wavelength. In the second part the spectral tunability and the resulting pulse shapes as well as the signal power will be analysed and discussed.

3.2.1 Pump power influence

In Figure 3.3 the signal power and the conversion efficiency are shown as a function of the incident pump power for the double-pass OPG. If not otherwise mentioned, it will be always referred to average powers and pump-to-signal conversion efficiencies. These measurements were done for a poling period of 27.9 µm at a temperature of 30 °C, which leads to a signal wavelength of $\lambda_s = 1372$ nm. The signal power was measured using a thermal power meter[5] and corrected for filter losses. The maximum achieved signal power was 2.5 W at 4.6 W incident pump power, which corresponds to a conversion efficiency of nearly 55%. By using the Manley-Rowe relations or assuming energy conservation, the generated idler radiation can be calculated [109], corresponding to a photon conversion efficiency of 72%. Saturation of the conversion efficiency seems to be reached at 4 W input power. Figure 3.3 suggests that there is no optical parametric generation below 1.5 W input power, but with the help of a LN_2-cooled InGaAs-CCD coupled to a monochromator,[6] parametric fluorescence at pump powers below 100 µW could be recorded. For all data points shown the delay between the

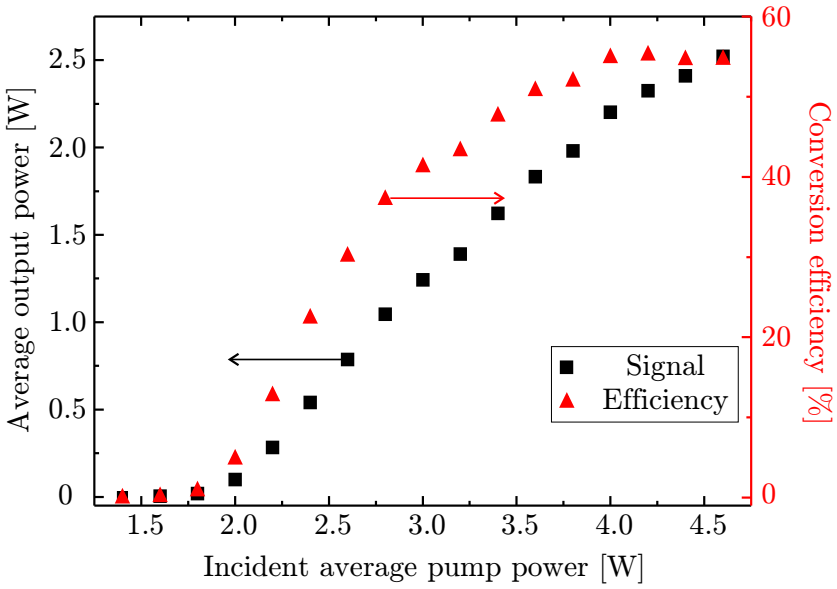

Figure 3.3: *Average output power of the signal (left axis, black squares) and pump-to-signal conversion efficiency (right axis, red triangles) versus incident average pump power.*

[5]Thermopile sensor PM10 attached to power meter FieldMate, Coherent LaserSystems GmbH, Germany
[6]PyloN-IR attached to Acton SP 2300i, Princton Instruments, USA

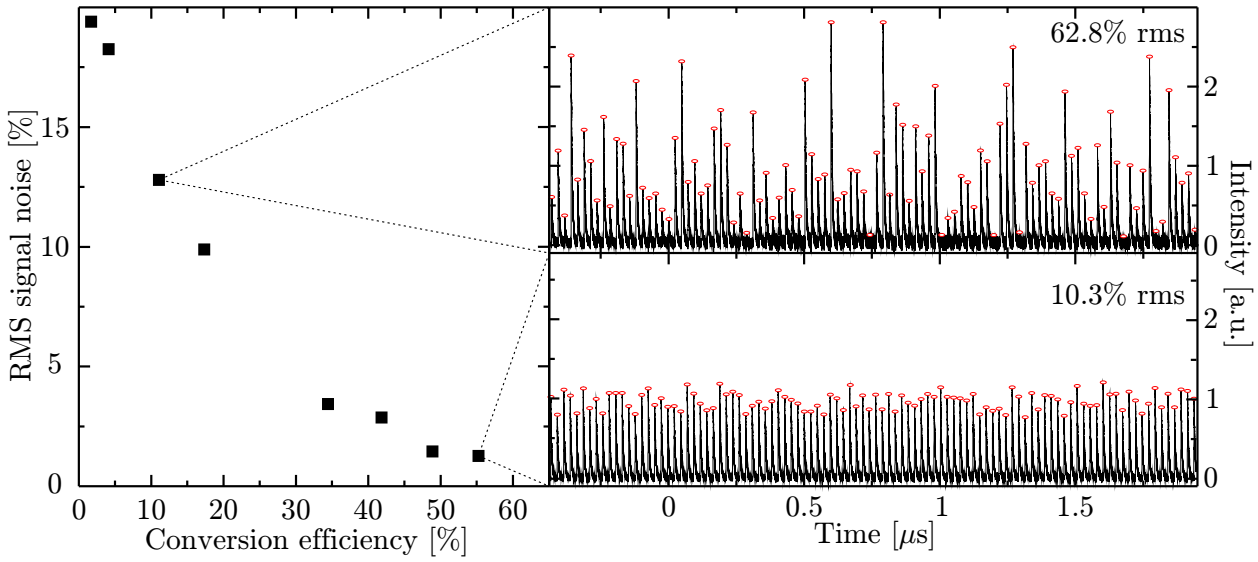

Figure 3.4: *(Left) Power fluctuations of the signal output for different conversion efficiencies. Each measurement point corresponds to a 15 minute measurement. (Right) Pulse-to-pulse fluctuations of the OPG at 10% conversion efficiency (upper) and 55% conversion efficiency (lower).*

pump and signal pulses in the second pass was optimized for maximum signal power by translating DM_2 (see Figure 3.1).

To measure the noise characteristics of the OPG, the signal power fluctuations for different conversion efficiencies, employing the 27.9 µm poling period, were evaluated. Each individual measurement was carried out over 15 minutes and for high conversion efficiencies the results were double-checked by an one hour measurement. In addition the pulse-to-pulse fluctuation of the OPG signal in the case of low and high conversion efficiency were recorded. The noise measurements of the OPG are shown in Figure 3.4. As expected, a high noise level in the case of low conversion efficiency and a drastic decay down to 1.4% rms (long term) respectively 10.3% rms pulse-to-pulse with increasing conversion efficiency can be observed. In addition long time measurement (one hour) of the spectral stability of the OPG were performed, which showed a fluctuation of the center wavelength of only 97 pm and a fluctuation of the spectral FWHM of 71 pm.

3.2.2 Wavelength tuning

Signal spectra and output power for the different poling periods between 27.9 µm and 30.5 µm, measured at 30 °C and 4 W input power are depicted in the upper part of Figure 3.5 and the corresponding intensity autocorrelations in the lower part. The input power was restricted to 4 W to stay well below the damage threshold of the longer poling periods, which should be significantly lower than that of the shorter ones [88]. The spectral positions are in reasonable agreement with numerical values achieved for perfect quasi phase matching, taking into account the temperature dependent Sellmeier equations [110] and assuming that the temperature inside the crystal should be somewhat higher than on the surface. The broadening of the spectra originates from an increase in the phase matching bandwidth for higher signal wavelengths. Also over one watt signal power were measured for the 31 µm poling period. The central wavelength should be approximately 1750 nm, but accurate spectra can not be presented as the responsivity of the used spectrometer[6] strongly decreases at around 1650 nm. This fact might also disturb the measurement of the spectrum for the 30.5 µm poling period.

The autocorrelations of the signal pulses can be fitted well assuming a secant hyperbolic pulse shape for poling periods up to 29.5 µm. With increasing poling period/signal wavelength a broadening of the side wings appears, which is especially visible for the 30 µm and 30.5 µm poling period. The pulse duration decreases monotonically from 345 fs down to 190 fs with increasing signal wavelength, assuming a secant hyperbolic pulse shape. The pulses created with the 30.5 µm poling period have an even smaller FWHM, but this value is obviously not a good figure of merit in the case of such strongly distorted pulses. The time bandwidth product for all poling periods except 30.5 µm is in the range of 0.44-0.53, which is close to the Fourier limit for a secant hyperbolic pulse. As can be seen in the upper part of Figure 3.5, the signal power is maximal at around 1380 nm signal wavelength and decreases for larger signal wavelengths.

The distortion of the pulse shape and the decrease of the conversion efficiency can be both attributed to effects originated in the GVM between the pump, signal and idler pulses discussed in paragraph 2.4.6. Up to 1450 nm signal wavelength the GVM of the signal and the idler pulses with respect to the pump pulse have different signs and furthermore the same absolute value at around 1380 nm signal wavelength, as can be seen in Figure 2.12. This leads to a trapping of the generated signal and idler pulses under the pump pulse. As a consequence the signal pulses are nearly transform limited and the length on which conversion takes place is increased. With increasing signal wavelength this trapping effect vanishes and therefore the conversion efficiency decreases and the signal pulses get distorted. This effect was minimized by optimizing the delay between the pump and signal pulses in the second pass to achieve the shortest possible pulse widths and smooth autocorrelations. A subsequent compression of the pulses with the help of a SF-10 prism sequence was also tested, but this approach gave no satisfying results. This additionally suggests, that the deviation from the Fourier limit is due to the nonlinear pulse interaction and not due to dispersion in the employed optics. Of course, more elaborate compression techniques might be used.

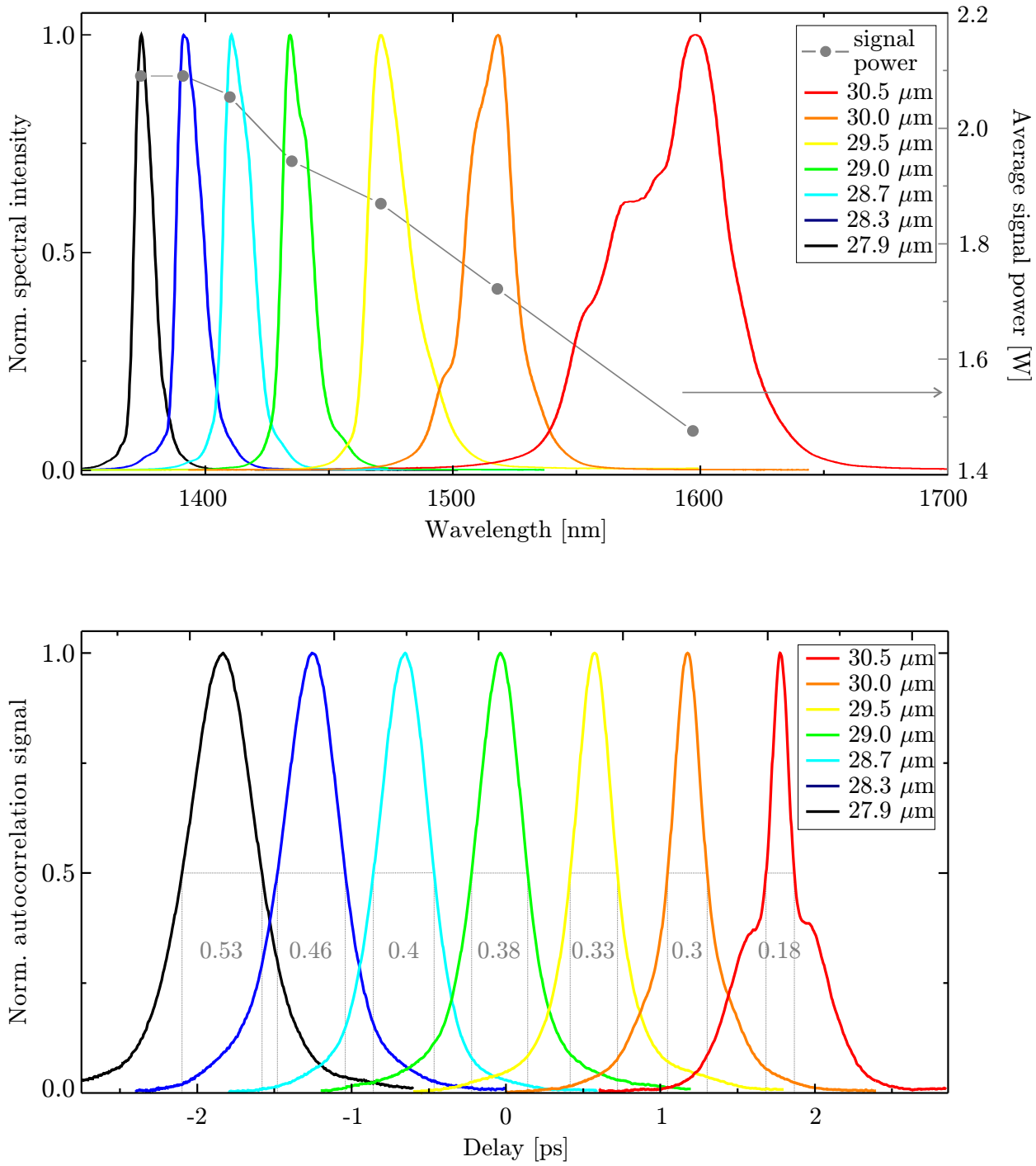

Figure 3.5: *(Upper) Measured normalized signal spectra for different poling periods. The grey dots show the measured average signal power, the grey line is a guide to the eye. (Lower) Intensity autocorrelations for different poling periods with FWHM values in ps (grey numbers). All measurements were taken at 30 °C and an average input power of 4 W.*

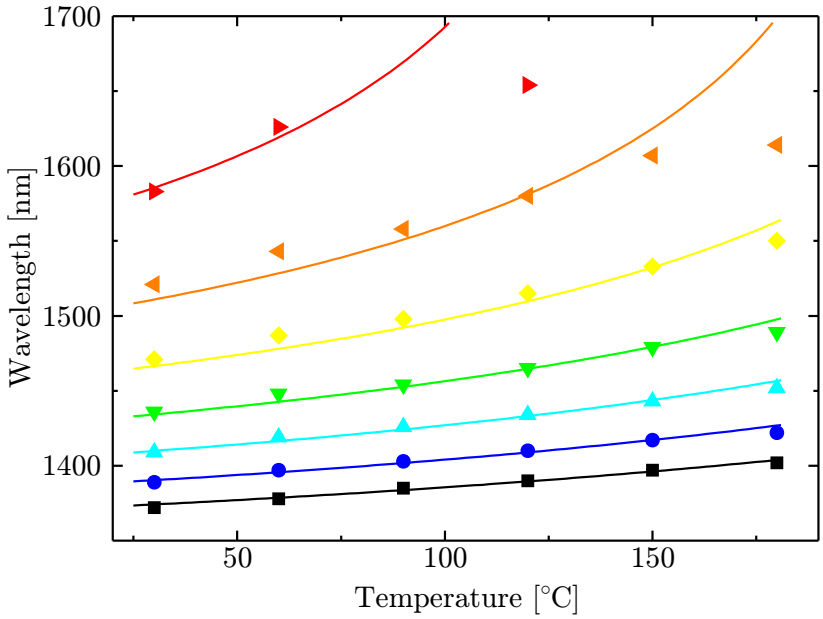

Figure 3.6: *Maxima of the measured signal spectra as function of the temperature of the heat sink for the poling periods of 27.9 µm (■), 28.3 µm (●), 28.7 µm (▲), 29.0 µm (▼), 29.5 µm (♦), 30.0 µm (◀), and 30.5 µm (▶). The continuous lines, coloured with respect to the poling periods, depict numerical values archived with [94].*

Additionally to the discrete tuning of the signal wavelength by a variation of the poling period, a continuous tuning is achieved by changing the crystal temperature as discussed in paragraph 2.4.5. The maxima of the measured signal spectra for the different poling periods are depicted in Figure 3.6 as function of the temperature. The temperature was measured/adjusted in the heat sink, on which the crystal is mounted, a few millimeters below the crystal. The symbols depict the actual measurement values, whereas the continuous lines are numerical values achieved with with the help of [94], based on the temperature dependent Sellmeier equations [110]. For lower temperatures the numerical values and the actual measurements are in good agreement. For higher temperatures ($> 170°C$) the measured signal wavelength is consistently lower than the expected value. This discrepancy most likely results from an insufficient thermal contact between the heat sink and the crystal. In the case of the longest poling periods (30.0 µm and 30.5 µm), this discrepancy is more pronounced and becomes also evident at lower temperatures. For longer poling periods the perfect quasi phase matching condition shows a stronger temperature dependency, as can be seen in the numerically achieved curves. Thus deviations between the actual and the assumed temperature of the crystal will become more pronounced. Additionally, it is not possible to measure accurate spectra at wavelengths above 1600 nm with the used equipment as discussed before.

4

Nonlinear Plasmonics

In this chapter the nonlinear response of plasmonic nanostructures and metamaterials will be investigated by means of linear spectroscopy and second harmonic generation spectroscopy. In the first section the methods used in this thesis to fabricate plasmonic nanostructures and metamaterials will be introduced. In the second section the experiments carried out on hybrid plasmonic/dielectric nanostructures will be presented and the corresponding results will be discussed. The last section will deal with second harmonic generation from two-photon resonant metamaterials, i.e., metamaterials composed of nanostructures which only show a plasmonic resonance for the generated second harmonic field, but not for the driving field.

4.1 Sample fabrication

In this section the methods used to fabricate plasmonic nanostructures and metamaterials will be discussed. In the first paragraph the principle fabrication scheme based on electron-beam lithography will be presented step by step, whereas the second paragraph focusses on thin film deposition by thermal evaporation which is used for the material deposition involved in the fabrication process.

4.1.1 Electron-beam lithography

In Figure 4.1 the essential fabrication steps of a double-stage electron-beam lithography process are shown. As electron-beam lithography cannot provide levitating nanostructures, the first step (indicated in (a)) is the provision of a substrate, suitable for both, the further experiments and the fabrication process. For the optical experiments the substrate has to be transparent in the visible and near-infrared spectral range and a low refractive index is desirable. As the goal is the fabrication of structures with submicron dimensions the substrate has obviously to be as smooth and clean as possible. For the fabrication process the substrate has to be chemically inert to organic solvents and resistant to heat treatments. These properties can be fulfilled by borosilicate glass. However electron-beam lithography also requires a conducting substrate or at least a conducting layer on top of it to avoid

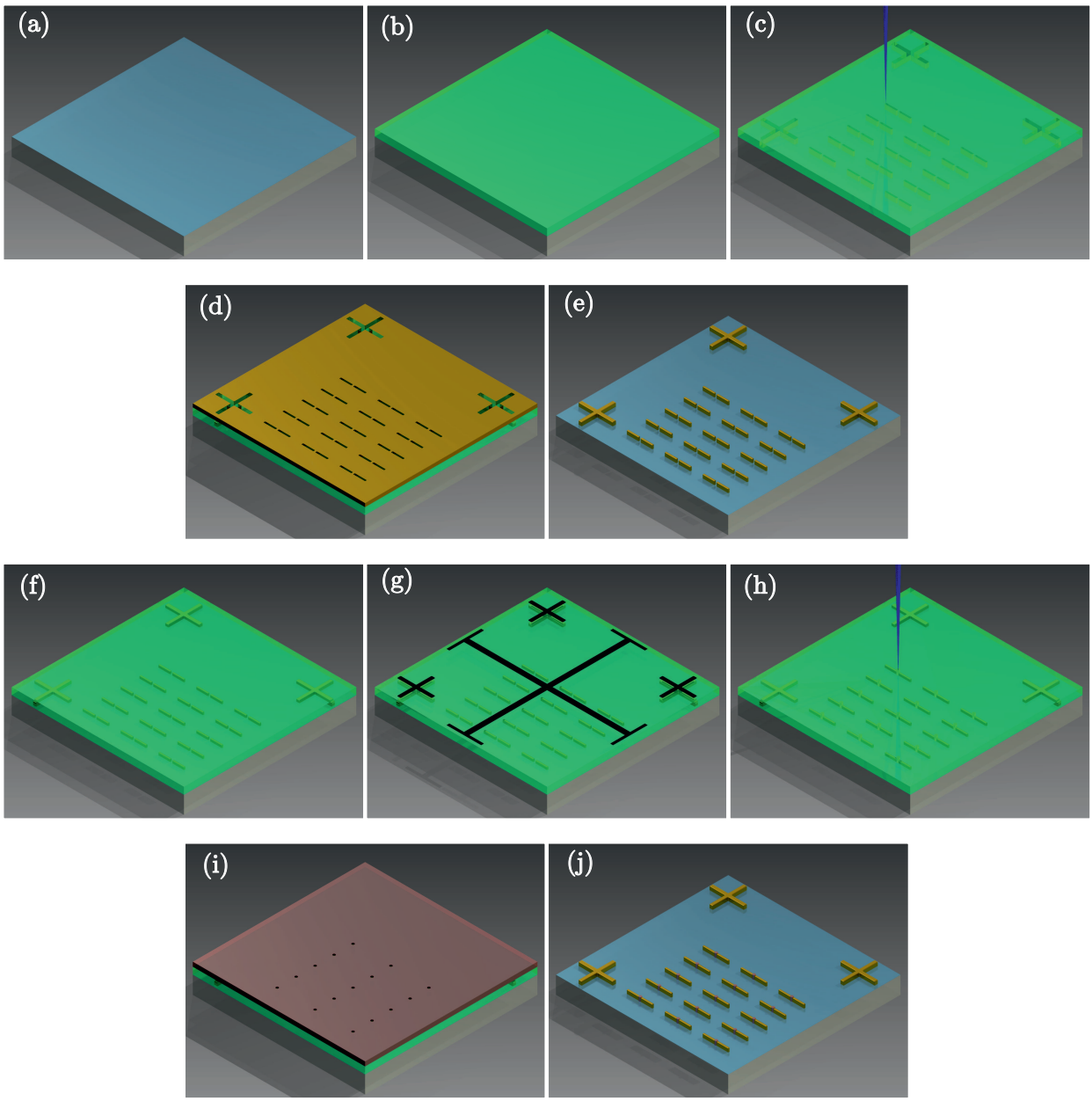

Figure 4.1: *Artists representation of a double-stage electron beam lithography process: (a) Starting with the provision of a borosilicate glass substrate (greyish transparent) covered with 10 nm ITO (blue), (b) followed by spin coating of PMMA (green) and (c) electron beam (deep blue) exposure with subsequent development resulting in a negative mask. (d) A 40 nm thin gold film is then evaporated on top and afterwards (e) a lift-off process is performed to remove the remaining PMMA with the surplus gold on top of it. (f) Next, the sample is again spin coated with PMMA. (g) Prior to the second electron exposure (h) the markers fabricated together with nanostructures in the first run are located to read in the local coordinate system of the first exposure, which allows a precise second exposure (h) relative to the first one. (i) After the development of the second exposure a 60 nm thin dielectric film is evaporated on top and afterwards (e) a lift-off process is performed analogously to the first step.*

charge accumulation. In order to obtain a large amount of substrates with identical properties a permanent, 10 nm thin indium tin oxide (ITO) layer is deposited via electron beam evaporation (see paragraph 4.1.2) on a complete 4 inch wafer of borosilicate glass,[1] which is subsequently cut into pieces with a size of 10 mm × 10 mm. ITO is one of the few materials which is transparent in the optical and near-infrared range, but has a high DC-conductivity. After the cutting, the substrate(s) is cleaned via mechanically polishing and a more than one hour ultrasonic bath with acetone and isopropyl alcohol subsequently and finally thoroughly blown dry with clean nitrogen.

Directly afterwards the electron beam resist is applied to the substrate by spin coating (indicated in (b)). As electron beam resist PMMA with a molecular weight of 950 k diluted to 4 % in anisole, is used.[2] The spin coating is done in the following steps: (i) The substrate is rotated at 500 rpm for 5 s in order to dispense 50 µl of the PMMA/anisole solution over the substrate, (ii) and then rotated at 4000 rpm for 90 s in order to obtain an approximately 200 nm thick film. (iii) At last the substrate is baked for 45 minutes at 175 °C in a convection oven to remove the residual solvent and to smooth the PMMA film.

The substrate is then transferred to a scanning electron microscope[3] (SEM) equipped with a fast electrostatic beam blanker and an external scan control and pattern generator.[4] This system allows for a controlled selective exposure (see (c)) of the PMMA film, defining the cross sections of the desired structures. For the exposure an acceleration voltage of 20 kV, an aperture size of 10 µm and a working distance of 8 mm, resulting in a current of 40 pA, was used. Due to the electron bombardment the molecular chains of the PMMA get reduced to smaller chains, which are less resistive to organic solvents. Thus, after the exposure, the PMMA is developed by swivelling the substrate for 45 seconds in a 8 °C cold, 1:3 methyl isobutyl ketone to isopropyl alcohol mixture with 1.5 vol-% butanone, resulting in the negative PMMA mask depicted in (c). The development is stopped by blowing dry the substrate with clean nitrogen.

On top of the negative mask a 40 nm thin gold film (depicted in (d)) is thermally evaporated (see paragraph 4.1.2). Afterwards a lift-off process is performed, in which the hole substrate is soaked in 60 °C hot N-methyl-2-pyrrolidone in order to dissolve the remaining PMMA. After 3 hours the softened PMMA and the surplus gold on top of it are washed away, by carefully spraying the substrate with N-methyl-2-pyrrolidone. In order to obtain clean samples and nanostructures, as depicted in (e), the substrate is afterwards rinsed in acetone, isopropyl alcohol and distilled water, baked for 45 minutes at 175 °C in a convection oven, and finally exposed for 1 hour to an Ar/O_2-plasma.

If only gold nanostructures are desired the sample is now finished. For several purposes the combination of nanostructures consisting of different materials is needed, for example the combination of plasmonic nanostructures with dielectrics. To fabricate those a second electron-beam lithography run is applied to the previously fabricated sample. The sample is again spin coated with PMMA (depicted in (f)), but this time with a double layer. The first layer consists of 600 k PMMA spun with 4000 rpm and the second layer consists of 950 k

[1] Supplied by Plan Optik AG, Germany
[2] Supplied by micro resist technology GmbH, Germany
[3] Type Sigma, Carl Zeiss Microscopy GmbH, Germany
[4] Type ELPHY Plus, Raith GmbH, Germany

PMMA spun at 6000 rpm. Between the two spin coating steps, an intermediate baking is performed for 10 minutes on a hot plate at 175 °C. The lower, thicker layer, consisting of PMMA with a lower molecular weight is more sensitive to electron exposure, than the upper, thinner layer. Thus an electron exposure and subsequent development results in a PMMA cross section profile with a deep undercut, which makes the lift-off easier in the case of structures with a bigger height. Prior to the second exposure, the exact coordinate system of the first exposure has to be retrieved. For this purpose, not only the desired nanostructures were fabricated in the first electron-beam lithography run, but also three cross like markers around the nanostructure arrays. By selectively scanning those makers, the coordinate system of the first exposure can be determined (see (g)). Thus the cross sections of the second set of nanostructures can be exposed with a high precision relative to the nanostructures fabricated in the first run (see (h)). For the scanning of the markers and the subsequent exposure an acceleration voltage of 30 kV, an aperture size of 15 µm and a working distance of 13 mm is used, resulting in a current of 130 pA. These parameters, different from those used in the first exposure, are used, as the PMMA appears more transparent at 30 kV and the higher current provides a better contrast, thus the makers can be read in more precisely. After the second exposure the sample is developed analogously to the first exposure. This time a 60 nm thin dielectric film is thermally evaporated on the obtained hole mask (see (i)). Last but not least the same lift-off procedure as before is performed, resulting in the hybrid metallic/dielectric nanostructures depicted in (j). However, the baking and plasma cleaning are left out, as these might damage the dielectric nanostructures.

The artists representation of the above explained process in Figure 4.1 might suggest, that only a single array of nanostructures per substrate is fabricated. In reality both, the fabrication of the metallic nanostructure geometries and the relative positioning of the dielectric nanostructures is not as reproducible as desired. Therefore several arrays are fabricated on a single substrate, with variations of both parameters form array to array. The maximum deflection of the electron beam limits the area, which can be exposed to 100 µm × 100 µm. Therefore the retrieval of the original coordinate system has to be done for each array of nanostructures individually, which is a quite time consuming and wearing process. Hence, an automatization of this step was implemented in the process. By this the number of nanostructure arrays per substrate is only limited by the substrate size resulting in maximum number of areas per substrate of roughly 600.

4.1.2 Thin film deposition by thermal evaporation

In the previous paragraph the deposition of thin films consisting of three different inorganic materials was mentioned: gold, ITO, and not yet specified dielectrics. While there are several possible methods for thin film deposition, in this thesis thermal evaporation under high vacuum is solely used and will be shortly reviewed in the following. A schematic sketch of an evaporation plant is shown in Figure 4.2(a). In the evaporation process the starting material (target material) is heated slightly above its boiling or sublimation point in a high vacuum chamber.[5] This leads to the liberation of atoms, atomic clusters or molecules, i.e., evaporation, from the target material. These will then travel undirected away from

[5]Typical pressures are below 10^{-6} mbar.

the hot target material due to thermal diffusion, until they hit a cold surface where they condensate and form a film [111]. The reason to perform the heating under vacuum is, that the evaporated material would react with residual gas particles otherwise leading to a contamination of the fabricated film and furthermore, the lower pressure leads to a lower boiling or sublimation point. In a typical geometry the substrate is mounted several tens of centimeters above the target material with the surface to coat pointing towards the target material. If the evaporation is undirected, a bigger distance between the target material and the substrate leads to a lower rate of evaporated material hitting the substrate, whereas a smaller distance leads to an increased heat up of the substrate. The thickness of the evaporated thin film and the evaporation rate is measured in situ with a quartz microbalance and the knowledge of the target material's volumetric mass density.

The heating of the target material is, in this thesis, done via: (i) Ohmic or resistive heating, i.e. the target material is placed on a metal foil, formed like a boat (depicted in Figure 4.2(b)), which is heated by the passage of a high current through itself. As materials for the metal foils tungsten, tantalum or molybdenum are usually used due to their high melting point. The electrodes connected to the metal foil are usually cooled, in order to only heat up the metal foil. (ii) Electron beam heating, i.e., a high energy electron beam is guided and focussed on the target material. The electrons transfer their kinetic energy due to inelastic scattering to the target material and thus heat it up. The target material is usually placed in a water cooled crucible, which leads to a selective heating of the material at the position of the electron impact.

Both methods have several advantages and disadvantages. First of all the equipment needed for Ohmic heating is less complicated than that for electron beam heating. But in the case of Ohmic heating the target material gets heated mainly at the contact points to the

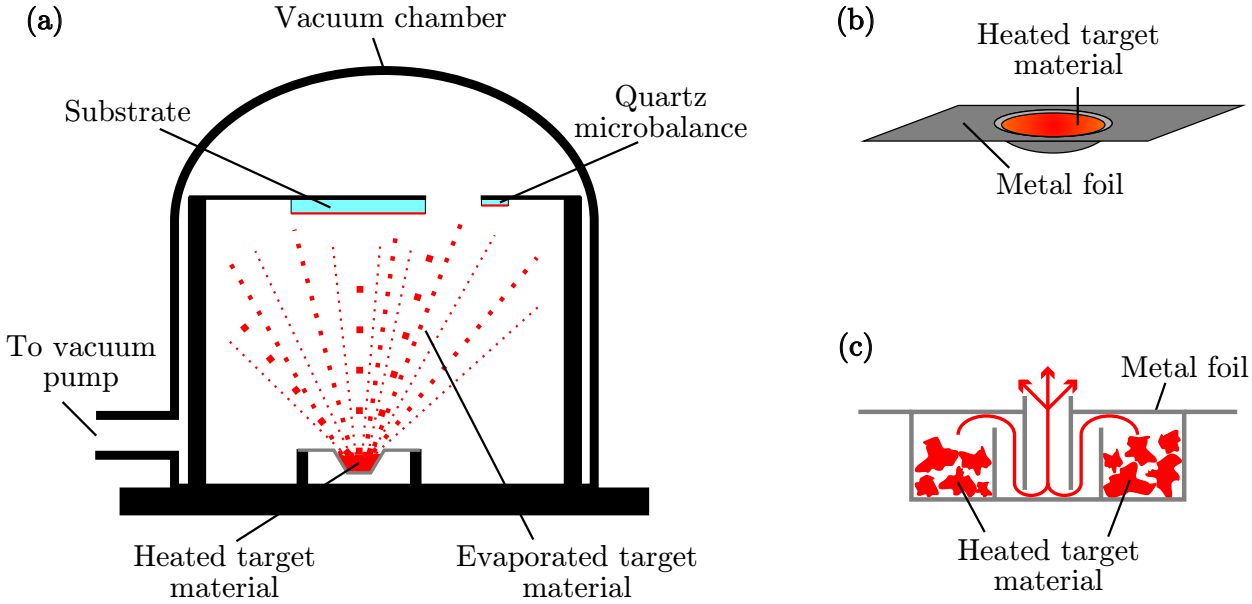

Figure 4.2: *(a) Schematic sketch of a vacuum chamber used for thin film deposition via thermal evaporation. (b) Sketch a boat-type evaporation source. (c) Cross section of a baffled box evaporation source.*

metal foil, which are not pointing towards the substrate, and only partially by radiative heating. This results in a not uniformly heated target material and in a slow response to a change of the temperature of the metal foil. Thus the evaporation rate, which is determined by the temperature, is quite complicated to control. These problems can be overcome by using only materials, whose melting point is below their sublimation or boiling point, at the pressure were the deposition is performed. The target material will then melt before evaporation sets in and thus forming a good thermal contact. Unfortunately there are only a few materials, which fulfil this criteria under high vacuum conditions, but one of them is gold. Alternatively to boat like metal foils, box like heaters can be used, which represent a kind of thermal radiation cavity where the target material can be placed in. There are also quite elaborate forms of these boxes (see Figure 4.2(c)), where the evaporated material is redirected through several baffles, leading to an uniform thermal distribution [112]. And finally only those materials can be evaporated, whose sublimation point is reasonably below that of the metal foil.

Electron beam evaporation does not show all these disadvantages, and as the evaporation rate is governed by the energy of the electron beam it allows also for a very fine tuning of the rate. However, some tests suggest, that a part of the electrons hitting the target material are reflected by it towards the substrate. If the substrate is coated with PMMA, as in the case of electron beam lithography, the PMMA will get modified by the electron bombardment hindering a lift-off process [113]. Thus electron beam evaporation is used to deposit the ITO, as an accurate rate control will be needed to fabricate a uniform 10 nm thin film on a complete wafer, but for gold and the dielectrics Ohmic heating is the method of choice.

During evaporation the target material decomposes into atoms, atomic clusters or molecules (in the following called particles), which condensate again when they hit the cold substrate. Thus the resulting film will be polycrystalline or amorphous. If we think of multielement materials this may also lead to non stoichiometric films. It was stated that the particles directly condensate or to be more precise stick to the surface of the substrate when they hit it. But in detail, a particle hitting the surface can still move over the surface for a finite time or even reevaporate. This time is proportional to the substrate temperature and the kinetic

Material	Evaporation source	Evaporation rate	Substrate temperature during evaporation	Annealing
Au	Tungsten boat	0.2 nm/s	ambient	175°C for 45 min
ITO	Electron beam	0.1 nm/s	ambient	400°C for 4 h
LaF_3	Tantalum baffled box	1 nm/s	ambient	non
ZnS	Tantalum baffled box	5 nm/s	100°C	non

Table 4.1: Materials deposited via thermal evaporation and the corresponding process parameters.

energy of the incoming particle [114]. If this time is sufficiently long for another particle to collide with it these particle can interact and form a compound. Hence, a higher substrate temperature and evaporation rate will in general lead to a more crystalline film [115]. In some cases the evaporated films can be also improved by a heat treatment following the evaporation. For example in the case of gold, the melting point will strongly decrease with decreasing particle size, thus a heat treatment can lead to a smoothing of the evaporated films [116]. In the case of oxides, evaporated films usually show a lack of oxide. This can be also overcome by just annealing those films under normal air, as they will oxidise [117]. Indeed, it is even possible to obtain thin metal oxide films by evaporating thin metal films and a subsequent oxidation procedure [118].

Finally, the appropriate parameters for the film deposition via thermal evaporation have to be determined empirically and matched to the demands on the films to fabricate and the available equipment. The relevant parameters for the deposition used in this thesis are given in the following Table 4.1.

4.2 Hybrid plasmonic/dielectric gap nanoantennas

In several experiments on second harmonic generation [35, 119, 120] and third harmonic generation [38, 39] from hybrid plasmonic/dielectric nanostructures an enhancement of the nonlinear efficiency of the hybrid dielectric/plasmonic nanoantennas compared to that of the corresponding bare nonlinear dielectric nanocrystals was observed. These findings apparently support the idea, that the nonlinear signal of a dielectric particle with a large nonlinear susceptibility can be increased by employing the local field enhancement inherent to plasmonic nanostructures. However, a recent experimental study on third harmonic generation from gap nanoantennas containing ITO nanoparticles casts serious doubts on this interpretation [39]. A strong indication was found that the nonlinear enhancement of the investigated hybrid plasmonic/dielectric nanoantennas is mainly related to changes in the linear optical properties of the gap nanoantenna resonances due to the presence of the ITO nanoparticles and not to the third order nonlinearity of the nanoparticles.

In this section, which is closely following [121], the origin of the second harmonic generation from hybrid plasmonic/dielectric gap nanoantennas will be studied. For this purpose, gap nanoantennas made of gold are combined either with nonlinear zinc sulphide (ZnS) nanoparticles or linear (in this context linear means that the second order nonlinear susceptibility vanishes due to symmetry reasons) lanthanum fluoride (LaF_3) nanoparticles. Additionally, the combination of two plasmonic gap nanoantennas will be studied, where one gap nanoantenna is resonant for the pump field while the second gap nanoantenna is resonant for the generated second harmonic light.

4.2.1 Investigated samples

In Figure 4.3 SEM micrographs of the investigated (a) bare gold gap nanoantennas, (b) gap nanoantennas with ZnS nanoparticles, (c) gap nanoantennas with LaF_3 nanoparticles, (d) ZnS nanostructures, and (e) double resonant gap nanoantenna systems with ZnS nanoparticles are shown. The preparation of all nanostructures is done by a double-stage electron-beam lithography process (see section 4.1). For the experiments a gap nanoantenna design was chosen, which is known to exhibit only a weak intrinsic SHG efficiency [122–124]. The gap nanoantennas have a width and a height of 40 nm, a gap width of 50 nm, and are arranged on a 900 nm × 600 nm lattice with a size of 40 µm × 40 µm. Several arrays with different antenna arm lengths were fabricated, whereas the arm length was varied around 300 nm. Out of these, the antennas in Figure 4.3 were chosen such, that the linear extinction has a maximum at around 1500 nm wavelength. In order to compensate the red-shift associated with the incorporation of a dielectric in the nanoantenna's gap (see paragraph 2.3.2), hybrid gap nanoantennas were chosen for comparison, which are approximately ten percent shorter than the bare gold gap nanoantennas. Additionally dielectric nanoparticles arranged on a 900 nm × 600 nm lattice without antennas but with a comparable size to those located in the nanoantenna gaps, and 60 nm thin dielectric films were fabricated in the second lithography stage. For one sample (sample 1) ZnS, which is a wide band gap noncentrosymmetric semiconductor, was used as dielectric, whereas for a second sample (sample 2) LaF_3, which has a comparable refractive index to ZnS but a centrosymmetric crystal structure, was used instead. The SEM micrographs indicate that the ZnS is in a crystalline state.

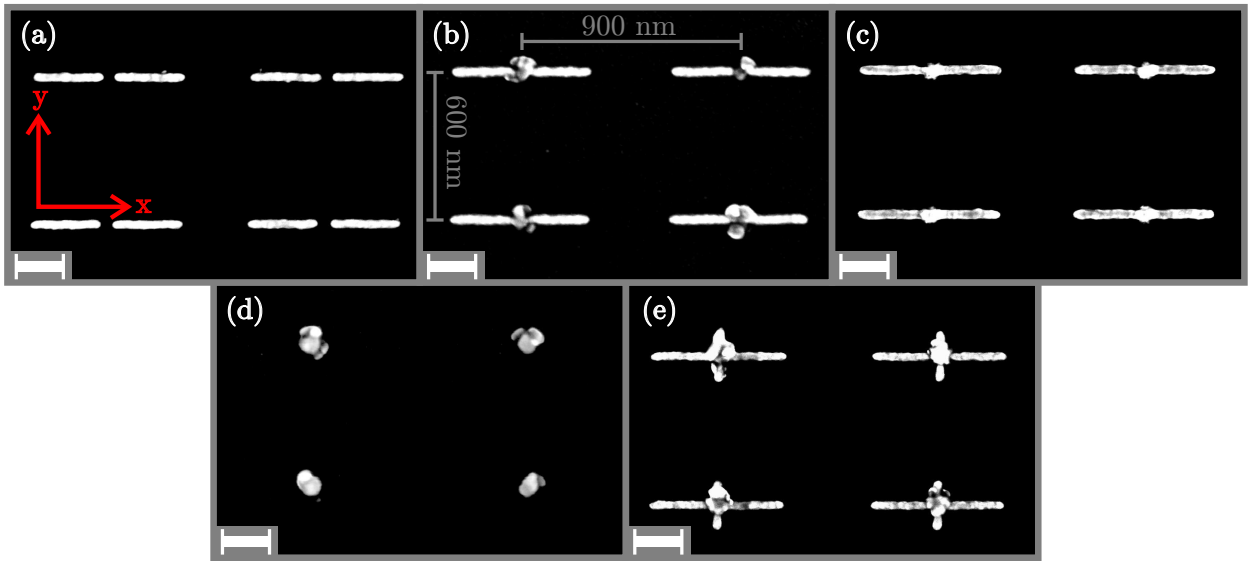

Figure 4.3: *Top-view SEM micrographs of the investigated (a) bare gold gap nanoantennas, (b) gap nanoantennas with ZnS nanoparticles, (c) gap nanoantennas with LaF_3 nanoparticles, (d) ZnS nanostructures and (e) double resonant gap nanoantenna systems with ZnS nanoparticles. The white scale bars represent 200 nm and the red arrows the used coordinate system.*

4.2.2 Experimental setup

Two separate experimental setups are used to investigate the previously introduced nanostructures and will be presented in detail in the following. A white light transmission spectroscopy setup is used to measure the linear extinction of the plasmonic nanostructures in the visible and near-infrared spectral range, whereas a second setup, employing the double-pass optical parametric generator presented in chapter 3 is used to perform second harmonic generation spectroscopy.

White light transmission spectroscopy

The home-built white light transmission spectroscopy setup for visible and near-infrared wavelengths (500-1700 nm) is schematically shown in Figure 4.4. In order to have a good approximation to a point-like light source, the light emitted by a halogen bulb is focussed (L_1) into an optical multi mode fiber (OF_1) whose end acts almost as a point emitter. The light emerging from the fiber end is collimated by a lens (L_2) and sent into the optical setup, where it first passes a Glan-Thompson polarizer[6] (P) in order to obtain linearly polarized light. A microscope objective[7] (O_1) with a numerical aperture of 0.25 is used to focus the light on the sample and a second microscope objective[8] (O_2) with a numerical aperture of 0.4 collimates the beam again. The sample is mounted on a computer controlled 3D translation stage with nanometer resolution in order to precisely address different positions on the sample. An intermediate image is produced (L_3) and the light is collimated (L_4) again. Within the

[6]Glan-Thompson Polarizer 3PTO001, Melles Griot, USA
[7]Plan N 10x/0.25, Olympus GmbH, Germany
[8]Plan Apo NIR 20x/0.40, Mitutoyo GmbH, Germany

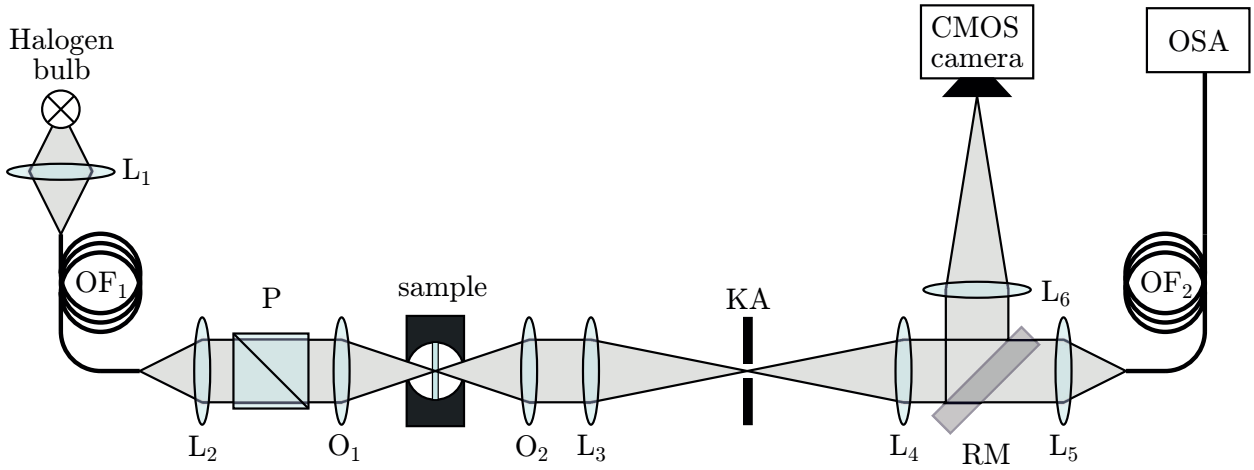

Figure 4.4: *White light transmission spectroscopy scheme: L: lens, OF: optical fiber, P: polarizer, O: objective, sample: sample with plasmonic nanostructures mounted on a computer controlled 3D translation stage, KA: adjustable rectangular knife edge aperture, RM: removable mirror, OSA: optical spectrum analyser.*

intermediate image plane an adjustable rectangular knife edge aperture (KA) is placed, to select only the relevant part of the sample for detection. The light transmitted through the selected area of the sample is guided (L_5, OF_2) to an optical spectrum analyser realized by a dual band Si/InGaAs photodiode attached to a grating monochromator.[9] With the optical spectrum analyser the transmitted intensity can be measured wavelength resolved. All transmittance spectra are normalised with respect to the transmittance right beside the gap nanoantenna array, i.e., with respect to the transmittance of the bare glass substrate with the ITO layer. Alternatively the light can be redirected using a removable mirror (RM) to produce with a long focal length lens (L_6) an image of the sample and the aperture on a CMOS camera,[10] in order to adjust the sample or the aperture.

Nonlinear spectroscopy

The setup used for the second harmonic generation spectroscopy measurements is schematically shown in Figure 4.5. As pump source the double-pass optical parametric generator (OPG) described in chapter 3 is employed. The average power of the pump beam was attenuated to below 10 mW in order to stay well below the damage threshold of the nanostructures, which was determined in preceding tests. The linear polarization in x-direction (see coordinate system in Figure 4.3) of the pump beam is controlled by the combination of a polarizer (P) and an achromatic half-wave plate (AHWP). The pump light is focused down (L_1) to approximately 30 µm spot diameter under normal incidence (z-direction) on the sample, corresponding to a peak intensity of approximately 170 MW/cm^2. The sample is mounted on a computer controlled 3D translation stage with nanometer resolution to precisely address different positions on the sample. The surface of the sample containing the nanostructures is pointing oppositely to the propagation direction of the pump beam.

[9] Acton SP2150, Princton Instruments, USA
[10] DCC1545M, Thorlabs GmbH, Germany

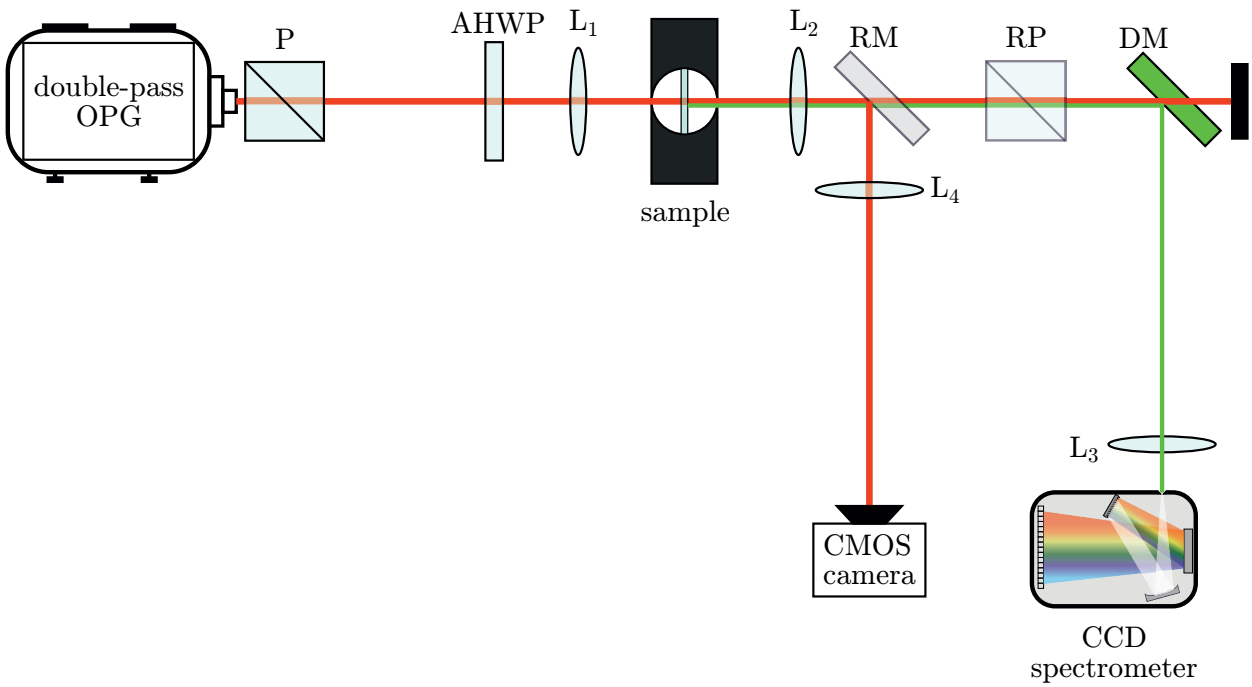

Figure 4.5: *SHG spectroscopy scheme: P: polarizer, AHWP: achromatic half-wave plate, L: lens, sample: sample with plasmonic nanostructures mounted on a computer controlled 3D translation stage, RM: removable mirror, RP: removable polarizer, DM: dichroic mirror.*

The second harmonic light emerging from the sample is collimated (L_2), separated from the residual pump light by a dichroic mirror (DM) and focussed (L_3) onto the entrance slit of a CCD spectrometer.[11] The SHG signal is recorded for different pump wavelengths in steps of approximately 20 nm. In order to eliminate any parasitic effects due to changes in the pulse shape and beam divergence when tuning the OPG, the SHG signals from the nanostructures are spectrally integrated and referenced to the weak SHG signal obtained from the ITO covered substrate surface. Additionally a removable polarizer (RP) can be used to characterize the polarization of the generated second harmonic light. If not mentioned otherwise the SHG signal is always recorded polarization unselective, in order to maximize the signal-to-noise ratio. With the help of a removable mirror (RM) and a long focal length lens (L_4) the beam/sample position can be monitored and adjusted on a CMOS camera.[10] For this purpose the OPG can be also exchanged by a white light source. Despite the fact that the camera is silicon based, it can detect the pump beam due to strong multiphoton interactions emerging at high peak powers.

[11] USB4000, Ocean Optics Inc., USA

4.2.3 Influence of dielectrics

To first assess the nonlinear properties of the thermal evaporated dielectrics, the SHG efficiency of the nanoparticle arrays and the 60 nm thin films made from ZnS and LaF_3 is compared with the SHG efficiency of the underlying ITO covered substrate surface at a fixed wavelength of 1480 nm and constant pump intensity. The results are shown in Figure 4.6 in terms of the frequency doubled spectra. In the case of the LaF_3 nanoparticle array the SHG efficiency is slightly weaker than that of the underlying ITO surface. The most likely reason for this observation is scattering of the incoming pump light. Consistently, the SHG efficiency is even more dim, if the substrate is covered with a thin film of LaF_3, leading to reflection of the incoming pump light. In case of the ZnS nanoparticle array the SHG efficiency is larger by a factor of 1.4 than that of the underlying ITO surface and by a factor of 115 larger in the case of a thin film of ZnS. The ratio between the SHG efficiency of the ZnS nanoparticle array and the thin film corresponds to the volume ratio between them. This observation is in excellent agreement with the theories for random quasi phase matching, discussed in paragraph 2.4.5. Therefore this preliminary experiment indicates that the ZnS nanoparticles are in a polycrystalline state and therefore indeed show a second order nonlinear response whereas no second order nonlinear effects can be observed from LaF_3 nanoparticles as expected.

Next, the SHG efficiency of a gap nanoantenna array with ZnS nanoparticles (connected red data points in Figure 4.7) is compared with that of an array of bare ZnS nanoparticles. At the center wavelength of the plasmonic resonance of the gap nanoantennas, the SHG signal of the hybrid plasmonic/dielectric nanoantenna array is by a factor of 500 000 larger than that of the ZnS nanoparticle array. This seems to suggest, that the SHG efficiency of the ZnS nanoparticles is indeed enhanced by the plasmonic field-enhancement.

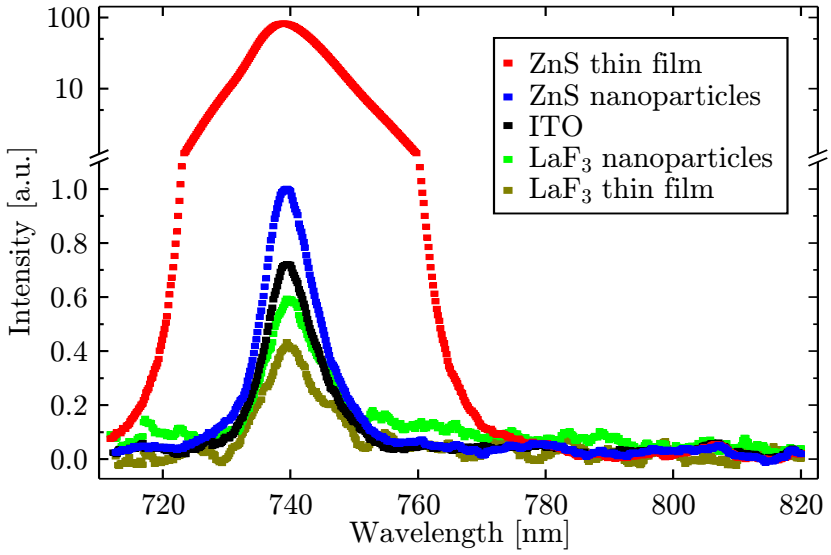

Figure 4.6: *Frequency doubled spectra of the pump beam at 1480 nm wavelengths and constant pump intensity, obtained form a thin film of ZnS (red), a ZnS nanoparticle array (blue), the ITO covered substrate surface (black), a LaF_3 nanoparticle array (green), and a thin film of LaF_3 (dark yellow).*

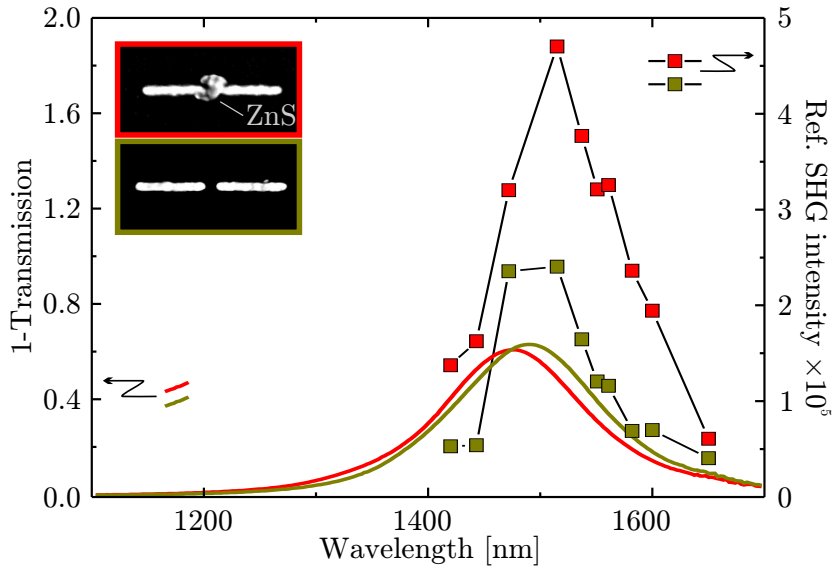

Figure 4.7: *Normal-incidence optical extinction (one minus the measured intensity transmission) spectra for x-polarized light (left axis, continuous lines) as well as the SHG intensity (right axis, connected data points) for an array of bare gold gap nanoantennas (dark yellow) and an array of gap nanoantennas with ZnS nanoparticles (red), both located on sample 1. The SHG intensity spectra are both referenced to that of an array of ZnS nanoparticles located on the same sample.*

In order to determine the main source of the nonlinear signal of the hybrid plasmonic/dielectric gap nanoantennas the linear and nonlinear spectra of an array of bare gold gap nanoantennas are compared with that of an array of gap nanoantennas with ZnS nanoparticles, both located on sample 1. The corresponding extinction (one minus measured transmission) spectra for x-polarized normal incident light are shown as continuous lines in Figure 4.7. The connected symbols represent the measured SHG spectra referenced to that of an array of ZnS nanoparticles located on the same sample. For both antenna arrays the SHG efficiency is closely following the linear extinction, which shows that the SHG is governed by the plasmonic resonance of the gap nanoantennas. A close examination of the linear extinction spectra reveals a slightly broader line width of the resonance in the case of the bare gold gap nanoantennas. A comparison of the SHG efficiencies of both antenna arrays shows a doubling of the SHG efficiency of the gap nanoantennas due to the incorporation of the ZnS nanoparticles.

To test whether the increased SHG efficiency really stems from the nonlinear properties of the ZnS, an array of bare gold gap nanoantennas and a gap nanoantenna array with LaF_3 nanoparticles, both located on sample 2, are compared in the same way as before (Figure 4.8). Again a doubling of the SHG efficiency due to the incorporation of a dielectric is observed, even as the bare LaF_3 nanoparticles did not show SHG in the preliminary experiment. A slight narrowing of the resonance line width of the hybrid antennas relative to the bare gold antennas is observed again.

To rule out any experimental artefacts, numerical calculations using the discontinuous Galerkin time-domain method [51, 125] for the bare gold gap nanoantenna arrays and gap

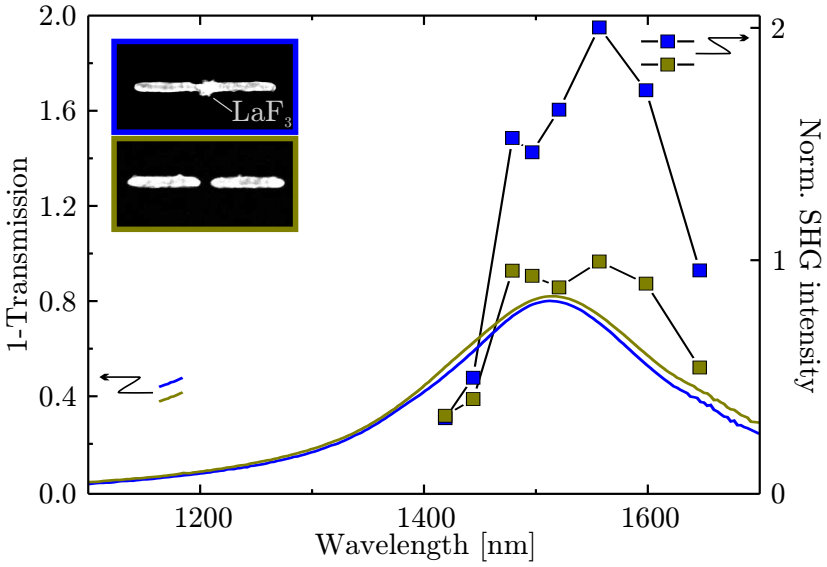

Figure 4.8: *Normal-incidence optical extinction (one minus the measured intensity transmission) spectra for x-polarized light (left axis, continuous lines) as well as the SHG intensity (right axis, connected data points) for an array of bare gold gap nanoantennas (dark yellow) and an array of gap nanoantennas with LaF_3 nanoparticles (blue), both located on sample 2. The SHG intensity spectrum is normalized to the maxima of the corresponding bare gold gap nanoantenna array.*

nanoantenna arrays with a linear dielectric were performed.[12] This method self-consistently takes the light propagation at the second harmonic frequency into account and therefore includes SHG reabsorption, emission shaping and the near to far field transition. The optical response of the metal is described by the state-of-the-art hydrodynamic Maxwell-Vlasov theory [33, 126], whose principle features are outlined in paragraph 2.4.3. Its linear limit corresponds to the Drude free-electron model, for which a plasma frequency $\omega_{\mathrm{pl}} = 1.33 \times 10^{16}$ rad/s, a collision frequency $\omega_{\mathrm{col}} = 8 \times 10^{13}$ rad/s, and a background dielectric constant of $\epsilon_\infty = 9.84$ was chosen. The refractive index of the glass substrate is taken as $n = 1.46$. The geometric parameters of the gap nanoantennas were adapted from the SEM micrographs shown in Figure 4.3(a) and (b), respectively. The length of the gap nanoantennas is 350 nm per arm in the case of the bare gold gap nanoantennas and 325 nm in the case of the hybrid gap nanoantennas. The width and the height are approximately 40 nm. The gap has a width of 50 nm and the size of the dielectric nanoparticles was chosen such that they scarcely touch the nanoantenna arms. The antennas as well as the dielectric nanoparticles were modelled with a surface roughness of around 3 nm r.m.s., by a random displacement of the vertices defining the surfaces of the geometries in the meshes, used for discretization. This mimics the experimental conditions and resulting in the observed significant SHG signal. The refractive index of the dielectric nanoparticles was varied in order to obtain overlapping resonances between the hybrid and the bare gold nanoantennas, resulting in a refractive index of $n = 3$. The deviations from the geometry parameters of the actual samples presented in paragraph 4.2.1 results from the fact, that both the antennas

[12]The calculations and modelling were performed by Dr. Yevgen Grynko, member of the research group for theoretical electrical engineering at the university of Paderborn, employing the Paderborn Center for Parallel Computing (PC2).

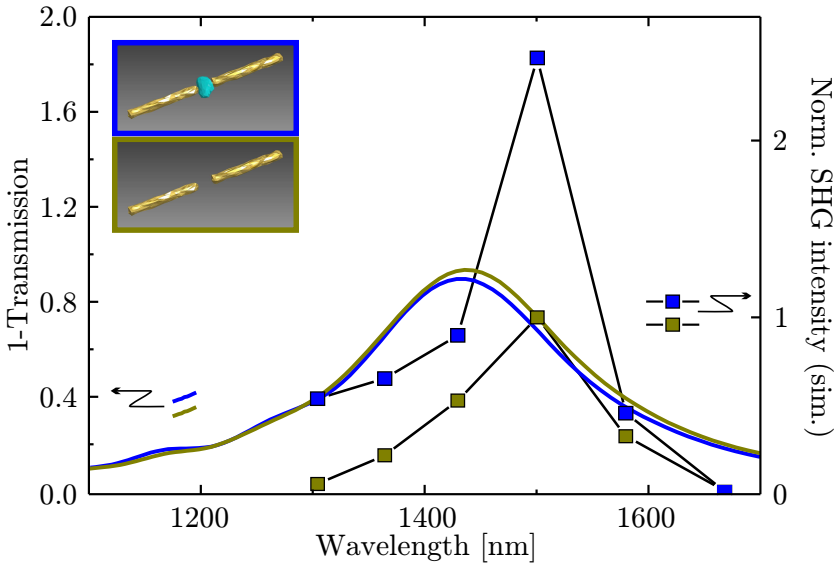

Figure 4.9: *Numerically calculated normal-incidence optical extinction (one minus the simulated intensity transmission) spectra for x-polarized light (left axis, continuous lines) as well as the SHG intensity (right axis, connected data points) for an array of bare gold gap nanoantennas (dark yellow) and an array of gap nanoantennas with linear dielectric nanoparticles (blue). The SHG intensity spectrum is normalized to the maxima of the corresponding bare gold gap nanoantenna array.*

and the dielectric nanoparticles were modelled with a surface roughness. Thus, they are not in contact with each other and the substrate surface over a large area, but only at singular points.

In order to verify the influence of a change of the dielectric environment of the gap nanoantennas on their SHG efficiency, the second order nonlinear coefficient of the dielectric nanoparticles was set equal to zero. The linear extinction calculations as well as the nonlinear SHG simulations are presented in Figure 4.9 in the same way as before the experimental results. Within the experimental as well as the numerical uncertainties the doubling of the SHG efficiency due to the incorporation of a dielectric is reproduced, as well as the line width narrowing.

A survey of the presented experimental and numerical results allows to draw several conclusions:

(i) The same efficiency enhancement is obtained, regardless whether linear LaF_3, arbitrary linear dielectric (numerical study), or nonlinear ZnS nanoparticles are used. It can thus be concluded, that the SHG efficiency enhancement of the plasmonic gap nanoantennas due to the incorporation of dielectric nanoparticles does not originate from an interplay between the plasmonic field-enhancement effect and the nonlinear optical properties of the dielectric nanoparticle.

(ii) The dominant source of the SHG signal are the gold gap nanoantennas, as the LaF_3 nanoparticles show no measurable second order nonlinearity and no nonlinearity of the nanoparticles was assumed in the simulation.

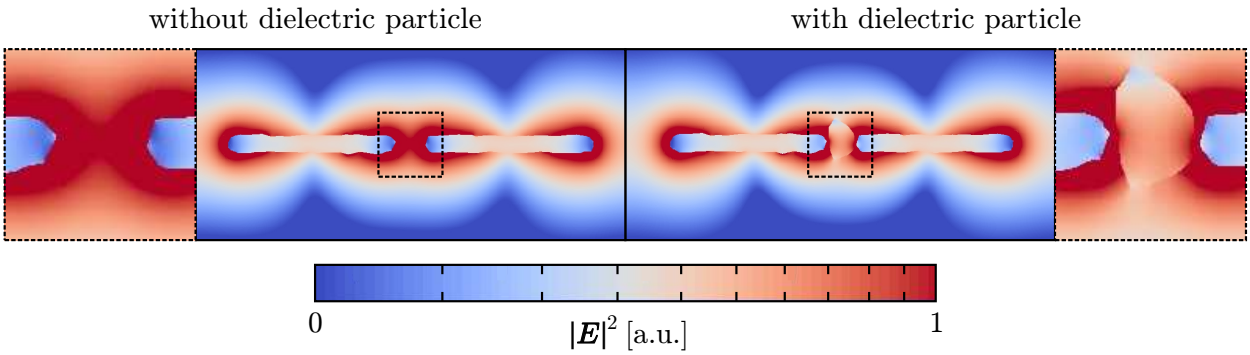

Figure 4.10: *Simulated local intensity distribution ($|\boldsymbol{E}|^2$) at a wavelength of 1450 nm, on a logarithmic colour scale of the bare gold gap nanoantenna model (left) and the model of a gap nanoantenna with a dielectric nanoparticle (right), which are used for the simulation presented in the right part of Figure 4.8. The marked gap region is magnified for better visibility.*

(iii) Even as the idealized geometry of the investigated gap nanoantennas is centrosymmetric they give rise to a SHG efficiency, which exceeds that of the nonlinear ZnS nanoparticles and thin films by many orders of magnitude.

(iv) The SHG efficiency of plasmonic gap nanoantennas can be increased by a modification of the dielectric environment and the overall geometry.

The modification of the dielectric environment and the overall geometry leads to the following phenomenon. First, a small but measurable narrowing of the resonance line width of the hybrid antennas relative to the bare gold antennas, can be seen in both sets of experiments and in the numerical simulation. This is synonymous with an increase of the quality factor Q, which is known to have a strong effect on the nonlinear performance of plasmonic nanostructures [36, 39], as can be seen from the survey in paragraph 2.4.5. Second, the modification of the overall geometry leads to a local change of the intensity distribution of the pump field as can be seen in Figure 4.10. Here, the intensity in the tips of the antenna arms is slightly but visibly higher in the case of the hybrid system, compared to the bare gold antenna.

4.2.4 Double resonant gap nanoantenna systems

In the following double resonant nanoantenna systems consisting of two gap nanoantennas oriented perpendicular to each other (see Figure 4.3(e)) are studied. One gap nanoantenna is designed to be resonant to the pump field (long horizontal orientated gap nanoantenna) and the other gap nanoantenna is designed to be resonant to the generated second harmonic light (short vertical orientated gap nanoantenna). The idea behind this design is, that the pump resonant antenna locally enhances the pump light field, in order to obtain efficient second harmonic generation, whereas the second antenna provides a resonant feedback of the generated second harmonic light and also mediates the coupling to the far field [68, 127]. In a classical resonator picture this geometry can be seen as a miniaturized version a double resonant cavity used for intracavity SHG, which is known to show higher conversion efficiencies than the case where only the pump light or the generated second harmonic light is resonantly enhanced [128, 129].

Linear extinction and SHG spectroscopy measurements are performed on an array of double resonant nanoantenna systems with ZnS nanoparticles. For reference an array of only pump resonant gap nanoantennas with ZnS nanoparticles is used (see Figure 4.11). Both, the pump resonant gap nanoantennas and the long nanoantennas of the double resonant nanoantenna systems, have nominally the same length. In the case of the double resonant nanoantenna systems a resonance in the extinction spectrum at approximately 780 nm wavelength for y-polarized incident light is observed, due to the presence of the short nanoantennas, which is absent in the case of the only pump resonant nanoantennas. The resonance of the long nanoantennas, which is only visible for x-polarized incident light, is slightly red-shifted and

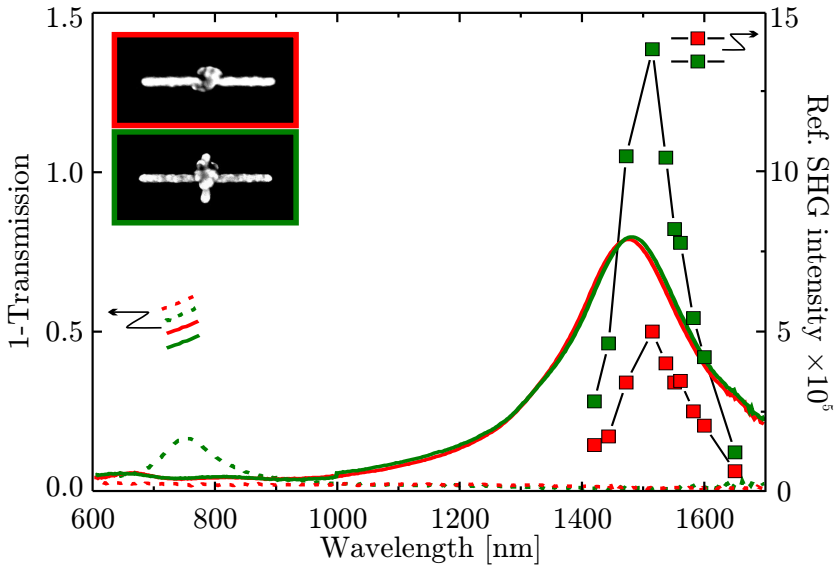

Figure 4.11: *(a) Normal-incidence optical extinction (one minus the measured intensity transmission) spectra for x-polarization (left axis, continuous lines) and y-polarization (left axis, dashed lines), and the SHG intensity (right axis, connected data points) for an array of ZnS gap nanoantennas with ZnS nanoparticles (red) and an array of double resonant gap nanoantenna systems with ZnS nanoparticles (green). The SHG intensity spectra are both referenced to that of an array of ZnS nanoparticles located on the same sample.*

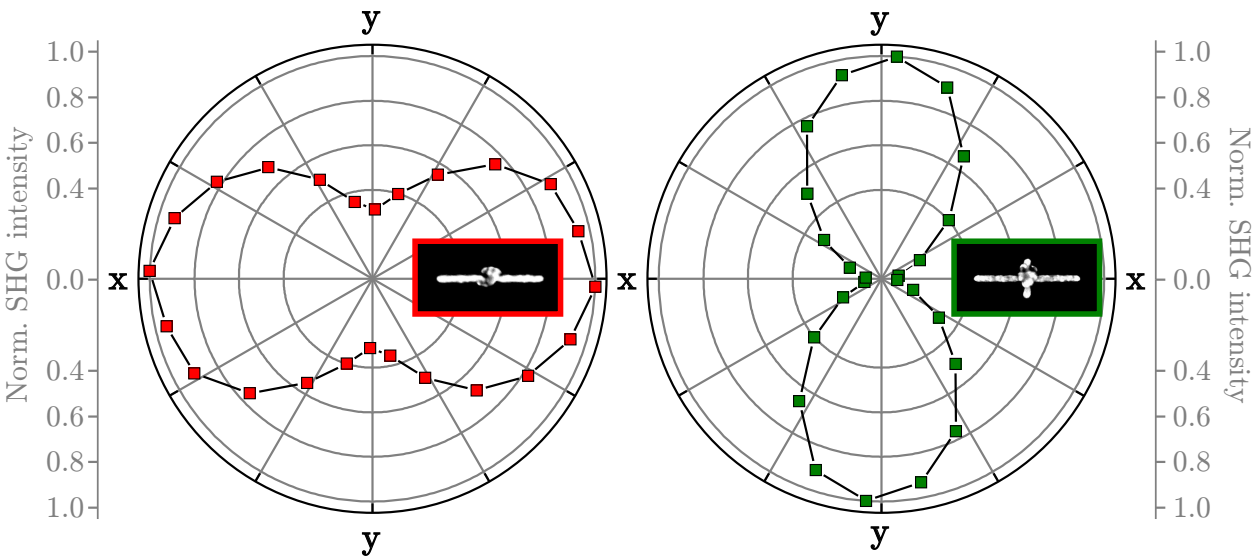

Figure 4.12: *Polar diagrams of the polarization state of the generated second harmonic light from an array of gap nanoantennas with ZnS nanoparticles (left diagram) and an array of double resonant gap nanoantenna systems with ZnS nanoparticles (right diagram). In both cases the pump light was x-polarized. All data points are normalized to the maxima of the corresponding data set.*

its line width is marginally increased in the case of the double resonant systems compared to the only pump resonant gap nanoantennas. The red-shift and the line width increase originate from a coupling between the short and the long antennas. Investigation of the linear extinction spectra of several different double resonant gap nanoantenna systems revealed the red-shift and the line width increase to be independent of the actual nanoantenna lengths (not shown). By comparing the SHG spectroscopy data of both structures (see Figure 4.11) it can be seen, that the feedback provided by the additional short nanoantennas strongly enhances the SHG efficiency of the hybrid nanoantenna systems, even as the previously mentioned increase of the line width should act counterproductive.

The additional short nanoantenna in the case of the double resonant gap nanoantenna systems does not only enhance the SHG efficiency, but it also mediates the coupling to the far field of the generated second harmonic light. This becomes evident by examining the polarization properties of the second harmonic light generated by the only pump resonant gap nanoantennas with ZnS nanoparticles and the double resonant gap nanoantenna systems with ZnS nanoparticles. The results are shown in polar diagrams in Figure 4.12. In the case of the only pump resonant nanoantennas the second harmonic light is weakly polarized along the long nanoantenna axis (x-polarized), whereas significant larger degree of polarization is obtained in the case of the double resonant nanoantenna systems, this time along the axis of the short nanoantennas (y-polarized). These results indicate, that double resonant nanoantenna systems offer the opportunity to influence the far field properties of the generated second harmonic light.

For the sake of completeness the SHG efficiency of both antenna geometries was checked for y-polarized pump light. However, in both cases no SHG signal could be measured within the measurement resolution.

4.3 Two-photon resonant metamaterials

It was shown in the previous section, that the SHG efficiency of plasmonic nanostructures, which are resonant for both the pump light (one-photon resonant) and for the generated second harmonic light (two-photon resonant), exceeds that of only one-photon resonant nanostructures. In the case of antenna like structures this result is in agreement with previous studies [41], but for more complex nanostructures evidence was found, that two-photon resonances act as a loss channel [40]. In all these investigations the second harmonic generation is attributed to the strong near field enhancement of the pump wave, whereas the additional two-photon resonances are believed to provide a feedback, scatter, or absorb the generated second harmonic light, thus representing a "passive component". In contrast to this, in an earlier study on SHG from silver nanoisland films with varying volumes using a fixed pump frequency evidence was found that an enhancement due to a two-photon resonance is achievable [130].

For dielectric materials an enhancement of the SHG efficiency, or at least the second order nonlinear susceptibility, due to two-photon resonances is a quite usual phenomenon. It can be observed for example in semiconductors, when the band gap energy is approximately two times the photon energy of the incident pump light [74, 131]. Indeed, this phenomenon in general is a direct consequence of Miller's law, presented in paragraph 2.4.2, which predicts two-, as well as one-photon resonances for the nonlinear susceptibility for second harmonic generation.

In this section, which is closely following [132], second harmonic generation from plasmonic nanostructures, which only exhibit a two-photon resonance, will be investigated. Specifically, SHG spectroscopy measurements will be analysed in the framework of a metamaterial picture presented in paragraphs 2.3.4 and 2.4.5, based on an anharmonic oscillator model.

4.3.1 Materials and experimental methods

To study the influence of the two-photon resonance on the SHG efficiency of plasmonic nanostrucutres, a series of arrays of centrosymmetric gold nanoantennas is examined. Within this series the length of the antennas increases from 100 nm to 135 nm in 5 nm steps (SEM

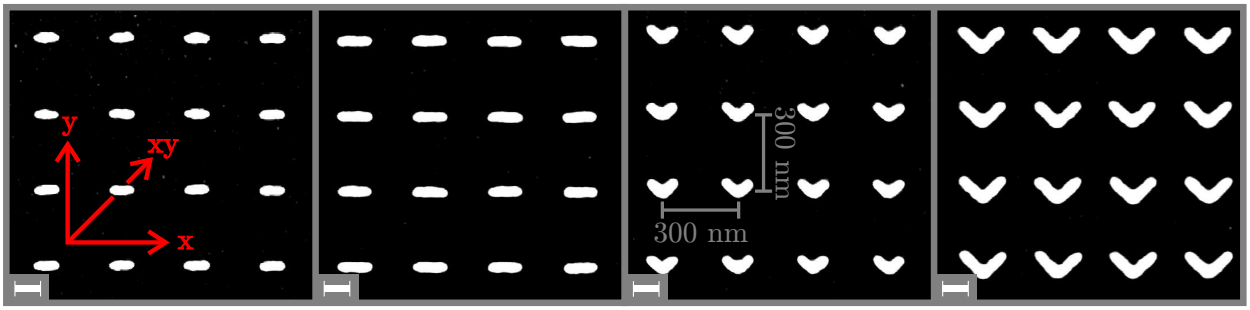

Figure 4.13: *Top-view SEM micrographs of selected gold nanostructures presenting the extremal investigated antennas and the two different V-shaped structures. The red arrows indicate the different incident linear polarizations used in the following. The white scalebars represent 100 nm.*

micrographs of the extremal antennas are shown in Figure 4.13). In addition noncentrosymmetric V-shaped gold nanostructures with two different arm lengths of 90 nm and 140 nm, respectively will be investigated. All nanostructures have an arm width and height of 40 nm and are arranged on a 300 nm x 300 nm square lattice with a footprint of 70 µm x 70 µm. The gold nanostructures were fabricated by standard electron-beam lithography and lift-off techniques as presented in section 4.1. As the nanostructures consist of gold only, the fabrication scheme is truncated after step (e) of Figure 4.1.

To measure the linear response of the nanostructure arrays the same white-light transmission spectroscopy setup as depicted in Figure 4.4 and explained in paragraph 4.2.2 will be used. As the goal of this section is to analyse the influence of the linear spectral response of plasmonic nanostructures on their SHG efficiency, i.e., to measure the frequency dependency of this nonlinear process, the resolution of the SHG spectroscopy setup/measurement compared to section 4.2 has to be improved. One possible reason for the slightly noisy results presented in section 4.2 might be the use of the SHG signal obtained from the ITO covered substrate surface as reference to eliminate parasitic effects associated with the detuning of the OPG. First the SHG signal from ITO covered surface in general is very weak as can be seen by comparing Figures 4.6 and 4.7, resulting in a low signal-to-noise ratio. Second, the second harmonic generation from ITO films is not studied in detail yet, thus an unknown spectral dependency of this process might also disturb the measurements [133, 134].

To overcome this a reference arm is added to the previously used setup as schematically shown in Figure 4.14. In the reference arm, which is accessed by a removable mirror (RM_1),

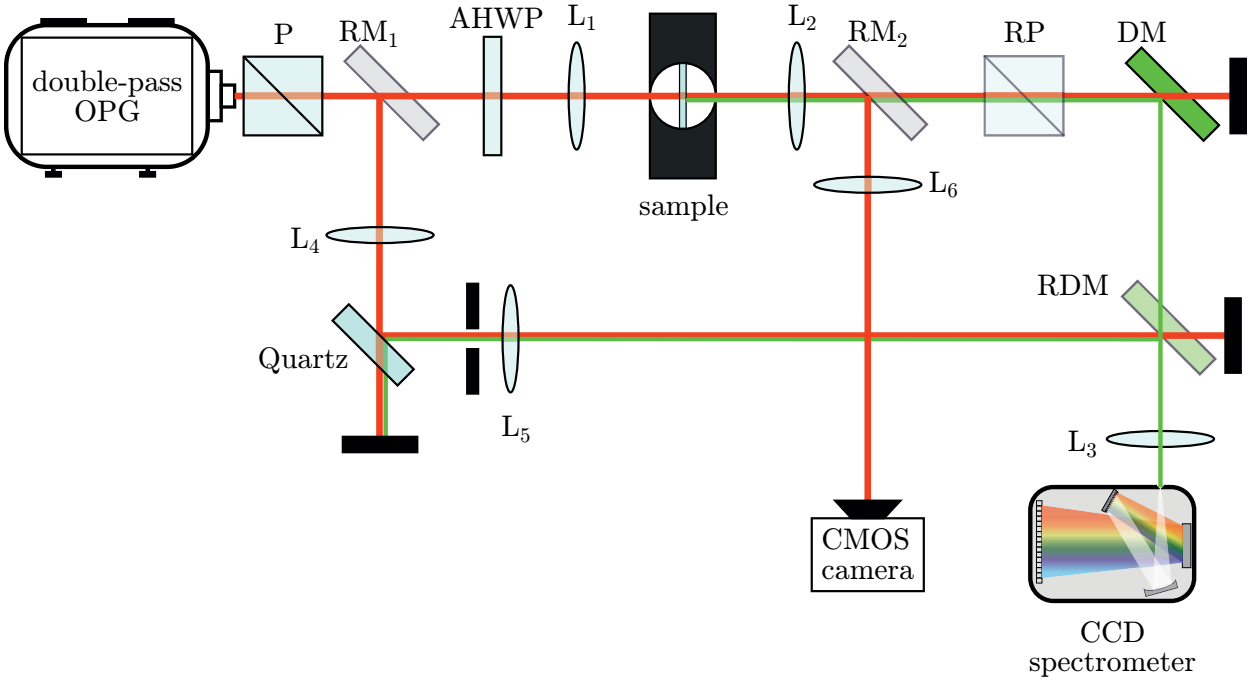

Figure 4.14: *SHG spectroscopy scheme: P: polarizer, RM: removable mirror, AHWP: achromatic half-wave plate, L: lens, sample: sample with plasmonic nanostructures mounted on a computer controlled 3D translation stage, RP: removable polarizer, DM: dichroic mirror, RDM: removable dichroic mirror.*

the horizontal polarized (x-direction) pump beam coming from the OPG is focused (L_4) on the surface of a z-cut quartz plate under 45° incidence. The second harmonic light generated at the surface of the quartz plate is collimated (L_5) and coupled (RDM, L_3) into the CCD spectrometer. An aperture between the quartz plate and the collimating lens (L_5) is used to block the second harmonic light emerging from the quartz plate volume and reflection at its back side. The optics used in the reference arm are similar to those used in the measurement arm, thus the SHG signal obtained from the plasmonic nanostructures can not only be referenced but also compared to that of the quartz surface. A quartz surface is used as reference sample, as surface second harmonic generation does not suffer from phase-matching effects as explained in paragraph 2.4.5. Furthermore, the band gap of quartz is located below 200 nm, therefore its linear spectral response in the visible and near-infrared spectral range is remarkable flat [135], which will lead to a wavelength independent nonlinear response in this spectral range, as can be seen from equation (2.88). To further increase the signal-to-noise ratio the average pump power is increased to 50 mW, as preceding tests showed, that the damage threshold of plasmonic nanostructures lacking a one-photon resonance is considerably higher than that of plasmonic nanostructures owning a one-photon resonance.

4.3.2 Two-photon resonant nanoantennas

Figure 4.15 depicts the measured linear optical extinction (one minus the measured intensity transmission) spectra versus the antenna length for x-polarization (see Figure. 4.13), presented as an interpolated contour plot. The maxima of the measured spectra are marked as circles and connected as guide to the eye. Obviously, the plasmonic resonances of nanoantennas can be very finely tuned through the second harmonic range of the employed pump source (700 nm to 830 nm), by only slight variations of the antenna lengths. Furthermore, the investigated nanoantennas exhibit only a single plasmonic mode in the spectral range relevant for this work (700 nm to 1680 nm), as can be seen in the inset showing the complete extinction spectra of the longest investigated antennas for both x- and y-polarization.

Due to the lack of a one-photon resonance it is not a priori clear whether these nanoantennas will show second harmonic generation or not. As the nanoantennas are centrosymmetric it is also not possible to predict which component of the nonlinear susceptibility tensor is non vanishing, except for the fact that the used setup only allows for normal incidence measurements. Thus, a measurement of the SHG efficiency of the longest investigated antennas for different polarization angles of the pump beam in steps of 10° is done first. For this measurement a fixed wavelength of 1640 nm, corresponding to a two-photon resonant excitation is used. The results are illustrated in the left graph of Figure 4.16. One can clearly see that the SHG for y-polarized pump light is vanishingly small compared to the case of x-polarized pump light. This finding can be qualitatively explained as follows. For x-polarized light the antennas exhibit a pronounced resonance at around 800 nm wavelengths, whereas the plasmonic resonance for y-polarized light at around 500 nm is weak and strongly damped (see inset of Figure 4.15). In terms of a simple harmonic oscillator model one expects that the strong resonance for x-polarization gives rise to a stronger contribution to the linear susceptibility at the pump wavelength, than the weak resonance for y-polarization. This explains the dependence of the SHG signal on the polarization of the pump beam.

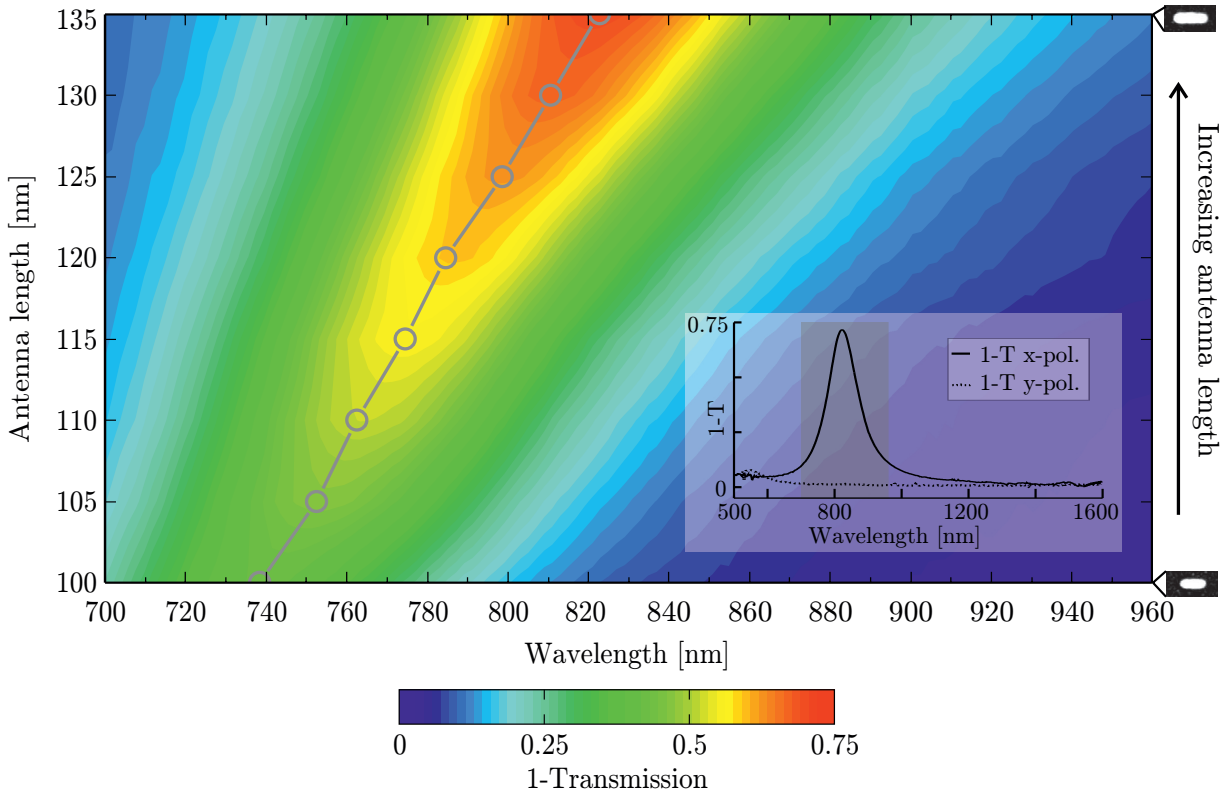

Figure 4.15: *Normal-incidence optical extinction (one minus the measured intensity transmission) spectra of the antenna arrays versus the antenna length for x-polarized light, presented as an interpolated contour plot. The maxima of the actual data-points are marked as circles and connected as guide to the eye. The inset shows the spectra for the longest antennas for x- (—) and y-polarization (· · · ·), the grey area illustrates the wavelength range of the contour plot. The SEM micrographs (200 nm × 100 nm) on the right depict the extremal antenna lengths.*

The right part of Figure 4.16 shows the polarization of the generated second harmonic light for x-polarized pump light. Here, it becomes evident, that the SHG signal is clearly polarized along the antenna axis (x-axis). This finding is consistent with equation (2.88), as $\chi_{xx}(2\omega) \gg \chi_{yy}(2\omega)$, which can be evaluated by equations (2.46) and (2.47) from the linear extinction measurements. Thus, only the $\chi^{\mathrm{SHG}}_{xxx}$ element of the second order nonlinear susceptibility tensor is non vanishing in the case of two-photon resonant nanoantennas.

Based on the polarization measurements, SHG spectroscopy measurements are performed with x-polarized pump light and polarization unselective detection for all nanoantenna arrays. In Figure 4.17 the referenced SHG signal is depicted as function of the second harmonic wavelength and the antenna length. The maxima of the measured SHG spectra are marked as black circles and connected as guide to the eye. For direct comparison, the maxima of the measured linear extinction spectra are also plotted as grey connected circles. Obviously, the spectral maximum of the SHG signal is closely following the linear resonance of the antennas.

According to the anharmonic oscillator model, presented in paragraphs 2.4.2 and 2.4.2, the second order nonlinear susceptibility for SHG $\chi^{\mathrm{SHG}}_{ijk}$ can be expressed by the linear susceptibilities χ_{ii} at the frequencies ω and 2ω. The analysis of polarization measurements presented

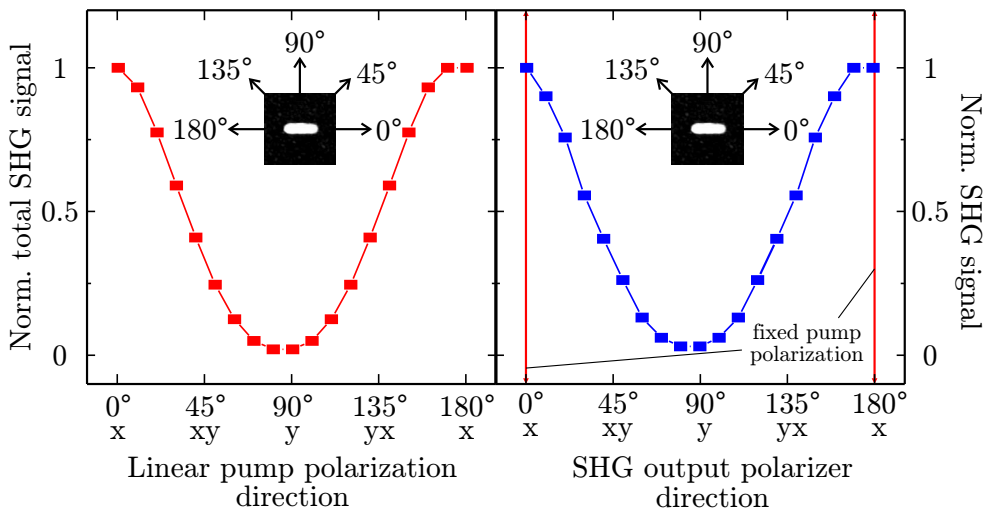

Figure 4.16: *(Left) Normalized total SHG signal of the longest antennas as function of the angle of polarization of the linearly polarized incident pump beam. (Right) Corresponding normalized SHG signal as function of the linear output polarizer. The red vertical lines indicate the fixed linear polarization of the respective pump light. All data points are normalized to the maximum of the individual measurement and connected as guide to the eye. The SEM micrographs show a 275 nm x 275 nm section of the investigated arrays.*

in Figure 4.16 revealed, that both the pump light and the generated second harmonic light address the same plasmonic mode, in the case of second harmonic generation from the nanoantennas. Therefore the linear susceptibilities have not to be evaluated explicitly to obtain $\chi^{\mathrm{SHG}}_{xxx}$. Instead, the measured extinction spectra have been fitted to a Lorentzian line shape, regarding equation (2.46), to obtain $\chi^{\mathrm{SHG}}_{xxx}$ with the help of equation (2.111). The thickness z of the metamaterial composed by the antennas, the factor a_{xxx} describing the nonlinear restoring force, and the nonlinear susceptibility and the proportionality constant η in the case of the reference measurements, i.e., the overall proportionality between the generated second harmonic intensity and the pump intensity for the reference, are still unknown. We note that z is, due to the used fabrication method, the same for all nanoantenna arrays and the proportionality factor to the quartz reference is wavelength independent. In the spirit of R. Miller's findings for solid state matter (see paragraph 2.4.2), it will be assumed in the following that a_{xxx} is constant for a specific metamaterial design, i.e., for the investigated nanoantenna arrays. Thus, the discussed factors can be combined and obtained by first evaluating the spectral dependency of second harmonic generation from a single nanoantenna array through the linear extinction measurement and second, comparing this result to the referenced SHG spectrum, measured for that nanoantenna array. Finally, the SHG spectra of all other nanoantenna arrays can then be predicted from their linear extinction spectra.

In the right part of Figure 4.17 the referenced SHG signals calculated with the above discussed method from the linear extinction measurements and the SHG spectrum of the nanoantennas with a length of 115 nm are presented in the same way as the actual measurements. The spectral positions of the maxima of the SHG signal from the measurements and the calculations are in good agreement (compare black circles in the left part of Fig-

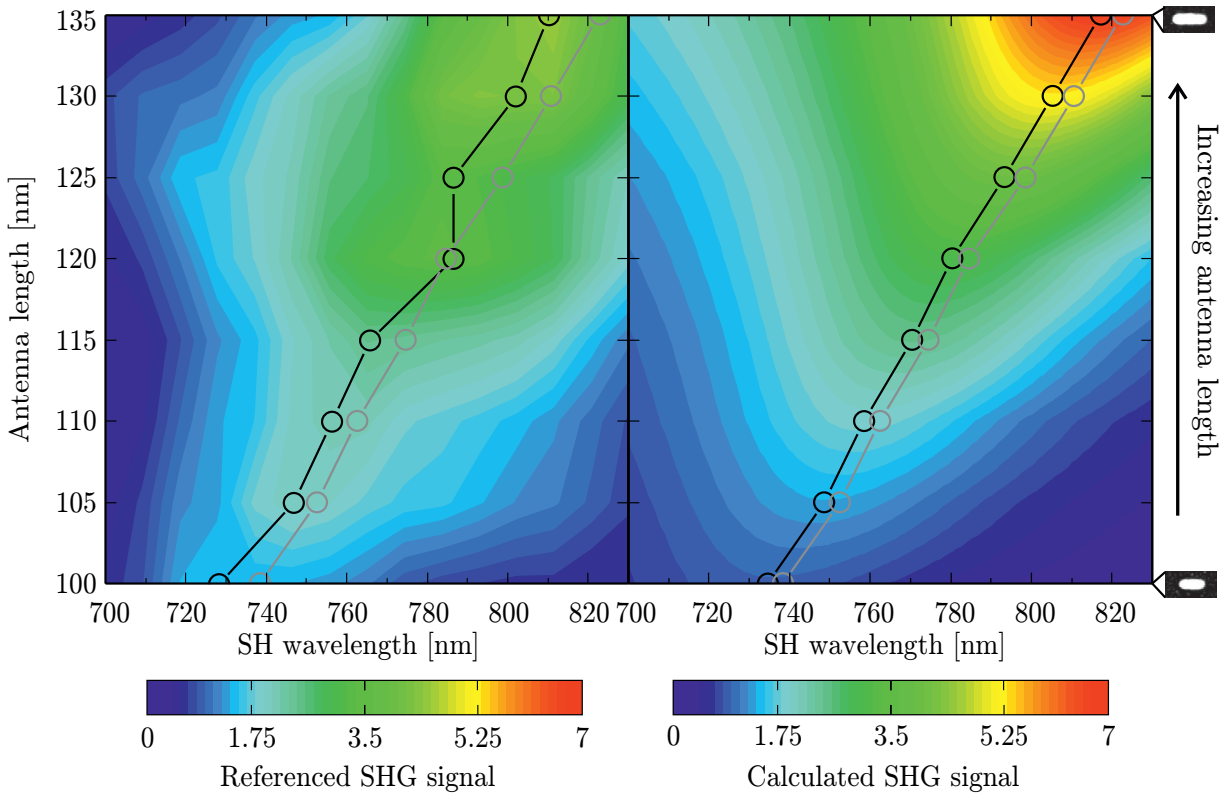

Figure 4.17: *(Left) Measured SHG signal referenced to the surface SHG signal of a quartz plate as function of the second harmonic (SH) wavelength versus the antenna length. (Right) SHG signal calculated from the extinction spectra and normalized for an antenna length of 115 nm. The maxima of the actual data-points are marked as black circles and connected as guide to the eye. The connected grey circles depict the maxima of the linear extinction. All measurements were taken with x-polarized incident light. The SEM micrographs (200 nm × 100 nm) on the right depict the extremal antenna lengths.*

ure 4.17 with those in the right part). Since the antenna arrays exhibit only a plasmonic resonance at the second harmonic frequency (see inset of Figure 4.15), this clearly shows that the SHG efficiency of metamaterials can be significantly enhanced by utilizing a two-photon resonance. In the actual measurement as well as the calculation, the spectral maxima of the SHG signals are slightly blue shifted with respect to spectral positions of the maxima of the linear extinction measurements (compare black and grey circles in Figure 4.17). This is due to the fact, that the plasmonic resonance of the nanoantennas does not show an exact Lorentzian line shape but is slightly deformed for lower wavelength due to the increasing intrinsic absorption of the gold. A slight deviation between absolute values of the maxima (marked as black circles) in both parts of Figure 4.17 can be observed. However the overall good agreement between experimental data and calculations justifies a posteriori the assumption of a constant a_{xxx} for the investigated antennas.

4.3.3 Noncentrosymmetric structures

Next, second harmonic generation from noncentrosymmmetric V-shaped structures with two different sizes will be investigated. Under the assumption, that the symmetry forbidden contributions to SHG are much weaker than the contributions arising from the symmetry breaking of the underlying geometry, the second-order nonlinear susceptibility for normal incidence should be dominated by the four elements $\chi^{\mathrm{SHG}}_{xxy} = \chi^{\mathrm{SHG}}_{xyx}$, $\chi^{\mathrm{SHG}}_{yxx}$, and $\chi^{\mathrm{SHG}}_{yyy}$ (see paragraphs 2.4.2 and 2.4.5). To test the contributions of the different elements, the SHG polarization properties of the V-shaped structures at the respective two-photon resonance (pump wavelengths 1600 nm and 1500 nm) were measured, in the same way as for the nanoantennas in the previous paragraph. In the case of the smaller Vs, a strong SHG signal is obtained for xy-polarized pump light only (see upper left part of Figure 4.18), resulting in x-polarized second harmonic light as shown in the upper right part Figure 4.18. These observations identify the element $\chi^{\mathrm{SHG}}_{xxy}$ as the dominant source of the SHG signal. The slight

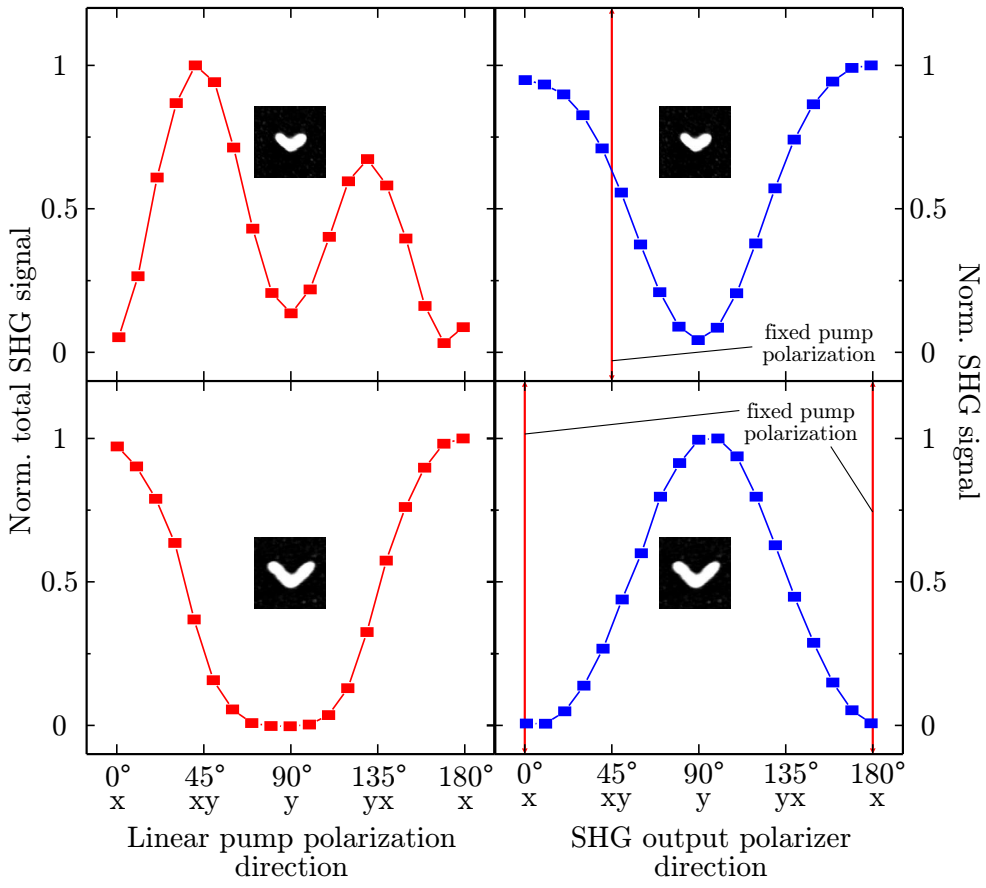

Figure 4.18: *Normalized total SHG signal of the small V-shaped (upper left), and the large V-shaped (lower left) structures as function of the angle of polarization of the linearly polarized incident pump beam. The SEM micrographs show a 275 nm x 275 nm section of the investigated arrays. (Upper right), (lower right), Corresponding normalized SHG signal as function of the linear output polarizer. The red vertical lines indicate the fixed linear polarization of the respective pump light. All data points are normalized to the maximum of each individual measurement and connected as guide to the eye.*

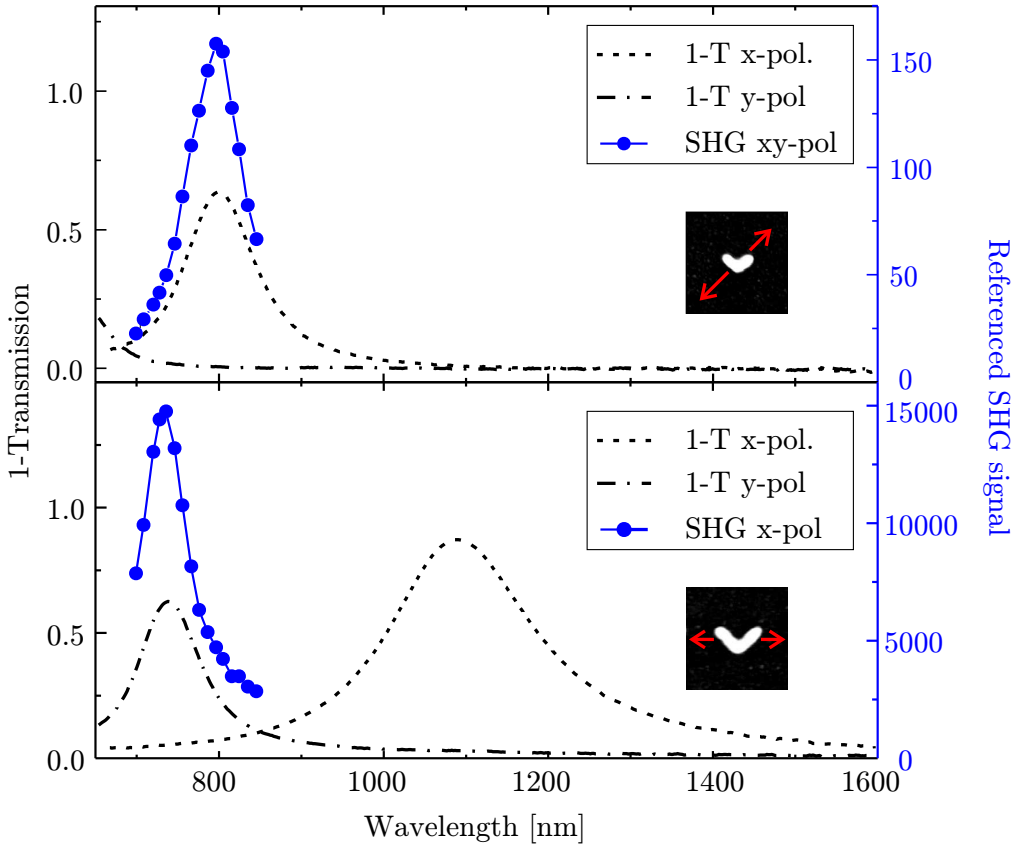

Figure 4.19: *(Top) Normal-incidence optical extinction (one minus the measured intensity transmission) spectra for x- (– · –) and y- (- -) incident polarization as well as the referenced SHG signal (–●–) of the small V-shaped structures obtained with xy-polarized pump light as function of the second harmonic wavelength. (Bottom) Experimental results represented as in the top graph for the large V-shaped structures. This time the pump light for the SHG experiments was x-polarized. The SEM micrographs show a 400 nm × 400 nm section of the investigated arrays, wherein the red arrows indicate the linear polarization of the respective pump light.*

asymmetry between 45° and 135° can be probably explained by fabrication imperfections. In contrast, for the bigger Vs (lower part of Figure 4.18) the strongest SHG signal is observed for x-polarized pump light, resulting in y-polarized SH light. Thus, $\chi^{\mathrm{SHG}}_{yxx}$ is the dominant contribution in the case of the bigger Vs.

To understand why for both sizes of the Vs only one, but not the same, element of the χ^{SHG} tensor dominates, one has to look at the linear optical extinction spectra and the nonlinear spectroscopy data presented in Figure 4.19. In the case of the small Vs a strong resonance can be observed in the extinction for x-polarized light centred at around 800 nm wavelength, whereas no resonance for y-polarized light can be observed within the relevant spectral range. As a result, the generation of x-polarized second harmonic light is enhanced by a two-photon resonance, which can be clearly observed in the SHG spectrum (see top of Figure 4.19). The only symmetry allowed tensor element for the generation of x-polarized SH light is $\chi^{\mathrm{SHG}}_{xxy}$ which demands xy-polarized pump light as observed in the upper left part of Figure 4.18. In the case of the bigger Vs (bottom of Figure 4.19) a resonance in the linear extinction centred at around 740 nm wavelength can be observed for y-polarized light and a second resonance

centred at 1100 nm wavelength for x-polarized light. The extinction-resonance at 740 nm gives rise to a two-photon resonance for both the $\chi^{\mathrm{SHG}}_{yxx}$ and the $\chi^{\mathrm{SHG}}_{yyy}$ element. However, the linear extinction-resonance at 1100 nm has a non-negligible overlap with the pump light for x-polarization. Since $\chi_{xx}(\omega)$ enters quadratically in $\chi^{\mathrm{SHG}}_{yxx}$ but not in $\chi^{\mathrm{SHG}}_{yyy}$, one finds that $\chi^{\mathrm{SHG}}_{yxx} \gg \chi^{\mathrm{SHG}}_{yyy}$.

Inspection of Figure 4.19 shows that the maximum SHG signal of the large Vs is approximately two orders of magnitude larger than that of the small Vs. This can not only be explained by the larger amount of gold, which enters equations (2.88) and (2.111) via the electron number density. Rather, one has to keep in mind, that the large Vs represent a double resonant plasmonic nanostructure, as discussed above, while in the case of the small Vs the second order nonlinear susceptibility is only two-photon resonant. In contrast to the results of paragraph 4.2.4 and earlier studies on second harmonic generation from double resonant plasmonic nanostructures [40, 41, 136] this result clearly demonstrates the constructive influence of a two-photon resonance on the SHG efficiency, as the spectral evolution of the SHG signal is governed by the two-photon resonance and is not superimposed by a strong one-photon resonance.

It is also interesting to compare the maximal obtained SHG signal from the small Vs to that of the measurements on the antennas. Even as both geometries exhibit comparable linear extinction spectra, a 30 times stronger SHG signal is observed from the noncentrosymmetric Vs. This shows that the symmetry selection rules for the second order nonlinear susceptibility tensor elements play, as expected, a dominant role for metamaterials. However, the observed ratio is significant smaller than those presented in comparisons on one-photon resonant centro- and noncentrosymmetric plasmonic nanostructures [32, 33, 37], where ratios of more than 100 are reported. This is quite surprising as the dependency of the nonlinear susceptibility on the resonance frequency and on the symmetry of the electron potential, accounted by a_{ijk} in equation (2.88), are segregated in the anharmonic oscillator model. This discrepancy is more likely due to the fact, that deviations from the idealized geometry and symmetry of plasmonic nanostructures, originated in fabrication method associated issues, are more pronounced for small structures, which give rise to two-photon resonances, than for large structures which give rise to one-photon resonances.

5

Conclusions

In this thesis second harmonic generation (SHG) from plasmonic nanostructures and metamaterials composed of those have been experimentally investigated with spectroscopic methods. The experimental findings are furthermore supported by either numerical or analytical calculations. The main results of this thesis are: (i) The design, implementation and characterization of a frequency tunable, high intensity light source, suitable for the spectroscopic investigation of nonlinear processes; (ii) the clarification of the origin of the nonlinear response of hybrid plasmonic/dielectric nanoantennas; (iii) the exposition of the influence of two-photon resonances, i.e., resonances for the generated second harmonic light, on the spectral dependency and the efficiency of SHG from plasmonic nanostructures and metamaterials composed of those.

For the SHG spectroscopy experiments conducted in this thesis, a high power double-pass femtosecond optical parametric generator (OPG) operating with long term stability at a repetition rate of 42 MHz has been designed and demonstrated. A signal output of more than two watts average power and nearly 55% pump to signal conversion efficiency has been obtained by pumping the setup based on a magnesium oxide doped periodically poled lithium niobate crystal directly with an Yb:KGW laser oscillator, without any further amplification. The signal is tunable from 1370 nm to at least 1650 nm and pulse durations below 200 fs were achieved without further compression techniques. The setup consists completely of commercial of the shelf available parts, which had not to be optimized for ultra short pulse applications, resulting in a very cost effective system. Compared to alternative frequency tunable short pulse systems, i.e., commercial optical parametric oscillators and amplifiers, the presented OPG is also very compact and insensitive to external perturbations and thus an interesting alternative to those. Finally this system proofed its usability and reliability in the experiments conducted in this thesis, far more than in the actual characterization.

Prior to the actual experiments on plasmonic nanostructures a fabrication method based on electron beam lithography and thin film deposition by thermal evaporation was developed, which allows to combine different metallic and dielectric nanostructures with nanometer precision. Due to a high degree of automation and parallelization the used method allows the reproducible fabrication of samples, also for further research projects. Furthermore it is applicable for a large variety of materials.

To analyse the interplay between the plasmonic field-enhancement effect, inherent to plasmonic nanostructures, and the nonlinear optical properties of dielectric nanoparticles a comparison of the SHG efficiency of nonlinear dielectric nanoparticles with bare gold nanoantennas, and hybrid dielectric/plasmonic nanoantennas containing either linear or nonlinear dielectric nanoparticles was conducted. By combining the results of linear extinction measurements and SHG spectroscopy it was shown, that an increase of the SHG efficiency of plasmonic nanoantennas, obtained by filling their feed gaps with dielectric nanoparticles, is independent of the nonlinear properties of the dielectric. This experimental result was also supported by numerical simulations. Furthermore these experiments showed that the SHG efficiency of plasmonic nanoantennas is several orders of magnitude higher than that of the used nonlinear dielectric nanoparticles. Additional experiments showed, that a simple combination of two nanoantennas to a double resonant nanoantenna system provides not only a strong enhancement of the SHG efficiency but also offers control over the polarization properties of the generated second harmonic light.

Inspired by the results from double resonant nanoantenna systems, plasmonic nanostructures were investigated which show only a resonance for the generated second harmonic light. With the help of linear and SHG spectroscopy on a rather large series of nanoantenna arrays, exhibiting spectral distinct plasmonic resonances, it was shown, that these two-photon resonances enhance the SHG efficiency. Furthermore two-photon resonant noncentrosymmtric nanostructures with and without a weak one-photon resonance were studied. This study proofed the validity of the general symmetry selection rules for SHG in the case of plasmonic nanostructures. It allowed also to analyse the spectral influence of a two-photon resonance in the case of a double resonant plasmonic system without the interference of a strong one-photon resonance for the pump light. With this, the previous result, that a further enhancement of the SHG efficiency is possible by designing nanostructures, which are not only resonant for either the pump or the generated second harmonic light, but for both, is reinforced. Finally the results were qualitatively and in part also quantitatively explained in a metamaterial picture, connecting the results of the linear extinction spectra with those of the SHG spectroscopy measurements via an anharmonic oscillator model.

Outlook

The presented double-pass OPG showed a superior performance, but is still a prototype. A possibility to decrease the size of the system would be to replace all lenses by curved mirrors. With this upgrade also changes of the beam divergence occurring when the signal wavelength is detuned would be diminished. As part of a complete automation of the system it would be also interesting to replace the nonlinear crystal equipped with discrete poling periods by a crystal with a so called fan out poling design. In such a design the poling period is not changed in discrete steps but continuously over the crystal. With such a crystal a continuous tuning could be achieved avoiding a temperature control of the crystal. A combination of these improvements would also allow to directly integrate the OPG in the housing of the pump laser. For several applications it would be also interesting to change the setup in a way that the idler light can be used. For this purpose optics could be employed which are non absorptive in the wavelength range from 2000 nm to 4500 nm, but it is questionable whether dichroic mirrors can be fabricated, which work over the combined signal and idler wavelength range. Furthermore the feedback for the signal and idler light has to be separated due to their unequal group velocities, which would make the system more complicated. The main advantage of the double-pass OPG compared to optical parametric oscillators and amplifiers operating in the femto- and picosecond regime is, that it does not need to be synchronised to the pump or seed source. Therefore it would be highly interesting to test this setup with other pump sources. Several industrial grade high average power femtosecond lasers with a central wavelength of 1030 nm and 1040 nm work at repetition rates of several MHz and not several tens of MHz. The peak intensity of these lasers is accordingly higher, thus the OPG should work without any changes. The main disadvantage of the OPG compared to an optical parametric oscillator are the pulse to pulse fluctuations as well in the intensity, as in time. To overcome this, the double-pass optical parametric generator could be used as an optical parametric amplifier seeded by a tunable continuous wave external cavity diode laser, to start the parametric amplification not from vacuum noise, but from a well defined constant intensity. This approach would also increase the conversion efficiency and/or lower the operation threshold. Thereby it might be possible to use shorter nonlinear crystals and in turn to use compact fiber lasers operating with lower average output powers, higher repetition rates and shorter pulse length than the used Yb:KGW oscillator.

The idea of enhancing the nonlinear conversion efficiency of nonlinear dielectric nanostructures by combining them with plasmonic nanostructures did not work out in the presented studies. But the situation might be different, if nonlinear dielectrics possessing higher second order nonlinear coefficients could be employed. For example zinc selenide or gallium arsenide would be interesting candidates, as they posses a 10/100 times higher second order nonlinear coefficient and are compatible with the used fabrication scheme. But within this work it was abstained from their usage, as both materials are rather hazardous. Furthermore their higher nonlinear coefficient is accompanied by a strong absorption for at least the generated second harmonic light, which could act counterproductive. Another alternative could be the use of monocrystalline nonlinear dielectrics with their crystal axis aligned with respect to the local field distributions. However this approach would be extremely demanding from the fabrication point of view. Finally one should keep in mind that it was shown in this work, that noncentrosymmetric bare plasmonic nanostructures show an orders of magnitude higher

conversion efficiency and the effort to fabricate hybrid structures is similar to the effort for fabricating multilayer metamaterials with a double-stage electron beam lithography process.

Even as it was not explicitly measured in this thesis it is reasonable to assume that two-photon resonant plasmonic nanostructures show a weaker second harmonic generation efficiency than one-photon resonant structures, due to the structure of the nonlinear susceptibility. But one-photon resonances also lead to a strong suppression of the pump light, additional to the actual depletion by conversion. There might be applications, for example in integrated optical networks, where (i) small SHG signals are sufficient and (ii) the residual pump light has to be used for additional purposes in the network. In such a scenario a strong suppression of the pump light additional to the actual conversion is undesirable, therefore two-photon resonant plasmonic nanostructures represent a promising opportunity.

An interesting property of two-photon resonant plasmonic nanostructures and metamaterials composed of those, is their ability to influence the far field properties of the generated second harmonic light, which was partially shown by controlling its polarization. In the light of these results one could also think about directional emission of the generated second harmonic light by fabricating a Yagi-Uda like nanostructure system. Such a system is composed of three antennas aligned parallel to each other, where the middle antenna is resonant for the light field to emit, the resonance of one of the other antennas is slightly red-shifted, acting as reflector, and the resonance of the last antenna is slightly blue-shifted acting as director. Such a system could be also composed of V-shaped structures, for example. Or one could think of a metamaterial which focusses the generated light to a specific position, like it is done for radio frequencies with a phased-array radar.

Last but not least the research on multiresonant plasmonic nanostructures for nonlinear frequency conversion processes is very promising, as it was shown in this thesis that their performance exceeds that of single resonant structures. If this approach can be combined with noncentrosymmetric nanostructures one cane hope for large conversion efficiencies. This could for example be done by varying the opening angel of the V-shaped structures or by combining two differently sized types of Vs in a metamaterial. This approach can then be also combined with the concept of directionality. If these attempts work out, one could finally try to reverse the process of second harmonic generation and to perform optical parametric generation, amplification and oscillation with plasmonic nanostructures and metamaterials.

Bibliography

[1] I. Newton. *Opticks: Or a Treatise of the Reflections, Refractions, Inflections & Colours of Light*. Londen, 1730.

[2] H. A. Lorentz. *Ueber die Beziehung zwischen der Fortpflanzungsgeschwindigkeit des Lichtes und der Körperdichte*. Ann. Phys. **245**, 641–665 (1880).

[3] C. F. Bohren, D. R. Huffman. *Absorption and scattering of light by small particles*. John Wiley and Sons, Inc., New York, 1983.

[4] S. A. Maier. *Plasmonics: Fundamentals and applications*. Springer, 2007.

[5] L. Novotny, B. Hecht. *Principle of Nano-Optics*. Cambridge University Press, 2012.

[6] H. Hertz. *Ueber sehr schnelle electrische Schwingungen*. Ann. Phys. **267**, 421–448 (1887).

[7] G. Marconi. *Wireless Telegraphic Communication: Nobel Lecture, 11 December 1909*. In *Nobel Lectures, Physics 1901-1921*, Elsevier Ltd., Amsterdam, 1967.

[8] P. Rai-Choudhury. *Handbook of microlithography, micromachining, and microfabrication*. 1997.

[9] P. Bharadwaj, B. Deutsch, L. Novotny. *Optical Antennas*. Adv. Opt. Photon. **1**, 438–483 (2009).

[10] P. Biagioni, J. S. Huang, B. Hecht. *Nanoantennas for visible and infrared radiation*. Rep. Prog. Phys. **75**, 024402 (2012).

[11] M. Born, E. Wolf. *Principles of Optics: Electromagnetic Theory of Propagation, Interference and Diffraction of Light*. Cambridge University Press, 1997.

[12] J. B. Pendry, A. J. Holden, W. J. Stewart, I. Youngs. *Extremely low frequency plasmons in metallic mesostructures*. Phys. Rev. Lett. **76**, 4773–4776 (1996).

[13] J. B. Pendry, A. J. Holden, D. J. Robbins, W. J. Stewart. *Magnetism from conductors and enhanced nonlinear phenomena*. IEEE T. Microw. Theory **47**, 2075–2084 (1999).

[14] S. Linden, C. Enkrich, M. Wegener, J. Zhou, T. Koschny, C. M. Soukoulis. *Magnetic response of metamaterials at 100 terahertz*. Science **306**, 1351–1353 (2004).

[15] S. Zhang, W. Fan, B. K. Minhas, A. Frauenglass, K. J. Malloy, S. R. J. Brueck. *Midinfrared resonant magnetic nanostructures exhibiting a negative permeability.* Phys. Rev. Lett. **94** (2005).

[16] C. Enkrich, M. Wegener, S. Linden, S. Burger, L. Zschiedrich, F. Schmidt, J. F. Zhou, T. Koschny, C. M. Soukoulis. *Magnetic metamaterials at telecommunication and visible frequencies.* Phys. Rev. Lett. **95** (2005).

[17] R. A. Shelby, D. R. Smith, S. Schultz. *Experimental verification of a negative index of refraction.* Science **292**, 77–79 (2001).

[18] V. M. Shalaev. *Optical negative-index metamaterials* (2007).

[19] C. M. Soukoulis, S. Linden, M. Wegener. *Negative refractive index at optical wavelengths.* Science **315**, 47–9 (2007).

[20] D. Schurig, J. J. Mock, B. J. Justice, S. A. Cummer, J. B. Pendry, A. F. Starr, D. R. Smith. *Metamaterial electromagnetic cloak at microwave frequencies.* Science **314**, 977–980 (2006).

[21] W. Cai, U. K. Chettiar, A. V. Kildishev, V. M. Shalaev. *Optical cloaking with metamaterials.* Nat. Photonics **1**, 224 – 227 (2007).

[22] T. Ergin, N. Stenger, P. Brenner, J. B. Pendry, M. Wegener. *Three-Dimensional Invisibility Cloak at Optical Wavelengths.* Science **328**, 337–339 (2010).

[23] P. A. Franken, A. E. Hill, C. W. Peters, G. Weinreich. *Generation of optical harmonics.* Phys. Rev. Lett. **7**, 118 (1961).

[24] T. H. Maiman. *Stimulated optical radiation in ruby.* Nature **187**, 493 (1960).

[25] D. Lindley. *Focus: Landmarks - Ruby Red Laser Light Becomes Ultraviolet.* Physics **7** (2014).

[26] J. A. Armstrong, N. Bloembergen, J. Ducuing, P. S. Pershan. *Interactions between light waves in a nonlinear dielectric.* Phys. Rev. **127**, 1918–1939 (1962).

[27] R. C. Miller. *Optical 2nd harmonic generation in piezoelectric crystals.* Appl. Phys. Lett. **5**, 17 (1964).

[28] C. G. B. Garrett, F. N. H. Robinson. *Miller's phenomenological rule for computing nonlinear susceptibilities.* IEEE J. Quant. Electron. **QE-2**, 328–329 (1966).

[29] R. W. Boyd. *Nonlinear Optics.* Academic Press, San Diego, 2003.

[30] B. Lambrecht, A. Leitner, F. R. Aussenegg. *Femtosecond decay-time measurement of electron-plasma oscillation in nanolithographically designed silver particles.* Appl. Phys. B-Lasers O. **64**, 269–272 (1997).

[31] M. W. Klein, C. Enkrich, M. Wegener, S. Linden. *Second-harmonic generation from magnetic metamaterials.* Science **313**, 502–504 (2006).

[32] M. W. Klein, M. Wegener, N. Feth, S. Linden. *Experiments on second- and third-harmonic generation from magnetic metamaterials.* Opt. express **15**, 5238 (2007).

[33] Y. Zeng, W. Hoyer, J. Liu, S. W. Koch, J. V. Moloney. *Classical theory for second-harmonic generation from metallic nanoparticles.* Phys. Rev. B **79**, 235109 (2009).

[34] F. B. Niesler, N. Feth, S. Linden, J. Niegemann, J. Gieseler, K. Busch, M. Wegener. *Second-harmonic generation from split-ring resonators on a GaAs substrate.* Opt. Lett. **34**, 1997–1999 (2009).

[35] Y. Pu, R. Grange, C. L. Hsieh, D. Psaltis. *Nonlinear optical properties of core-shell nanocavities for enhanced second-harmonic generation.* Phys. Rev. Lett. **104**, 207402 (2010).

[36] S. Linden, F. B. P. Niesler, J. Förstner, Y. Grynko, T. Meier, M. Wegener. *Collective effects in second-harmonic generation from split-ring-resonator arrays.* Phys. Rev. Lett. **109**, 015502 (2012).

[37] R. Czaplicki, H. Husu, R. Siikanen, J. Mäkitalo, M. Kauranen, J. Laukkanen, J. Lehtolahti, M. Kuittinen. *Enhancement of second-harmonic generation from metal nanoparticles by passive elements.* Phys. Rev. Lett. **110**, 093902 (2013).

[38] H. Aouani, M. Rahmani, M. Navarro-Cía, S. A. Maier. *Third-harmonic-upconversion enhancement from a single semiconductor nanoparticle coupled to a plasmonic antenna.* Nat. nanotechnol. **9**, 290–4 (2014).

[39] B. Metzger, M. Hentschel, T. Schumacher, M. Lippitz, X. Ye, C. B. Murray, B. Knabe, K. Buse, H. Giessen. *Doubling the Efficiency of Third Harmonic Generation by Positioning ITO Nanocrystals into the Hot-Spot of Plasmonic Gap-Antennas.* Nano Lett. **14**, 2867–2872 (2014).

[40] F. B. P. Niesler, N. Feth, S. Linden, M. Wegener. *Second-harmonic optical spectroscopy on split-ring-resonator arrays.* Opt. Lett. **36**, 1533–1535 (2011).

[41] K. Thyagarajan, S. Rivier, A. Lovera, O. J. F. Martin. *Enhanced second-harmonic generation from double resonant plasmonic antennae.* Opt. express **20**, 12860 (2012).

[42] M. Kauranen, A. V. Zayats. *Nonlinear plasmonics.* Nat. Photonics **6**, 737–748 (2012).

[43] D. A. Skoog, F. J. Holler, S. R. Crouch. *Principles of instrumental analysis.* Brooks/Cole : Thomson Learning, Australia, 2007.

[44] J. C. D. Brand. *Lines of Light.* CRC Press, 1995.

[45] J. D. Jackson. *Classical Electrodynamics.* John Wiley and Sons, Inc., New York, 1941.

[46] D. Meschede. *Optik, Licht und Laser.* Teubner, Wiesbaden, 2005.

[47] F. A. Hopf, G. I. Stegemann. *Applied Classical Electrodynamics, Volume I: Linear Optics.* John Wiley and Sons, Inc., New York, 1985.

[48] P. Drude. *Zur Elektronentheorie der Metalle.* Ann. Phys. **306**, 566–613 (1900).

[49] P. B. Johnson, R. W. Christy. *Optical constants of the noble metals.* Phys. Rev. B **6**, 4370–4379 (1972).

[50] N. E. Christensen, B. O. Seraphin. *Relativistic Band Calculation and the Optical Properties of Gold.* Phys. Rev. B **4**, 3321 (1971).

[51] J. S. Hesthaven, T. Warburton. *Nodal Discontinuous Galerkin Methods - Algorithms, Analysis, and Applications.* Springer-Verlag, Berlin, 2007.

[52] K. Busch, M. König, J. Niegemann. *Discontinuous Galerkin methods in nanophotonics.* Laser Photonics Rev. **5**, 773–809 (2011).

[53] L. Novotny, C. Hafner. *Light propagation in a cylindrical waveguide with a complex, metallic, dielectric function.* Phys. Rev. E **50**, 4094–4106 (1994).

[54] E. Feigenbaum, M. Orenstein. *Ultrasmall volume plasmons, yet with complete retardation effects.* Phys. Rev. Lett. **101** (2008).

[55] J. Dorfmüller, R. Vogelgesang, R. T. Weitz, C. Rockstuhl, C. Etrich, T. Pertsch, F. Lederer, K. Kern. *Fabry-Pérot resonances in one-dimensional plasmonic nanostructures.* Nano Lett. **9**, 2372–2377 (2009).

[56] J. S. Huang, J. Kern, P. Geisler, P. Weinmann, M. Kamp, A. Forchel, P. Biagioni, B. Hecht. *Mode imaging and selection in strongly coupled nanoantennas.* Nano Lett. **10**, 2105–2110 (2010).

[57] W. Rechberger, A. Hohenau, A. Leitner, J. R. Krenn, B. Lamprecht, F. R. Aussenegg. *Optical properties of two interacting gold nanoparticles.* Opt. Commun. **220**, 137–141 (2003).

[58] H. Goldstein. *Classical mechanics.* Addison-Wesley Publishing Company Inc., London, 1985.

[59] B. Metzger. *Ultrafast Nonlinear Plasmonics.* Universität Stuttgart, 2014.

[60] I. N. Bronstein, K. A. Semendjajew, G. Musiol, H. Mühlig. *Taschenbuch der Mathematik.* 2008.

[61] F. von Cube, S. Irsen, R. Diehl, J. Niegemann, K. Busch, S. Linden. *From isolated metaatoms to photonic metamaterials: Evolution of the plasmonic near-field.* Nano Lett. **13**, 703–708 (2013).

[62] I. Sersic, M. Frimmer, E. Verhagen, A. F. Koenderink. *Electric and Magnetic Dipole Coupling in Near-Infrared Split-Ring Metamaterial Arrays.* Phys. Rev. Lett. **103** (2009).

[63] M. Decker, N. Feth, C. M. Soukoulis, S. Linden, M. Wegener. *Retarded long-range interaction in split-ring-resonator square arrays.* Phys. Rev. B **84** (2011).

[64] A. Beer. *Bestimmung der Absorption des rothen Lichts in farbigen Flüssigkeiten.* Ann. Phys. **162**, 78–88 (1852).

[65] S. E. Harris, M. K. Oshman, R. L. Byer. *Observation of tunable optical parametric fluorescence.* Phys. Rev. Lett. **18**, 732–734 (1967).

[66] F. A. Hopf, G. I. Stegemann. *Applied Classical Electrodynamics, Volume II: Nonlinear Optics.* John Wiley and Sons, Inc., New York, 1986.

[67] P. Y. Chen, C. Argyropoulos, A. Alù. *Enhanced nonlinearities using plasmonic nanoantennas.* Nanophotonics **1**, 221–233 (2012).

[68] U. K. Chettiar, N. Engheta. *Optical frequency mixing through nanoantenna enhanced difference frequency generation: Metatronic mixer.* Phys. Rev. B **86** (2012).

[69] S. B. Hasan, F. Lederer, C. Rockstuhl. *Nonlinear plasmonic antennas.* Materials Today **17**, 478–485 (2014).

[70] J. I. Dadap, J. Shan, K. B. Eisenthal, T. F. Heinz. *Second-Harmonic Rayleigh Scattering from a Sphere of Centrosymmetric Material* (1999).

[71] M. Finazzi, P. Biagioni, M. Celebrano, L. Duò. *Selection rules for second-harmonic generation in nanoparticles.* Phys. Rev. B **76** (2007).

[72] R. Dendy. *Plasma Physics: An Introductory Course.* Cambridge University Press, 1993.

[73] J. E. Midwinter, J. Warner. *The effects of phase matching method and of uniaxial crystal symmetry on the polar distribution of second-order non-linear optical polarization.* Brit. J. Appl. Phys. **16**, 1135–1142 (2002).

[74] R. Chang, J. Ducuing, N. Bloembergen. *Dispersion of the Optical Nonlinearity in Semiconductors.* Phys. Rev. Lett. **15**, 415–418 (1965).

[75] C. Chen, A. de Castro, Y. Shen. *Surface-Enhanced Second-Harmonic Generation.* Phys. Rev. Lett. **46**, 145–148 (1981).

[76] D. S. Hum, M. M. Fejer. *Quasi-phasematching.* C. R. Phys. **8**, 180–198 (2007).

[77] M. Baudrier-Raybaut, R. Haidar, P. Kupecek, P. Lemasson, E. Rosencher. *Random quasi-phase-matching in bulk polycrystalline isotropic nonlinear materials.* Nature **432**, 374–376 (2004).

[78] S. E. Skipetrov. *Disorder is the new order.* Nature **432** (2004).

[79] S. Helmfrid, G. Arvidsson. *Influence of randomly varying domain lengths and nonuniform effective index on second-harmonic generation in quasi-phase-matching waveguides.* J. Opt. Soc. Am. B **8**, 797 (1991).

[80] M. M. Fejer, G. A. Magel, D. H. Jundt, R. L. Byer. *Quasi-phase-matched second harmonic generation: tuning and tolerances.* IEEE J. Quant. Electron. **28** (1992).

[81] V. Mizrahi, J. E. Sipe. *Phenomenological treatment of surface second-harmonic generation.* J. Opt. Soc. Am. B **5**, 660 (1988).

[82] G. Cerullo, S. De Silvestri. *Ultrafast optical parametric amplifiers.* Rev. Sci. Instrum. **74**, 1–18 (2003).

[83] C. Manzoni, G. Cirmi, D. Brida, S. de Silvestri, G. Cerullo. *Optical-parametric-generation process driven by femtosecond pulses: Timing and carrier-envelope phase properties.* Phys. Rev. A **79**, 033818 (2009).

[84] R. L. Byer, S. E. Harris. *Power and bandwidth of spontaneous parametric emission.* Phys. Rev. **168**, 1064–1068 (1968).

[85] M. H. Dunn, M. Ebrahimzadeh. *Parametric generation of tunable light from continous-wave to femtosecond pulses.* Science **286**, 1513–1517 (1999).

[86] V. Petrov. *Parametric down-conversion devices: The coverage of the mid-infrared spectral range by solid-state laser sources.* Opt. Mater. **34**, 536–554 (2012).

[87] R. Sowade, J. Kieß ling, I. Breunig. *CW laser light tunable from blue to red: OPOs pave the way.* Photonik int. 63–65 (2013).

[88] T. Südmeyer, J. Aus der Au, R. Paschotta, U. Keller, P. G. R. Smith, G. W. Ross, D. C. Hanna. *Novel ultrafast parametric systems: high repetition rate single-pass OPG and fibre-feedback OPO.* J. Phys. D Appl. Phys. **34**, 2433–2439 (2001).

[89] S. V. Marchese, E. Innerhofer, R. Paschotta, S. Kurimura, K. Kitamura, G. Arisholm, U. Keller. *Room temperature femtosecond optical parametric generation in MgO-doped stoichiometric LiTaO3.* Appl. Phys. B **81**, 1049–1052 (2005).

[90] G. Arisholm. *General analysis of group velocity effects in collinear optical parametric amplifiers and generators.* Opt. Express **15**, 4941–4947 (2007).

[91] R. L. Byer. *Nonlinear Optical Phenomena and Materials.* Annual Review of Materials Science **4**, 147–190 (1974).

[92] S. M. Eaton, H. Zhang, P. R. Herman, F. Yoshino, L. Shah, J. Bovatsek, A. Y. Arai. *Heat accumulation effects in femtosecond laser- written waveguides with variable repetition rate.* Opt. express **13**, 2496–2504 (2005).

[93] J. C. Diels, W. Rudolph. *Ultrashort Laser Pulse Phenomena.* Academic Press, 2006.

[94] A. Smith. *SNLO, http://www.as-photonics.com.*

[95] H. Linnenbank, S. Linden. *High repetition rate femtosecond double pass optical parametric generator with more than 2 W tunable output in the NIR.* Opt. express **22**, 18072 (2014).

[96] T. A. Rabson. *Stimulated parametric fluorescence induced by picosecond pump pulses.* Appl. Phys. Lett. **21**, 129 (1972).

[97] P. Zhao, B. Zhang, E. Li, R. Zhou, D. Xu, Y. Lu, T. Zhang, F. Ji, X. Zhu, P. Wang, J. Yao. *Experimental study on a high conversion efficiency, low threshold, high-repetition-rate periodically poled lithium niobate optical parametric generator.* Opt. express **14**, 7224 (2006).

[98] M. Levenius, V. Pasiskevicius, F. Laurell, K. Gallo. *Ultra-broadband optical parametric generation in periodically poled stoichiometric LiTaO3.* Opt. express **19**, 4121–8 (2011).

[99] S. Chaitanya Kumar, M. Jelínek, M. Baudisch, K. T. Zawilski, P. G. Schunemann, V. Kubeček, J. Biegert, M. Ebrahim-Zadeh. *Tunable, high-energy, mid-infrared, picosecond optical parametric generator based on CdSiP2.* Opt. express **20**, 15703–9 (2012).

[100] F. Seifert, V. Petrov, F. Noack. *Sub-100-fs optical parametric generator pumped by a high-repetition-rate Ti:sapphire regenerative amplifier system.* Opt. Lett. **19**, 837–839 (1994).

[101] X. Xie, A. M. Schober, C. Langrock, R. V. Roussev, J. R. Kurz, M. M. Fejer. *Picojoule threshold, picosecond optical parametric generation in reverse proton-exchanged lithium niobate waveguides.* J. Opt. Soc. Am. B **21**, 1397 (2004).

[102] M. Marangoni, R. Osellame, R. Ramponi, G. Cerullo, A. Steinmann, U. Morgner. *Near-infrared optical parametric amplifier at 1 MHz directly pumped by a femtosecond oscillator.* Opt. Lett. **32**, 1489 (2007).

[103] F. Brunner, T. Südmeyer, E. Innerhofer, F. Morier-Genoud, R. Paschotta, V. E. Kisel, V. G. Shcherbitsky, N. V. Kuleshov, J. Gao, K. Contag, A. Giesen, U. Keller. *240-fs pulses with 22-W average power from a mode-locked thin-disk Yb:KY(WO(4))(2) laser.* Opt. Lett. **27**, 1162–1164 (2002).

[104] A. Steinmann, B. Metzger, R. Hegenbarth, H. Giessen. *Compact 7.4 W femtosecond oscillator for white-light generation and nonlinear microscopy.* CLEO: 2011 - Laser Science to Photonic Applications 1–2 (2011).

[105] F. Hoos, T. P. Meyrath, S. Li, B. Braun, H. Giessen. *Femtosecond 5-W Yb:KGW slab laser oscillator pumped by a single broad-area diode and its application as supercontinuum source.* Appl. Phys. B-Lasers O. **96**, 5–10 (2009).

[106] G. P. Banfi, C. Solcia, P. D. Trapani, R. Danielius, A. Piskarskas, R. Righini, R. Torre. *Travelling-wave parametric conversion of microjoule pulses with {LBO}.* Opt. Commun. **118**, 353–359 (1995).

[107] M. Koichi, K. Miyamoto, S. Ujita, T. Saito, H. Ito, T. Omatsu. *Dual-frequency picosecond optical parametric generator pumped by a Nd-doped vanadate bounce laser.* Opt. express **19**, 18523–8 (2011).

[108] G. D. Boyd, D. A. Kleinman. *Parametric interaction of focused Gaussian light beams.* J. Appl. Phys. **39**, 3597–3639 (1968).

[109] J. M. Manley, H. E. Rowe. *Some general properties of nonlinear elements 1: general energy relations.* Proc. Institute Radio Engineers **44**, 904–913 (1956).

[110] O. Gayer, Z. Sacks, E. Galun, A. Arie. *Temperature and wavelength dependent refractive index equations for MgO-doped congruent and stoichiometric LiNbO_3.* Appl. Phys. B: Lasers Opt. **91**, 343–348 (2008).

[111] L. Holland. *Vacuum deposition of thin films.* Chapman and Hall Ltd., London, 1963.

[112] E. R. Olson, R. D. Mathis. *Silicon monoxide evaporation with the multi-baffled box source* (1963).

[113] K. Cheng, M. Le, D. Mitchell, L. Hanes *Effects of Electron Radiation Generated during E-beam Evaporation on a Photoresist Liftoff Process.* In *GaAs Mantech Ceonference*, 2010.

[114] J. E. Lennard-Jones. *The migration and aggregation of atoms on solid surfaces.* P. Phys. Soc. **49**, 140 (1937).

[115] M. N. Borah, P. C. Sarmah, A. Rahman. *Effect of substrate temperature on structural properties of thermally evaporated ZnSe thin films.* J. Optoelectron. Adv. M. **10**, 427–433 (2008).

[116] P. Buffat, J. P. Borel. *Size effect on the melting temperature of gold particles.* Phys. Rev. A **13**, 2287–2298 (1976).

[117] N. Bouhssira, S. Abed, E. Tomasella, J. Cellier, A. Mosbah, M. S. Aida, M. Jacquet. *Influence of annealing temperature on the properties of ZnO thin films deposited by thermal evaporation.* Appl. Surf. Sci. **252**, 5594–5597 (2006).

[118] F. Khan, A. Mobin, M. Husain, G. Energy, S. Korea, J. M. Islamia. *Formation of ZnO by Annealing of Thermally Evaporated Zinc in Oxygen Ambient for Solar Cell Application.* Int. J. Electron. **2**, 823–827 (2013).

[119] P. M. Jais, C. Von Bilderling, A. V. Bragas. *Plasmon-enhanced second harmonic generation in semiconductor quantum dots close to metal nanoparticles.* Papers in Physics **3**, 1–5 (2011).

[120] G. Grinblat, M. Rahmani, E. Cortés, M. Caldarola, D. Comedi, S. A. Maier, A. V. Bragas. *High-Efficiency Second Harmonic Generation from a Single Hybrid ZnO Nanowire/Au Plasmonic Nano-Oligomer.* Nano Lett. **14**, 6660–6665 (2014).

[121] H. Linnenbank, Y. Grynko, J. Förstner, S. Linden. *Second harmonic generation spectroscopy on hybrid plasmonic/dielectric nanoantennas.* Light: Science and Applications **submitted** (2015).

[122] R. Jin, J. E. Jureller, H. Y. Kim, N. F. Scherer. *Correlating Second Harmonic Optical Responses of Single Ag Nanoparticles with Morphology.* J. Am. Chem. Soc. **127**, 12482–12483 (2005).

[123] J. Butet, J. Duboisset, G. Bachelier, I. Russier-Antoine, E. Benichou, C. Jonin, P. F. Brevet. *Optical Second Harmonic Generation of Single Metallic Nanoparticles Embedded in a Homogeneous Medium.* Nano Lett. **10**, 1717–1721 (2010).

[124] N. Accanto, L. Piatkowski, J. Renger, N. F. van Hulst. *Capturing the Optical Phase Response of Nanoantennas by Coherent Second-Harmonic Microscopy.* Nano Lett. **14**, 4078–4082 (2014).

[125] K. Stannigel, M. König, J. Niegemann, K. Busch. *Discontinuous Galerkin time-domain computations of metallic nanostructures.* Opt. express **17**, 14934–14947 (2009).

[126] A. I. Akhiezer. *Plasma electrodynamics - Vol.2: Nonlinear theory and fluctuations.* Pergamon Press, 1975.

[127] H. Harutyunyan, G. Volpe, R. Quidant, L. Novotny. *Enhancing the nonlinear optical response using multifrequency gold-nanowire antennas.* Phys. Rev. Lett. **108** (2012).

[128] A. Ashkin, G. D. Boyd, J. M. Dziedzic. *Resonant Optical Second Harmonic Generation And Mixing.* IEEE J. Quantum. Electron. **QE 2**, 109–124 (1966).

[129] C. Zimmermann, R. Kallenbach, T. W. Hänsch, J. Sandberg. *Doubly-resonant second-harmonic generation in beta-barium-borate.* Opt. Commun. **71**, 229–234 (1989).

[130] A. Wokaun, J. G. Bergman, J. P. Heritage, A. M. Glass, P. F. Liao, D. H. Olson. *Surface second-harmonic generation from metal island films and microlithographic structures.* Phys. Rev. B **24**, 849–856 (1981).

[131] H. P. Wagner, M. Kühnelt, W. Langbein, J. M. Hvam. *Dispersion of the second-order nonlinear susceptibility in ZnTe, ZnSe, and ZnS.* Phys. Rev. B **58**, 494–501 (1998).

[132] H. Linnenbank, S. Linden. *Second harmonic generation with two-photon resonant plasmonic metamaterials.* Optica **submitted** (2015).

[133] F. Ghebremichael, C. Poga, M. G. Kuzyk. *Optical second harmonic characterization of spontaneous symmetry-breaking at polymer/transparent conductor interfaces.* Appl. Phys. Lett. **66** (1995).

[134] W. Wang, J. Xu, X. Liu, Y. Jiang, G. Wang, X. Lu. *Second harmonic generation investigation of indium tin oxide thin films.* Thin Solid Films **365**, 116–118 (2000).

[135] G. Ghosh. *Dispersion-equation coefficients for the refractive index and birefringence of calcite and quartz crystals.* Opt. Com. **163**, 95–102 (1999).

[136] H. Aouani, M. Navarro-Cia, M. Rahmani, T. P. H. Sidiropoulos, M. Hong, R. F. Oulton, S. A. Maier. *Multiresonant Broadband Optical Antennas As Efficient Tunable Nanosources of Second Harmonic Light.* Nano Lett. **12**, 4997–5002 (2012).

List of publications

Parts of this thesis have already been published in refereed scientific journals:

- H. Linnenbank, S. Linden. *High repetition rate femtosecond double pass optical parametric generator with more than 2 W tunable output in the NIR.* Opt. express **22**, 18072 (2014).

Parts of this thesis have already been submitted to refereed scientific journals:

- H. Linnenbank, Y. Grynko, J. Förstner, S. Linden. *Second harmonic generation spectroscopy on hybrid plasmonic/dieletric nanoantennas.* Light: Sience and Applications **submitted**, (2015).
- H. Linnenbank, S. Linden. *Second harmonic generation with two-photon resonant plasmonic metamaterials.* Optica **submitted**, (2015).

Additional work on other topics has been published in refereed scientific journals

- T. Beckmann, H. Linnenbank, H. Steigerwald, B. Sturman, D. Haertle, K. Buse, I. Breunig. *Highly tunable low-threshold optical parametric oscillation in radially poled whispering gallery resonators.* Phys. Rev. Lett. **106**, 143903 (2011)

Acknowledgments

During the time of conducting my thesis a lot of people helped in many different ways. Here, I would like to take the opportunity of saying thank you to some of them:

First of all I would like to thank Prof. Dr. Stefan Linden for giving me the opportunity to write my PhD thesis in his research group and providing a remarkable environment for this task. He was an excellent teacher and supervisor, whose responsibility for the success of my work should not be underestimated. He was always open for discussions also about my strangest ideas and put an enormous trust in my abilities, regardless of the field of activity.

I want to thank PD Dr. Elisabeth Soergel for her kind readiness to take over the primary review of my thesis, but also for her regular friendly advices since the beginning of my diploma thesis. Thanks also to PD Dr. Bernard Metsch and Prof. Dr. Werner Mader for the secondary reviews.

Special thanks go to: Dr. Jens Niegemann and Dr. Yevgen Grynko, who not only supported me with numerical calculations, but also tried to give me an understanding of numerical physics. Dr. Johannes Overbuschmann and Angelika Rüttgers for their advisory in electron microscopy. Dr. Stephan Irsen and Carola Tröger for saving me from serious damage during my self-studies in the chemistry lab. Peter Holik and Bert Kann for introducing me into vacuum techniques and supporting me in the sample fabrication.

I am indebted to all proof readers of this thesis for their supporting comments and hints which improved the readability.

Thanks to the Nanophotonic group at the Rheinische Friedrich-Wilhelms-Universität Bonn and the EMA/konTEM group at the research center caesar, the current and the former members, for their support and the numerous discussions. Despite the science related stuff I will always look back at our coffee breaks, whiskey and video evenings, the barbecues and the evenings at conferences, which embellished the working ambience during my hole thesis.

Last, but not least, I would like to thank my parents for their support throughout my life, but especially for letting me go my own way with a little prodding in the right direction. I thank my entire club the Hard 'n Heavy's Rhein-Sieg for all the occasions to clear my mind and I beg pardon for my decision to choose an academic career. I want to thank my wife Jessica from the bottom of my heart for her understanding, support, encouragement and love during the past years, but also for bringing me back to earth if necessary. As I wrote at the end of my diploma thesis, without her I would have never made it this far.

To quote I. Newton for the last time: *"If I have seen further it is by standing on the shoulders of Giants."*